A STUDY ON MEASUREMENT OF NORMALIZED RADAR CROSS SECTION OF EARTH SURFACES BY SPACEBORNE SYNTHETIC APERTURE RADAR

衛星搭載用合成開口レーダを用いた
地表の規格化後方散乱断面積の計測に関する研究

Masanobu Shimada
島田政信

A STUDY ON MEASUREMENT OF NORMALIZED RADAR CROSS SECTION OF EARTH SURFACES BY SPACEBORNE

A Study on Measurement of Normalized Radar Cross Section of Earth Surfaces by Spaceborne Synthetic Aperture Radar

衛星搭載用合成開口レーダを用いた
地表の規格化後方散乱断面積の計測に関する研究

Masanobu Shimada
島田政信

June 1998

Thesis submitted to the University of Tokyo
in partial fulfillment of the requirements for the degree of
Doctor of Engineering

SUMMARY

This thesis presents the result of investigations on the calibration methods to estimate the normalized radar cross section, σ^0, of earth surfaces from the space-borne synthetic aperture radar (SAR) data. The calibration of the SAR system which is composed of the SAR instrument, the SAR processor, and calibrators, has become very important in recent years because the studies on the physical relation between σ^0 and the target characteristics have highly advanced and the absolute value of σ^0 derived from SAR data is being used in the global environment monitoring studies. The rain forest deforestation, oil spill disaster in the ocean, land use change, sea ice movement classification, etc., are the typical targets observations by SAR. In the measurement of σ^0 there are such error sources as receiver thermal noise, saturation noise at A/D converter, temporal change of antenna pattern, instability of the calibration instrument deployed on the ground, and the terrain gradient. For deriving accurate σ^0, these error sources must be carefully analyzed and be finally deleted. The following is the summary of the investigations presented in this thesis.

A new radar equation for SAR, in which saturation at A/D converter is considered, has been derived. A new calibration method on SAR images with saturation has been proposed. The method has been applied to real SAR images effectively.

A new method to estimate the antenna elevation pattern of an inflight SAR has been proposed. A screening processing using the χ^2 test to collect similarly distributed areas and inclusion of the signal-to-noise ratio in the radar equation are the feature of this method. By applying the method, the antenna elevation pattern of the SIR-B (Shuttle Imaging Radar-B) has been determined with an accuracy of 0.1 dB.

An accurate impulse response function has been developed for the frequency-tunable active radar calibrators (ARC). From computer simulations and field experiments on the JERS-1 (Japanese Earth Resources Satellite-1) SAR, the following has been shown and/or derived: 1) the location shift and the peak gain loss can be estimated with an accuracy less than 4.2 m and 1.6 dB accuracy, respectively, 2) the peak calibration method is not effective for the frequency-tunable ARC because of resolution broadening and decrease of peak, 3) the integral method should be used for the frequency-tunable ARC, and 4) the allowable frequency shift has an upper limit, which is about 40 Hz in the case of the L-band SAR.

As an example of calibration applications, images of two paths of the JERS-1 SAR over the Amazon have been connected based on the proposed calibration methods. The images have successfully been connected without generating visible banding. The accuracies of the peak method and the integral method have been compared.

The SAR interferometry technique has been applied to correct the effect of slope in σ^0 determination. It has been shown that σ^0 can be obtained with an accuracy of about 0.3 dB when the interferometric condition is satisfied. It has also been shown that the accuracy will become less than 0.1 dB when the perpendicular baseline distance is determined with an accuracy of 2% or higher.

CONTENTS

List of Tables

CHAPTER 1 INTRODUCTION

1.1 Background

1.1.1 Need for Earth monitoring by SAR

Global environmental changes from the 1980s, e.g., warming, ozone depletion, disasters (floods and hurricanes), and earthquakes, require the total understanding of the Earth system. The Earth is a very complex thermodynamic ecosystem, balancing the solar energy, the Earth radiation, and the inhabitants' energy consumption. If the energy interactions between the elements (i.e., forests, desert, water, land, ice, and snow) are expressed accurately, we may obtain some keys for describing the mechanism of these unusual phenomena and may have some ideas to prevent or delay them. These phenomena occur nearly randomly on different spatial and time scales (several kilometers to several thousand kilometers, and several seconds to several years). Earth orbiting satellites carrying the appropriate sensors may detect these phenomena because of their large spatial coverage and frequent availability. Active microwave instruments using relatively low-frequency signals (i.e., several hundred MHz to several GHz) are vital for Earth observation because those signals are self-generated, do not rely on the sun light, and can directly carry the Earth surface information unaffected by the atmosphere.

Synthetic Aperture Radar (SAR) is an active microwave instrument that performs high-resolution observation under almost all weather conditions. The measurements are the backscattered signals from the targets on the Earth in response to its transmission code. The optimal correlation of these signals with the ideal SAR receiving signal achieves high-resolution imaging of several meters. These correlated signals (or simply SAR images) contain information on the targets, the wave-propagation media, the distance between the SAR and the target, and the SAR characteristics. If the image is well modeled for these targets, the SAR observation can retrieve the target itself. There are, however, two difficulties: first is how well the SAR characteristics are eliminated from the SAR images and how accurately the signal power or the backscattering coefficient of the target is determined; second is how accurately the backscattering model can be built for each target. The first difficulty is so-called SAR calibration. Because erroneous calibration of SAR images causes mis-understanding of the targets, the SAR calibration is very important.

1.1.2 SAR instrument and processing algorithms

High-resolution imaging by the two-dimensional correlation of the scattered signal can be performed optically or digitally. The SAR imaging principle was first developed by Wiley [9] in the 1950s, and was verified by using the experimental SAR instruments and optical image processor by the end of the 1950s [10]. Digital SAR processing and its application evolved after an effective computing approach was proposed by Wu in 1978 [11]. Wu's approach enabled reducing the heavy mathematical load by employing the Fast Fourier Transform (FFT) for the range and azimuth correlation processing (this method is called the Range-Doppler method). SAR imaging algorithms were developed in many ways, i.e., range Doppler, seismic method [12], and chirp scaling [13]. All these algorithms have reduced possible distortion and yielded higher throughput.

The first spaceborne SAR on SEASAT was developed by NASA JPL (Jet Propulsion Laboratory) [1] and launched to an 800 km polar orbit in 1978 with the other microwave instruments as a "proof of concept" mission. This SAR featured a high resolution of 30m (in azimuth, four looks) and 10m (in slant range), L-band and HH polarization, a fixed off-nadir angle of 23 degrees, an imaging width of 100 Km, passive array antenna of 12 m x 2 m, a transmission power of 1000 W, an onboard data formatter which enabled the digital data generation on-ground, and the repeat-pass interferometry which was arranged after the launch. Although the SEASAT mission was terminated three months after the launch due to a power unit failure, most of the SAR missions succeeded. The huge amount of data acquired through its life advanced the SAR technologies not only for sensor development but also for digital signal processing, data interpretation, and Earth sciences. Following SEASAT, the Shuttle Imaging Radars (SIR-A in 1982 and SIR-B in 1984 [46]) promoted the radar science. The SARs onboard ERS-1/2 (European Remote sensing Satellite-1/2) (1990, 1995) [2], JERS-1 (Japanese Earth Resources Satellite-1) (1992) [3], [16], and Radarsat (1995) [4], [15] are being used more operationally at different frequencies, polarizations, and incidence angles. To increase the measurement consistency (same time, same place) at different radar parameters, SIR-C/X-SAR (1994) [5], [47] was launched on a later space shuttle mission. The data acquired in the two 10-day mission covers 19% of the land, 100 million km^2, within +- 60 degrees of the latitude in L, C, X bands with full polarizations and wide incidence angles. ALMAZ, the Russian SAR system, operated at S-band. Moon surface observation by Apollo 17 and Venus observation by the Magellan SAR [6], [17] are planetary applications of SAR technology [14].

1.1.3 Normalized radar cross section and its properties

As a general measure of backscattering properties, the bi-directional normalized radar cross section σ^0 is defined by ([7], [8], Fig. 1-1)

$$\sigma^0(\theta_s,\varphi_s:\theta,\varphi)=\frac{4\pi R^2\left\langle\left|E_r^s\right|^2\right\rangle}{A\cdot\left\langle\left|E_t^i\right|^2\right\rangle}, \qquad (1.1)$$

where (θ, φ) is the direction of the incident wave; (θ_s, φ_s) is the direction of the scattered wave; E_t^i and E_r^s are the electric filed of incident and scattered wave with t or r polarization; t and r are the horizontal or vertical polarizations; A is the illumination area; and $\langle\ \rangle$ is the expectation. This quantity is the energy ratio of the total power scattered by an equivalent isotropic scatterer in direction (θ_s, φ_s) to the products of incident power density in direction of (θ, φ) and the illuminated area A. Usually, σ^0 is measured for the case in which the incident and scattering directions are the same. σ^0 for the backscattering case (incident angle = scattered angle) is sometimes called "the backscattering coefficient." If the incident and scattered signal fields are very stable, σ^0 can be accurately measured. Speckle, a fading of scatterers within a SAR resolution cell, however, provides a considerably large fluctuation on σ^0 measurement. In addition, the SAR adds the thermal noise and A/D conversion noise to the measurements. Moreover, multiple scattering between the target and the radar propagation media fluctuates incident and scattered signals. Thus, σ^0 is the statistical value [59].

Scattering in the microwave region depends on the surface roughness, three-dimensional distribution of the complex emissivity, and the local incidence angle of the incoming signal to a target. More generally, σ^0 of a target is expressed by

$$\sigma^0(x,y,t,\theta,\varphi,\lambda), \qquad (1.2)$$

where x (y) is the location, t is the time, and λ is the wavelength. Ideally, any target can be represented by these parameters. σ^0 also depends on the structure and composition of the targets. The microwave signals most commonly used in SAR imaging are in the P (70 cm), L (23.5 cm), S (10 cm), C (5.6 cm), and X (3 cm) bands, where the numbers in parenthesis are the representative wavelengths. The lower the frequency, the more the signal penetrates the target and is scattered by the target structure. The higher the frequency, the more scattering occurs at the target surface. The overall scattering intensity, therefore, depends on the combination of the direct scattering at the target surface, the penetration rate which depends on the wavelength, and the size of the scatterers within the target. Because the target may contain a huge number of small scatterers, the received signal has statistical properties.

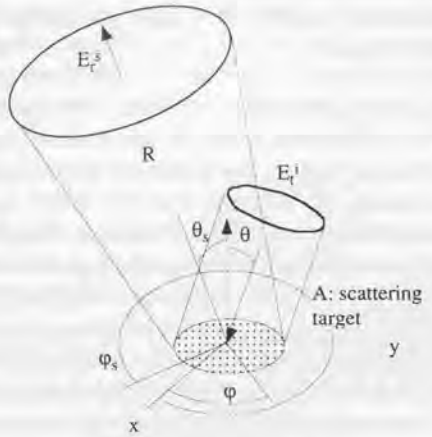

Fig. 1-1 Coordinate system for bistatic radar scattering

1.1.4 SAR data interpretation and the accuracy requirements

We here observe SAR data examples and consider the accuracy requirements for SAR calibration.

Forest

Some 30% of the global surface is the forest, and its biomass plays an important role in Earth environment maintenance. Identifying the forest region and estimating the forest biomass are desirable for understanding global phenomena. A typical flat rainforest image of the Amazon in Brazil acquired by JERS-1 SAR is shown in Fig. 1-2. This region suffers from expanding deforestation. The dark broken lines are the so-called fish bone deforestation area, and their temporal change should be monitored from space. This area also contains several targets: the fully grown forest; the secondary forest re-grown after the destruction by inundations, rivers, trees in deep water; the deforested area; and pastures. This figure also shows that each target can be identified from σ^0 using the scale bar at the upper image. Fig. 1-3 shows the representative relationship between forest biomass and σ^0 with L-band HH polarization [52]. σ^0 increases as forest biomass increases to 100 tons per hectare and is saturated at σ^0 of -7.7 dB after that. Other examples at different radar parameters (i.e., frequency, incidence angle, and polarization) show linear relationships between σ^0 and the trunk biomass [55],[53]. Thus, the calibrated σ^0 can be useful for measuring the forest biomass and/or trunk biomass. Although the sensitivity depends on the radar parameter, 1 dB may be the accuracy requirement for σ^0 measurement.

Sea ice

Monitoring the sea ice distribution over the ocean is important for the global environment understanding as sea ice acts as cold sources. Its movement should also be monitored for marine safety. Sea ice is classified the first-year ice and the multi-year ice. This distinction is based on the bubbles contained in the ice layers and surface roughness. Discriminating the sea ice from the ocean is necessary to estimate the volume of the cold sources floating in the ocean. Fig. 1-4 shows the possibility of discriminating sea ice in the ocean north of Hokkaido.

Land utilization

A typical example for the visibility (σ^0) difference for the land area is shown in Fig. 1-5 for JERS-1 SAR (L-band HH) and ERS-1 AMI (C-band VV). Mt. Fuji and the surrounding area contain various features such as urban cities, lakes, grassland, an army training area, a snow-capped top of the mountain, and natural forest. Differences in σ^0 should be detected by image interpretation. σ^0 for these areas also differs with frequency.

Soil Moisture

Soil moisture affects the global climate change through the water circulation and the thermal energy exchange between the atmosphere and the land. Measurement of the soil moisture is very desirable for promoting global understanding. Scattering from the land surface depends on the surface roughness and the dielectric constant of the soil moisture. We may estimate the soil moisture of the land surface by measuring σ^0 and knowing an additional parameter (i.e., surface roughness). Fig. 1-7 shows the relationship between σ^0 and soil moistures (% g/g) for two different fields conditions (bare soil and vegetation covered soil) and radar conditions of 5.3 GHz, VV polarization, and incidence angle of 23 degrees [56]. The dielectric constant, and, thus, σ^0 increases as soil moisture increases. Other research at different frequencies, incidence angles, and polarizations, provides similar results [54].

Wind speed

The ocean surface is roughened by wind-driven capillary waves and its developed longer waves. Thus, σ^0 of the ocean surface is related to the wind speed and direction. Most of the good examples are obtained from C and Ku band scatterometer data as shown in Fig. 1-8 [58].

Others

Although the examples are not shown, plant water contents, woody biomass, lava flows, vegetation, and desert can also be identified using σ^0 measurement [57], [60].

As described above, σ^0 must be measured accurately to classify and recognize targets. The requirements for relative and absolute accuracies for σ^0 measurement are summarized by A. Freeman [18], [20], F. Ulaby, and R. Kwok [19] and are shown in Table 1-1. The relative

accuracy is strictly required between 0.5 dB to 1 dB, but the absolute accuracy is slightly relaxed to between 1 dB to 3 dB. We also show the representative error of estimated geophysical parameters that corresponds to 1 dB error in σ^0 measurement in Table 1-2.

Table 1-1. Requirements for the σ^0 measurements [18], [19]

Geophysical parameter	Measurement accuracy	Calibration requirement		
		abs.	rel. (short)	rel. (long)
Ice classification 3 classes winter	Probably correct classification > 80%	2.0	0.5	2.0
Ice motion	Probably correct match > 95%	-	0.5	-
Snow pack water equivalent	< 20 cm* Assumes > 20 cm	1.0	1.0	1.0
Wind speed over ocean	< 20%	1.0	1.0	1.0
Wave height wave energy	System transfer function < 5%	1.0	0.5	0.5
Soil moisture (5 separate levels)	20% variation in each level level (+- 0.3 g/cm3)	1 dB	<0.5 dB	1 dB
Surface roughness	-	1 dB	-	-
Vegetation mapping and monitoring	Biomass density to within 25% leaf area index (LAI) +- 0.5 between 0 and 2	1 dB	<0.5 dB	0.5 dB
Age of lava flows	Accurate classification of three ages classes	3 dB	1 dB	1 dB

Table 1-2. Error of geophysical parameter that corresponds to 1 dB error in σ^0

no.	Item	Error	Measurement range	σ^0 range (dB)		Ref.
1	Forest biomass	20 t/ha	0 - 100 t/ha	-12 -	-7.7	[52]
2	Volume soil moisture(C)	5%	0 - 30%(g/g)	-9 -	-1	[56]
3	Volume soil moisture(L)	4%	0 - 25%(g/g)	-18 -	-10	[54]
4	Bole volume	70 m^3/ha	0 - 250	-10 -	-6	[57]
5	Plant water contents	0.75 kg/m^3	0 - 5 kg/m^3	-13 -	-7	[55]
6	Woody biomass	500 m^3/ha	400 - 2400 m^3/ha	-11 -	-6	[55]
7	Wind speed (Ku) down	10%	0 - 30 m/s	-25 -	-10	[58],[59]

Note that (C), (L), and (Ku) mean the radar frequency band.

Fig. 1-2 JERS-1 SAR image for the Amazon area

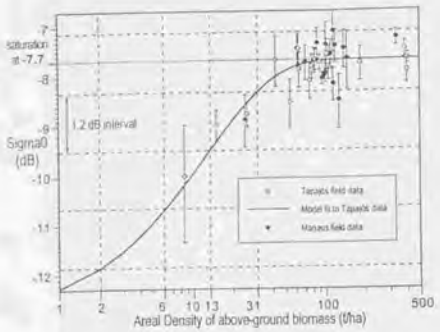

Quantised biomass density retrieval scheme

Fig. 1-3 A representative relationship between biomass and the σ^0 in L-HH (after J. R. Baker [97]).

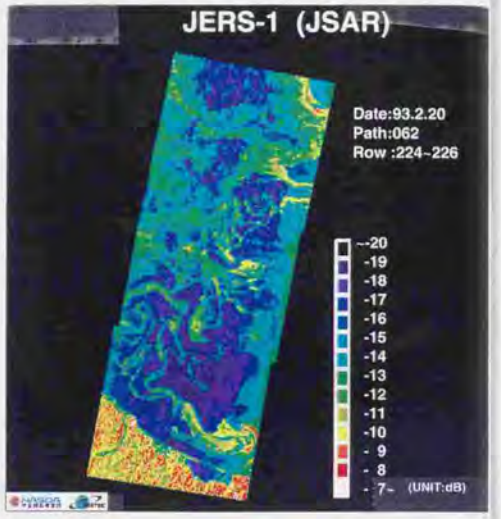

Fig. 1-4. Sea ice at Monbetsu, Hokkaido, Japan.

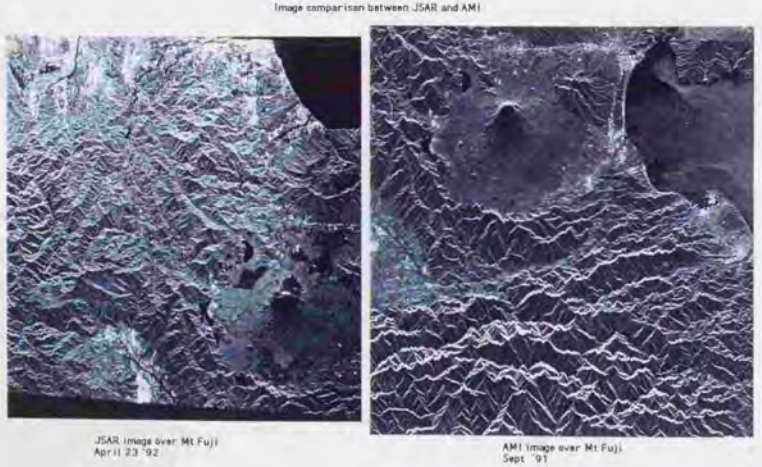

Fig. 1-5. SAR images for the Mt. Fuji area. a) by JERS-1; b) by ERS-1

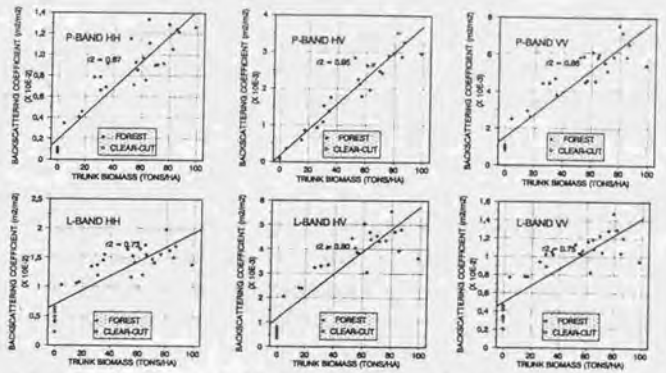

Fig. 1-6. σ^0 at P and L and HH, VV, HV as a function of trunk biomass(after Le Toan [53]).

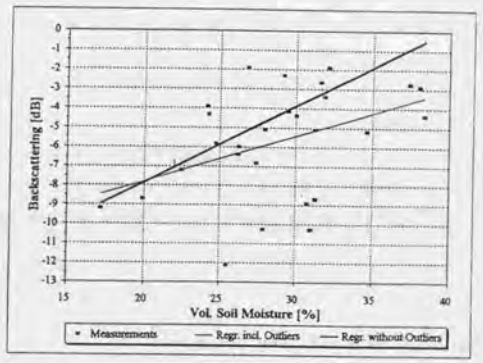

Fig. 1-7 σ^0 at C band and VV as a function of volume soil moisture (after Portmann [56])

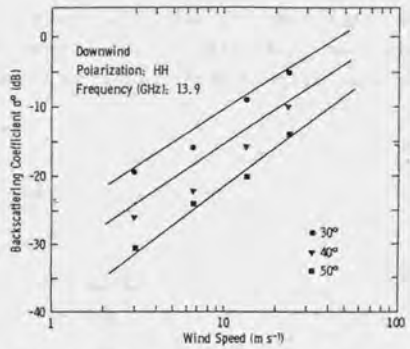

Fig. 1-8 σ^0 at Ku band at HH and downwind as a function of wind speed (after Moore [58]).

1.1.5 SAR artifacts

Aside of the original distortions in the SAR data, such as foreshortening, layover, and shadowing, some artifacts caused by incorrect SAR calibration make the data interpretation difficult. These artifacts are generally twofold: sensor oriented artifacts, and the interference from undesired targets.

1) Sensor oriented artifacts

SAR is ideally a linear system, and the receiving part is composed of a linear receiver and an analogue-to-digital converter. However, the hardware limitations (data transmission bandwidth, receiver dynamic range, etc.) require time-changing attenuators to fit the wide-dynamic-range signal within the receiver sensitivity. They are represented by the sensitivity time control and automatic gain controllers, which are adopted by most of airborne and spaceborne SARs except for AMI, SIR-C/X-SAR, and SIR-B. The antenna pattern and the high transmission signal power improve the signal-to-noise ratio of the target area. The incorrect instrumental characterization and its correction, however, cause several defects, i.e., several weak stripes along the path (Fig. 1-2).

2) Interference from undesired targets

An external signal which shares some or all of the SAR signal bandwidth can be received by the SAR and possibly imaged as brighter targets. Ground transmitters used for ground communication lines, air-traffic monitoring radars, and defense related radars, can be interferers.

1.1.6 Calibration of the SAR data (σ^0) and procedure

We focus on calibrating the SAR, not on canceling the interference from ground radar. As shown in Fig. 1-9, the accuracy of the estimated normalized radar cross section ($\hat{\sigma}^0$) depends on how accurately the temporal (long term and short term during a pulse) SAR characteristic variation and the SAR processor's characteristics can be eliminated from the SAR image power (P_C). For this purpose, an accurate expression of the SAR sensitivity model should be developed.

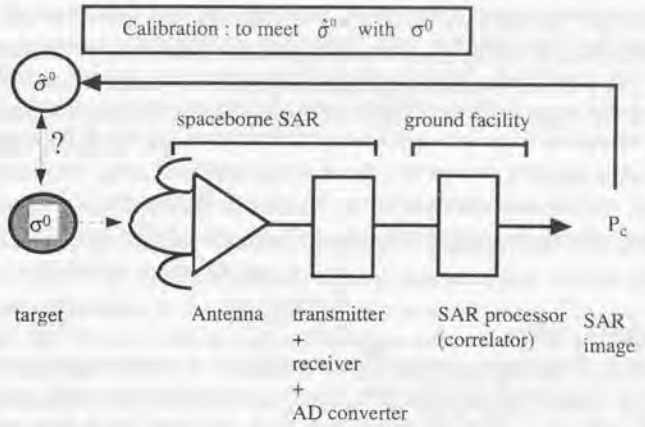

Fig. 1-9. Simplified block diagram of the SAR calibration scheme

The simplified radar equation relating the SAR image power P_C and $\hat{\sigma}^0$ is given by

$$P_C \propto \frac{G_{ant} \cdot G_{rec} \cdot \hat{\sigma}^0}{R^2} + \left(G_{rec} \cdot n_{noise} + n_{saturation}\right) \cdot R \ , \qquad (1.3)$$

where G_{ant} is the antenna pattern, G_{rec} is the receiver gain, R is the slant range, n_{noise} is the thermal noise, and $n_{saturation}$ is the saturation noise. Several factors must be considered to meet the estimated $\hat{\sigma}^0$ with the true σ^0. This procedure is called the SAR calibration, which requires us to determine 1) the antenna elevation pattern, 2) the receiver gain, 3) noise, and 4) the processor gain. Note that SAR calibration deals with the expected behavior of SAR image but not the speckle noise.

Since the Committee on Earth Observation Satellites (CEOS), an international organization to utilize spaceborne sensor data for global monitoring, was established in 1984, a program named "the SAR data CAL/VAL" has progressed through cooperative activities of the Jet Propulsion Laboratory (JPL), Canadian Center for Remote Sensing (CCRS), German Space Agency (DLR), National Space Development Agency of Japan (NASDA), European Space Agency (ESA), French Space Agency (CNES), and other related agencies [21], [22], [23], [24].

SAR correlation power model

The SAR calibration requires an accurate radar equation for SAR images. A. Freeman et. al. [25] developed a simple model which is composed of the coherently amplified signal and

redundancy noise are considered in this model. This model has been widely used for SAR calibration ([45], [26], [27], [28], [29], [30]). Most SARs are designed to prevent saturation in the data. Very strong back scatterers and incorrect receiver gain, however, sometimes saturate the signal, as reported that 1) AMI data is normally saturated over the ocean, 2) also in AMI, 32% of all locations in the near range have a power loss exceeding 0.5 dB [31], [45], and 3) JERS-1 SAR is normally 5% saturated for all images [42], [43], [44]. The model by Freeman et. al. overestimates the signal power if saturation occurs. Therefore, we have developed a new radar equation to cover the saturation noise, which will be described in Chap. 3 of this thesis.

Antenna elevation pattern

A SAR antenna is a large structure in space. The on-ground antenna pattern measurement may differ from the in-flight pattern due to possible anomalies in the deployment and/or vibration during attitude maneuvers. There are several methods for measuring the in-flight antenna pattern using 1) calibrated receivers (Seifert [32], [33]), 2) corner reflectors and active radar calibrators (Dobson et. al. [39]), and 3) flat rainforest data (Moore [34], [35]). The flat Amazon rainforest is a uniform scattering target with almost a constant backscattering coefficient ($=\sigma^0/\cos\theta$). Unless non-uniformities like rivers or mountain wrinkles are excluded and the noise level is considered, however, the pattern may be erroneous. We propose a new antenna pattern estimation method which excludes the non-similarly scattering areas from the SAR data and considers the signal-to-noise ratio. The method will be described in Chap. 4.

Use of the frequency tunable active radar calibrator

An active radar calibrator is a reliable external calibration source that provides a bright impulse response. If the re-transmission signal is frequency-shifted, its response can be moved in the azimuth direction to an area which is not affected by a man-made brighter target. The frequency shift, however, de-focuses SAR. The resultant impulse response looses the power and the resolution is broadened. Use of this ARC was first proposed by Brunfeldt [51], [36], and the location shift was discussed by Lukowski [50] and Fujita [41]. We have theoretically analyzed the mechanism which reduces the peak gain and broadens the resolutions. Based on a comparative study using the truth data, we have proposed a robust calibration method for this ARC. We have also derived a limit for the frequency shift for the resolution evaluation [40]. Our study on the ARC is described in Chap. 5.

SAR calibration using the flat-rainforest and the external calibrators

As an application of the calibration method described in Chapters 3 and 4, we have calibrated JERS-1 SAR data acquired for the Amazon rain forest. We have also obtained a calibration factor (CF) to convert a digital number to σ^0 using external point targets. The stability of two calibration methods, the integral method (Gray et. al. [37]) and the peak method (Ulander

[38]), has been compared. Measured σ^0 was validated using the ARC and trihedral corner reflectors and its error budget has been analyzed. The image quality for the point target has been evaluated. Ground communication lines often interferer with L-band SAR data. A method to exclude such signal from the SAR image is also investigated. The studies will be described in Chap. 6.

Slope corrected σ^0

σ^0 is a quantity per unit area. Two-dimensional terrain gradients cause local variations in the pixel area (A). If σ^0 is generated from the ellipsoid earth assumption, it differs more from the true value. This effect on the SAR calibration was analyzed by Zyl et. al. [48], [49]. They reported that SAR with a pointing angle of 35 degrees may have a maximum σ^0 error of 5 dB. Slope correction methods were proposed by Zyl et. al. and Ulander. Ulander used SAR interferometry to estimate the terrain gradients. We also propose a terrain slope correction method using SAR interferometry. The difference is that 1) flat-earth-corrected fringes are used and 2) orbital error is analyzed. Our study on the slope corrected σ^0 will be described in Chap. 7.

1.2 Outline of the Thesis

We have investigated the methods to measure σ^0 accurately from SAR data. The studies focused on 1) deriving a radar equation considering the saturation and thermal noise, 2) estimating the in-flight antenna elevation pattern, 3) analyzing the applicability of the distributed data for SAR characterization and calibrating the SAR using active radar calibrators, 4) investigating the availability of a frequency tunable active radar calibrator, and 5) obtaining the slope corrected σ^0 using SAR interferometry. The thesis is composed of eight chapters:

Chapter 1 Reviews the SAR calibration, the background of the investigation, and the abstract of the themes dealt with here. The outline of this thesis is also introduced.

Chapter 2 Prepares for subsequent chapters by introducing 1) the principle of SAR imaging; 2) descriptions of the SAR system, SAR processor, and calibration instrument; and 3) current calibration accuracy.

Chapter 3 Discusses saturation and develops a new radar equation to express the SAR correlated signal power including the saturation noise generated by A/D converters.

Chapter 4 Discusses a method to estimate the inflight SAR antenna elevation pattern using natural target data.

Chapter 5 Investigates SAR calibration accuracy using the frequency tunable ARC.

Chapter 6 Discusses methods of characterizing SAR using the rainforest data and investigates defects removal.

Chapter 7 Proposes a method for estimating the σ^0 corrected for the terrain gradients using SAR interferometry.

Chapter 8 Concludes the studies conducted in this thesis.

Fig. 1-10 illustrates the organization of the thesis.

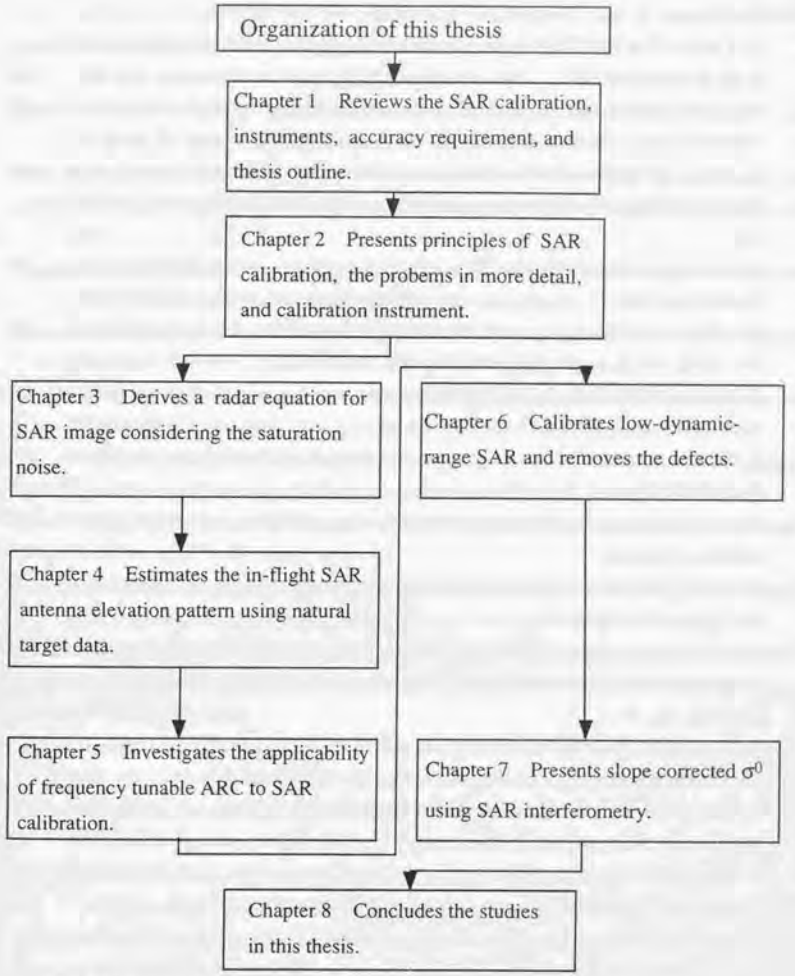

Fig. 1-10. Organization of this thesis

References

[1] R. L. Jordan, "The SEASAT A Synthetic Aperture Radar System," IEEE Oceanic Eng., vol. OE-5, no. 2, pp. 154-163, Apr. 1980.

[2] H. Joyce, R. P. Cox, and F. G. Sawyer, "The active microwave instrumentation for ERS-1," in Proc. IGARSS'84 Symp. (Strasbourg, France), ESP SP-215, pp. 835-840.

[3] Y. Nemoto, H. Nishino, M. Ono, H. Mizutamari, K. Nishikawa, and K. Tanaka, "Japanese Earth Resources Satellite-1 Synthetic Aperture Radar," Proc. of the IEEE., vol. 79, no. 6, pp. 800-809, June 1991.

[4] K. Raney, A. P. Luscombe, E. J. Langham, and S. Ahmed, "Radarsat," Proc. IEEE, vol. 79, no. 6, pp. 839-849, June 1991.

[5] R. L. Jordan, B. L. Huneycutt, and M. Werner, "The SIR-C/X-SAR synthetic aperture radar system," Proc. IEEE, vol. 79, no. 4, pp. 827- 838, June 1991.

[6] R. Kwok, and W. T. K. Johnson, "Block Adaptive Quantization of Magellan SAR Data," IEEE Trans. Geosci. Remote Sensing, vol. 27, no. 4, pp. 375-383, July 1989.

[7] C. Elachi, "Spaceborne Remote sensing: Application and Techniques," IEEE press, 1988.

[8] F. Ulaby, R.Moore, A. Fung, "Microwave Remote Sensing, Active and Passive," Vol. 2, Radar Remote sensing and surface scattering and emission theory, Chap 9, pp. 630-740, Addison-Wesley Publishing Company.

[9] C. Wiley et. al., "Pulsed Doppler Radar Methods and Apparatus," U.S. Patent 3,196,436, Field August 13, 1954, patented July 20 1965.

[10] F. Ulaby, R. Moore, A. Fung, "Microwave Remote Sensing, Active and Passive," Vol. 1, Radar Remote sensing and surface scattering and emission theory, Chap 1, pp. 8, Addison-Wesley Publishing Company.

[11] C. Wu, "A digital approach to produce imagery from SAR data," presented at the AIAA Syst. Design Driven by Sensors Conf., aper. no. 76-968, Pasadena, Ca, OCT. 18-20, 1976.

[12] C. Caffirio, C. Prati, and F. Rocca, "SAR Data Focusing Using Seismic Migration Techniques," IEEE TAES, vol. 27, no. 2, pp. 194-207, March 1991.

[13] R. K. Raney, H. Runge, R. Bamler, I. G. Cunning, and F H. Wong, "Precision SAR Processing Using Chirp Scaling," IEEE Trans. Geosci. Remote Sensing, vol. 32, no. 4, pp. 786-799, July 1994.

[14] J. Way, and E. A. Smith, "The Evolution of Synthetic Aperture Radar Systems and their Progression to the EOS SAR," IEEE Trans. Geosci. Remote Sensing, vol. 29, no. 6, pp. 962-985, Nov. 1991.

[15] S. Ahmed, H. R. Warren, M. D. Symonds, and R. P. COX, "The Radarsat System," IEEE. Trans. Geosci. Remote Sensing, vol. 28, no. 4, pp. 598-602, July 1990.

[16] K. Yoneyama, T. Koizumi, T. Suzuki, R. Kuramasu, T. Araki, C. Ishida, M. Kobayashi, and O. Kakuichi, "JERS-1 Development Status," 40th Congress of the International Astronautical Federation, 1989, Beijing, China, IAF-89-118.

[17] J. P. Ford, R. G. Blom, J. A. Crisp, C. Elachi, T. G. Farr, R. S. Saunders, E. E. Theilig, S. D. Wall, and S. B. Yewell, "Spaceborne Radar Observations, A guide for Magellan Radar-Image Analysis," Dec. 15 1989.

[18] A. Freeman, "The need for SAR calibration," Proc. in IGARSS, vol 1, July 10 - 14, 1989 Vancouver, CANADA, pp. 230-233.

[19] EOS SAR Instrument Panel Report, NASA, Publication, 1988.

[20] A. Freeman, J. C. Curlander, T. C. Dubois, P. D. and J. Klein, "SIR-C Calibration Workshop Report," JPL Center for Radar Studies Publication, No. 88-003, Nov. 1988.

[21] Committee on Earth Observation Satellites, "Strategic Plan of the working group on calibration and validation - Leadership to Ensure High-quality Earth Observation Data: A Strategic Vision," September 1996.

[22] SAR calibration Workshop Proceedings, 20-24, September, 1993, ESTEC, Noordwijk, the Netherlands. CEOS calibration/validation working group, SAR calibration subgroup.

[23] Proceedings of the SAR calibration workshop, 28- 30, September 1994, the University of Michigan, USA, CEOS Calibration/Validation working group SAR calibration subgroup.

[24] GEC-Marconi, "SAR data quality assessment and rectification final report," ESA contract, no. 6635/86/HGE-I, March 1988.

[25] A. Freeman and J. C. Curlander, "Radiometric correction and calibration of SAR images," Photogrammetric Engineering and Remote Sensing, vol. 55, no. 9, pp. 1295-1301, 1989.

[26] M. Shimada, "Radiometric and Geometric Calibration of JERS-1 SAR," Advanced in Space Research, vol. 17, no. 1, pp. 79-88, 1996.

[27] M. Shimada, "Absolute Calibration of JERS-1 SAR and Image Quality (Japanese)," Japan Remote Sensing Society, vol. 14, no. 2, pp. 35-47, 1994.

[28] A. Freeman, M. Alves, B. Chapman, J. Cruz, Y. Kim, S. Shaffer, J. Sun, E. Turner, and K. Sarabandi, "SIR-C Data Quality and Calibration Results," IEEE Trans. Geosci. Remote Sensing, vol. 33, no. 4, pp. 848- 857, July 1995.

[29] A. Freeman, J. C. Curlander, F. Heel, M. Zink, P. Hoogeboom, J. Groot, A. Dawkins, J. Baker, M. Reich, and H. Lentz, "Preliminary results of the multi-sensor, multi-polarization SAR calibration experiments in Europe 1989," Proc. IGARSS '90(Washington, USA), May 1990, pp. 783-787.

[30] M. Zink, F. Heel, and H. Kietzmann, "The Oberpfaffenhofen SAR Calibration Experiment of 1989," Journal of Electromagnetic Waves and Applications, vol. 5, no. 9, pp. 935 - 951, 1991.

[31] P. J. Meadows, and P. A. Write, "ERS-1 synthetic aperture radar analogue to digital converter saturation," Proceedings of the CEOS SAR calibration workshop, 28- 30, September, 1994, The University of Michigan, pp.. 24-37.

[32] P. Seifert, H. Lentz, M. Zink, and F. Heel, "Ground-Based Measurements of Inflight Antenna Patterns for Imaging Radar Systems," IEEE Trans. Geosci. Remote Sensing, vol. 30, no. 6, pp. 1131-1136, 1992.

[33] P. Seifert, M. Zink, and H. Lentz, "ERS-1 Preliminary Antenna Elevation Pattern Measured by Ground-receiver," Proceedings of the first ERS-1 Symposium, 4-6 November 1992, Cannes, ESA SP-359, vol. 1, pp. 157- 159.

[34] R. K. Moore and M. Hemmat, "Determination of the vertical pattern of the SIR-B antenna," Int. J. Remote Sensing, vol.9, no.5, pp. 839-847, 1988.

[35] R. K. Moore, V. S. Westmoreland, D. Frank, and M. Hemmat, "Determining the vertical antenna pattern of a spaceborne SAR by observation of uniform targets," Proc. IGARSS '86 Symp., Zurich, Switzerland, vol. 1, pp. 469-472.

[36] D. R. Brunfeldt and F. T. Ulaby, "Active Reflector for Radar Calibration," IEEE Trans. Geosci. Remote Sensing, vol. GE-22, no. 2, pp. 165-169, March 1984.

[37] A. L. Gray, P. W. Vachon, C. E. Livingstone, and T. I. Lukowski, "Synthetic Aperture Radar Calibration Using Reference Reflectors," IEEE Trans. Geosci. Remote Sensing, vol. 28, no. 3, pp. 374-383, May 1990.

[38] L. M. H. Ulander, R. K. Hawkins, C. E. Livingstone, and T. I. Lukowski, "Absolute Radiometric Calibration of the CCRS SAR," IEEE Trans. Geosci. Remote Sensing, vol. 29, no. 6, pp. 922-933, Nov. 1991.

[39]. M. C. Dobson, F. T. Ulaby, D. R. Brunfeldt, and D. N. Held, "External calibration of SIR-B imagery with area extended and point targets," IEEE Trans. Geosci. Remote Sensing, vol. 24, no.4, pp. 453-461, 1986.

[40] M. Shimada, H. Oaku, and M. Nakai, "Calibration Using Frequency-Tunable Active Radar Calibrators," IEEE Trans. Geosci Remote Sensing, 1998, in press.

[41] M. Fujita, "An Active Reflector for SAR Calibration Having a Frequency Shift Capability," IEICE TRANS. COMMUN., vol. E75-B, no. 8, pp. 791-793, Aug. 1992.

[42] M. Shimada, M. Nakai, and S. Kawase, "Inflight Evaluation of L band SAR of JERS-1," Canadian Journal of Remote Sensing, vol. 19, no. 3, ISSN 0703-8992, pp. 247- 258, Aug. 1993.

[43] M. Shimada, "Inflight Evaluation of L band SAR of Japanese Earth Resources Satellite-1," Adv. Space Res. vol. 14, no. 3, pp. 231- 240, 1994.

[44] M. Shimada, M. Nakai, "First result of the SAR characterization (in Japanese)," Technical Report of IECE SANE92-58, Nov. 1992.

[45] H. Laur, P. Meadows, J. I. Sanchez, E. Dwyer, "ERS-1 SAR radiometric Calibration," 20-24 September 1993, ESTEC, Noordwijk, the Netherlands. CEOS calibration-validation working group SAR calibration sub-group, pp. 257- 281.

[46] J. B. Cimino, C. Elachi, and M. Settle, "SIR-B the second shuttle imaging radar experiment," IEEE Trans. Geosci. Remote Sensing, vol. GRS-24, no. 4, pp. 445-452, July 1986.

[47] B. L. Huneycutt, "Spaceborne imaging radar-C instrument," IEEE Trans. Geosci. Remote Sensing, vol. 27, no. 2, pp. 164-169, March 1989.

[48] J. J. V. Zyl, B. D. Chapman, P. Dubois, and J. Shi, "The Effect of Topography on SAR Calibration," IEEE Trans. Geosci. Remote Sensing., vol. 31, no. 5, pp. 1036-1043, Sept. 1993.

[49] L. M. H. Ulander, "Radiometric Slope Correction of Synthetic Aperture Radar Images," IEEE Trans. Geosci. Remote Sensing, vol. 34, no. 5, pp. 1115-1122, Sept. 1996.

[50] T. I. Lukowski, R. K. Hawkins, B. Brisco, R. Brown, R. Ford, and P.S. Daleman, "The Saskatoon SAR Calibration Experiment," in proc. IGARSS'89, Remote sensing: pp. 254-257, Vancouver, Canada.

[51] D. R. Brunfeldt, "SAR Response to modulated target," in proc. IGARSS'89, Remote sensing: pp. 2901 -2905, College park, Maryland.

[52] A. Luckman, J. Baker, M. Honzak, and R. Lucas, "Tropical Forest Biomass Density Estimation Using JERS-1 SAR: Seasonal Variation, Confidence Limits, and Application to Image Mosaics," Remote Sensing Environment, 63: 126-139 (1998).

[53] T. Le Toan, A. Beaudoin, J. Riom, and D. Guyon, "Relating Forest Biomass to SAR Data," IEEE Trans. Geosci. Remote Sensing, vol. 30, no. 2, pp. 403-411, March 1992.

[54] S. Mohan, N. S. Mehta, R. L. Mehta, P. Patel, D. R. Rajak, and H. S. Srivastava, "Evaluation of JERS-1 SAR data for soil moisture and crop studies," in proc of final report of JERS-1/ERS-1 system verification program, pp. 2-55- 64, march 1995.

[55] S. Paloscia, P. Pampaloni, and S. Sigismondi, "Effects of crop biomass on JERS-1 SAR backscatter," in proc of final report of JERS-1/ERS-1 system verification program, pp. 2-3- 8, march 1995.

[56] F. Portmann, H-G Mendel, "Soil Moisture Estimation in Hydrological Mesoscale Modeling using ERS SAR data," in proc. the third symposium on Space at the service of our environment, Florence Italy, 14-21 march. 1996, pp. 86 - 92.

[57] H. Israelsson and J. Askne, "JERS-1 SAR analysis of boreal forest biomass," in proc of final report of JERS-1/ERS-1 system verification program, pp. 2-38- 45, march 1995.

[58] F. T. Ulaby, R. K. Moore, and A. K. Fung, "Microwave remote sensing : Active and Passive," Vol. II, Addison-Wesley, 1982.

[59] H. Hirosawa, "Some quantitative expressions on the SAR image quality," Japan remote sensing society, vol. 5, pp. 225, 1985 (2).

[60] ERSDAC, "Synthetic Aperture Radar: Chapter 2,1992.

CHAPTER 2 BACKGROUND OF SAR CALIBRATION

2.1 Introduction

Following the introduction given in Chap. 1, we review the following items in this chapter: 1) SAR imaging principle, 2) SAR calibration, 3) SAR instruments, 4) SAR processing algorithms, 5) Calibration instruments, 6) Statistics of the SAR data, and 7) Status of calibration accuracy.

2.2 SAR Imaging Principles

SAR imaging, a two-dimensional correlation of the SAR raw data with a reference function, have produced a high-resolution image of 8 to 20 m in the recent spaceborne SARs, 5 m for airborne SARs, and 150 m in the Magellan [1], [2], [3], [4], [5]. Obviously, the image focusing depends on how accurately the reference function is modeled by a transmission signal and a phase history between the SAR and the target.

Range correlation

SAR transmits cascaded linear FM pulses with a bandwidth "B_w" over a pulse duration "τ." Each transmission signal, $S_t(t)$, is expressed by

$$S_t(t) = A(t)e^{2\pi j\left(f_0 t + \frac{B_w}{2\tau}t^2\right)}, \tag{2.1}$$

where f_0 is the carrier frequency and t is the time. The amplitude, A(t), is non zero only when $|t| <= \tau/2$ else $A(t) = 0$. The cosine component is shown in Fig. 2-1. The received signal, $S_r(t)$, from the target which is located at slant range R from the SAR is expressed by

$$S_r(t) = S_t\left(t - \frac{2R}{C}\right)A_{att}e^{-j\delta}. \tag{2.2}$$

Note that we discuss the imaging principle here and ignore the amplitude variation on the slant range, i.e., antenna pattern, range attenuation, scattering amplitude of the target. The received signal is represented by the transmission signal time-shifted by 2R/C, multiplied by the attenuation (A_{att}) due to free space and the atmospheric loss, and multiplied also by the phase change at the target (δ). Because the transmission signal phase (where, phase is the distance between the SAR and the target) should be preserved by each scatterer (ignoring the phase change at the target), one dimensional correlation with the complex conjugate of the transmission signal makes the signal focused in range, i.e.,

$$S_{rc}(R) = \frac{1}{\tau}\int_{-\frac{\tau}{2}}^{\frac{\tau}{2}} S_r(t+t')S_t^*(t')dt'$$
$$= \frac{\sin\left(2\pi B_w \cdot \frac{R-R_0}{C}\right)}{2\pi B_w \cdot \frac{R-R_0}{C}} e^{-\frac{4R}{C}f_0\pi j} A_{att}e^{-j\delta}, \tag{2.3}$$

where S_{rc} is the range correlated signal; R is the slant range; C is the Light speed; "*" is the complex conjugate; and f_0 is the transmission frequency. This formula suggests that the range correlation gives a peak at $R = R_0$ and the signal decays as a sinc function. A half power point which equals half the peak power is given at $(R-R_0) = 0.886C/4B_w$ (A half power point of the squared sinc function is 1.39). Therefore, the range resolution containing more than half power is given by $0.886*C/2B_w$, which is simply written by $C/2B_w$.

Azimuth correlation

Some thousand pulses hit the target contiguously while the SAR antenna beam covers the point. Within this period, the distance between SAR and the target, R(T), changes as

$$R(T) \cong R_0 + \frac{V^2}{2R_0}T^2. \tag{2.4}$$

Although the range curvature migration correction is a most difficult task, it is not discussed in this thesis. Ignoring the sinc modulation introduced by range compression and the target and atmosphere dependent terms, we pick the exponential term of equation (2.3):

$$S_{rc}(R) \propto e^{-2\pi j\frac{V^2}{2R_0}T^2} e^{-4\pi j\frac{R_0}{\lambda}}. \tag{2.5}$$

This is also a linear FM signal generated by the relative motion between SAR and the target. If the SAR antenna is length L in azimuth, the illumination area size in azimuth is $R_0*\lambda/L$, which corresponds to a correlation time of $R_0*\lambda/LV$. Including the range correlation, the final output, $S_{rca}(R)$, is expressed by

$$S_{rca}(R) = \frac{\sin\left(2\pi B_w \cdot \frac{R-R_0}{C}\right)}{2\pi B_w \cdot \frac{R-R_0}{C}} \frac{\sin\left\{\pi\left(\frac{2V^2}{\lambda R_0}\right)\left(\frac{R_0\lambda}{LV}\right)\left(\frac{x-x_0}{V}\right)\right\}}{\left\{\pi\left(\frac{2V^2}{\lambda R_0}\right)\left(\frac{R_0\lambda}{LV}\right)\left(\frac{x-x_0}{V}\right)\right\}} e^{-\frac{4R_0}{C}f_0\pi j} A_{att}e^{-j\delta}. \tag{2.6}$$

where x and x_0 are the location of the target, and V is the satellite speed. Similarly, the second term gives the half power resolution by 0.886*L/2. Therefore, the range and azimuth correlation provides the two-dimensional high-resolution images. The actual processing is somewhat different for the range migration correction and the reduction of the azimuth reference function.

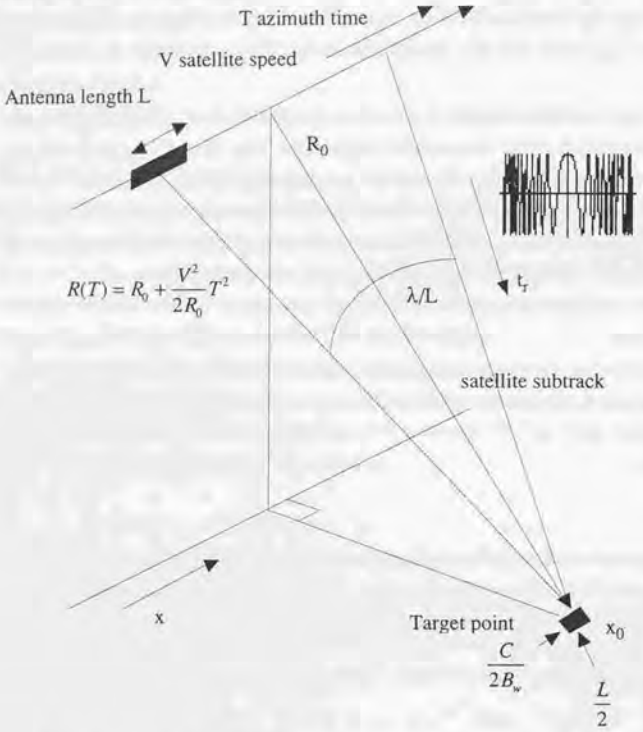

Fig. 2-1. SAR coordinate system and full resolution image.

2.3 Detailed Discussion of the SAR Calibration

We will review the current SAR calibration procedure in more detail and rearrange the problems. We show a detailed block diagram of the SAR calibration procedure in Fig. 2-2.

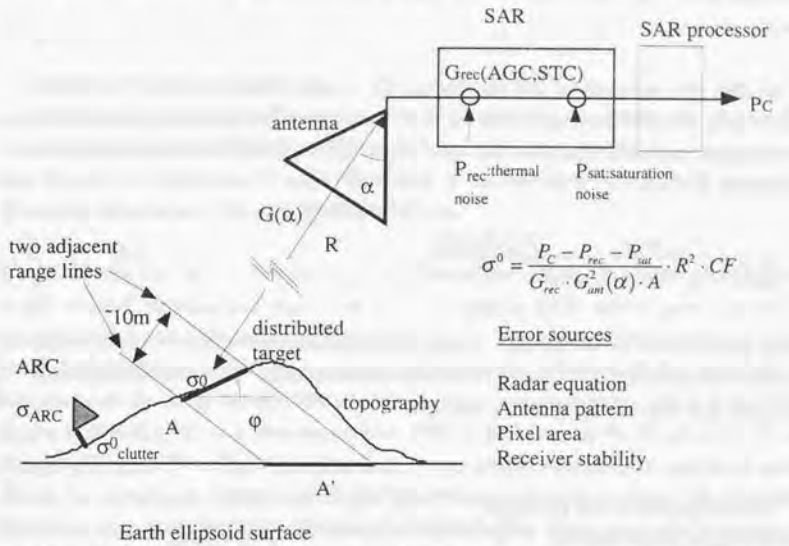

Fig. 2-2. Block diagram of σ^0 measurement from the SAR data. Error sources are saturation noise model P_{sat}, antenna elevation pattern $G(\alpha)$, pixel area A, receiver gain model G_{rec}, and stability of reflectors. The calibration factor is determined by using the impulse response of a reflector. Values with ' are for reflectors.

2.3.1 σ^0 Measurement and Current SAR Calibration

Speckle noise, caused by the fading of scatterers included within a resolution cell, is the largest obstacle for SAR data interpretation. It changes σ^0 of two adjacent pixels more than several dB (this amount heavily depends on the number of looks and the distribution of the scatterers; 200-look image for similarly distributed scatterers gives 1 dB of variation [73]). SAR calibration is defined to deal with the speckle-free SAR data to which some smoothing filter is applied. Under this condition, σ^0 of each pixel is expressed by (see Fig. 2-2)

$$\sigma^0 = \frac{P_C - P_{rec} - P_{sat}}{G_{rec} G_{ant}^2(\alpha) A} R^2 \cdot CF, \qquad (2.7)$$

where P_C is the correlation power (expectation), P_{rec} is the receiver noise (expectation), P_{sat} is the saturation noise (expectation), G_{rec} is the receiver gain, $G_{ant}(\alpha)$ is the two-way antenna

elevation pattern, α is the off-nadir angle, R is the slant range, and CF is the calibration factor that connects the SAR image with σ^0. SAR calibration is defined to determine 1) the correlation power model which includes noise power, 2) antenna elevation pattern, 3) receiver gain characteristics, 4) pixel area (if obtained), and 5) calibration factor, CF, so that σ^0 can be estimated accurately.

After the first four components are determined, CF is determined by using the impulse responses from the reference signal sources (e.g., the active radar calibrator and trihedral corner reflectors) and their radar cross sections. Since the SAR is the linear system, we have the calibration factor, CF:

$$CF = \frac{\sigma_{ARC}\sin\theta}{\iint\left(P_C' - P_{rec} - P_{sat} - P_{clutter}\right)dA}\frac{G_{rec}G_{ant}^2(\alpha')}{R^2}, \tag{2.8}$$

where the prime values are for the ARC, $P_{clutter}$ is the correlation power for the clutter, σ_{ARC} is the radar cross section of ARC, and θ is the local incidence angle. First, CFs are calculated for all ARCs, and their average gives the final CF.

2.3.2 Rearrangement of the Problems

SAR correlation power model

SAR calibration requires an accurate model for the correlated image power. The current understanding (A. Freeman [6]) is as follows. The received signal (after A/D conversion) is composed of the pure signals from a point target or a distributed target (composed of a large number of point targets with small backscattering coefficient), and the noise (the receiver thermal noise and the ADC redundancy noise). As long as the saturation does not occur at ADC, different (but constant) correlation gains amplify the pure signal and noise. The pure signal is correlated in voltage with the gain, C_G, which is roughly the product of the number of the range samples (N_{rg}) and the number of azimuth samples (N_{az}). The pure signal power is then amplified by C_G^2.

The noise is a stationary random process, so, the correlation sums up the noise power incoherently and increases it by ~C_G. If the azimuth resolution is maintained constant over the full swath, N_{az} should be proportional to the slant range (R) (because the same Doppler bandwidth should be maintained over a swath). As a result, the correlated power (P_c) is composed of a pure signal term inversely proportional to R^2 and the noise term proportional to R (see Eq.(2.9), where K_s, K_s', K_n, and K_n' are constants).

$$\begin{aligned} P_c &\equiv K_s\frac{C_G^2}{R^4} + K_n C_G \\ &= K_s\frac{\left(N_{az}N_{rg}\right)^2}{R^4} + K_n N_{az}N_{rg} \\ &= K_s\frac{1}{R^2} + K_n' \cdot R \end{aligned} \tag{2.9}$$

Generally, the antenna elevation pattern and other receiver gain controllers change the received signal intensity within a sampling window (~ several hundred micro seconds), and this should be corrected before range correlation. If the saturation occur at A/D converters, this model overestimates the correlated signal power.

To prevent the saturation, most SARs prepare four or five bits ADCs, or some employ the block floating pointing quantizer (SIR-C and Magellan SAR) and/or gain controllers (automatic gain controller and sensitivity time control). Even so, very strong backscatter and incorrect receiver gain sometimes saturate the signal, as reported that AMI data are normally saturated over the ocean and that 32% of all locations at near range have a power loss greater than 0.5 dB [41], [55]. It is also reported that JERS-1 SAR is normally 5% saturated for all images [53], [32], [54]. Therefore, theoretical power model considering the saturation noise should be developed. Some approaches have been developed to solve this problem. Meadows uses a look-up table which connects the correlated image power and the standard deviation of the corresponding raw data [41]. Cooper changed the scale factor to express the non-linearity of the ADC saturation [42]. Shimada, as presented in this thesis, has derived the correlation power as a function of the local saturation rate and has used it to correct the power loss [43], [72].

Antenna elevation pattern

The antenna elevation pattern ($G(\alpha)$) is a vital element for the calibration. Most SAR antennas have large structures, of 11.9 m in along track by 2.2 m in cross track for JERS-1 SAR, after several sub-paddles being deployed in space. The on-ground antenna pattern is usually estimated by combining each sub-paddle's actual measurement and the antenna synthesis theory. Such a pattern may differ from the true pattern in flight due to possible anomalies in the antenna deployment and/or vibration during attitude maneuvers. From these points of view, several methods for measuring the in-flight SAR antenna patterns were proposed. Seifert [44], [26] used many calibrated receivers across the imaging swath and obtained a two-dimensional measurement (range and azimuth) with an accuracy of 0.5 dB. Moore [45], [46] and Shimada [47], [56] used the Amazon rainforest images, where differences are in the data screening, radar equation, and error analysis. The Amazon rainforest has an almost constant backscattering coefficient (γ), defined as $\sigma^0/\cos(\theta)$ in a flat

plane. Manipulation of the radar equation for those images provides the better results within an accuracy of less than 0.1 dB. Dobson et. al. [49] have shown that point targets, such as corner reflectors or active radar calibrators [50], can be used to measure the elevation antenna pattern accurately. The airborne SAR's elevation pattern was estimated using natural targets by Hawkins [48].

Use of the Frequency tunable active radar calibrator

Absolute SAR calibration is highly desired to ensure valid research results derived from the SAR data. A calibration factor which translates the SAR data (8 bit, 16 bit, or more digital number) to the normalized radar cross section (NRCS or σ^0) can be obtained by using the calibration device deployed on the ground. There are two methods for the calibration; one is the integration method that relates the two-dimensional integration of IRF of the reference point target to the corresponding σ^0, and the other is the peak method that relates the IRF's peak to the σ^0 [29], [61], [62], [53], [28], [55], [19], [63]. Detailed error analyses for these two methods were presented by Ulander [70] and Gray et. al. [29]. Both methods require the subtraction of the averaged background intensity from the isolated IRF for the calibration device.

A corner reflector must be deployed in a wide and dark intensity background area. Desert and dry land are the best areas. A corner reflector with a smaller σ may be a reliable calibration instrument [62], [53], [19] since it has a relatively larger signal-to-clutter ratio for such an area. It is difficult to find such places in small, developed countries as Japan. An ARC can eliminate the background condition requirement because it can provide a larger σ. Its flat surface may, however, compete with the re-transmitted signal as it works as a reflector. Another serious problem is to find an area free from interference from brighter man-made targets, i.e., buildings, houses, highways, and automobiles. From these reasons, an ARC which is able to displace its response location is very desirable in order to provide a highly qualified IRF and its resultant calibration accuracy.

SAR imaging correlates the raw data with the two-dimensional reference function, the azimuth component of which describes the phase history between the SAR and the target at a constant range in the base band, and the range component of which describes the phase history over the pulse transmission bandwidth. It is possible to actively displace the calibration device response by modifying the re-transmission signal properties. Two methods are proposed: the frequency-shifting method and the time-shifting method. The frequency-shifting method adds a constant frequency to the re-transmitted signal from the ARC and changes the received Doppler frequency. The resultant impulse response moves in the azimuth direction. This concept was pioneered by Brunfeldt in the early 1980s' when he was

associated with the University of Kansas [68], [50]. Such an ARC was implemented in a transponder with a phase shifter [52], [59], [60], [69]. The time-shifting method delays the signal transmission from the ARC and moves the impulse response in the range direction [64], [61], [65], [65], [66], [67]. Both methods are very effective for shifting the ARC appearance. However, an avoidable mismatch with the reference function should be considered because it degrades the impulse response function and resulting calibration accuracy.

Several frequency tunable ARCs have been developed and evaluated mainly for the location shift accuracy [52], [59]. The disadvantage of correlation gain loss has been less discussed [67]. Shimada et. al. discussed the gain loss theoretically and analyzed the impulse response [51]. Chapter 5 in this thesis presents a theoretical and experimental evaluation concerning the location shift, correlation gain loss, and resolution broadening caused by the frequency shift.

Terrain Slope Corrected σ^0

The area illuminated by the SAR antenna beam (strictly, a beam corresponds to the range-azimuth correlated high-resolution beam) changes with the local topography (two-dimensional gradients). While σ^0 is defined as a unit-area quantity, the flat earth corrected σ^0 deviates from the true σ^0 that is corrected for the local gradients in two ways. First, the antenna elevation pattern is incorrectly estimated for the target position. Second, the tangential plane at the target area differs from that on the flat earth. The first way affects low-altitude SARs (i.e., airborne SARs) more. The second affects both airborne and spaceborne SARs [57], [58].

Zyl et. al. [57] first published error analyses for the airborne SAR (AIRSAR) and the spaceborne SAR (ERS-1 AMI) using a digital elevation model (DEM) prepared on the ground. In their article, it is stated that σ^0 deviates more for small-incidence-angle SAR than large-incidence-angle SAR (i.e., a typical value of 8 dB or more for ERS-1 which has an incidence angle of 23 degrees, and 3.5 dB for JERS-1 SAR which is the incidence angle of 40 degrees) and warned that the slope correction factor of the σ^0 was greater than the calibration accuracy of the σ^0 which is not corrected for the topography. Ulander [58] first proposed the use of the SAR interferometry technique for this correction. He described how the slope correction can be performed for a non-singular area, which excludes the layovers. He used the zero-padded FFT to estimate the two-dimensional local gradients, and derived an estimation error model for the slope correction factor. He also pointed out the importance of using the two-dimensional surface gradients for calculating the local surface normal vector.

We have developed another method using the SAR interferometry technique to derive the slope correction factor. Two factors are known to influence the slope correction factor: the estimation of the local instantaneous frequencies which takes very much computation time for the FFT and the accuracy of the restituted orbit vectors. We improved these two points by employing a fast processing for the frequency calculations (not using the FFT estimation) and by constructing an error model including the phase measurement error and the satellite position error. We have applied this method to correct JERS-1 SAR images and have achieved slope correction with an accuracy of 0.27 dB. Chapter 7 of this thesis treats the issue related to the terrain slope corrected σ^0.

2.3.3 Consideration of accuracy requirements for σ^0 measurements

Table 1-1 in Chapter 1 summarized the accuracy requirements for σ^0 measurements from the user point of view, and it showed that the requirements varied from 1.0 dB to 3.0 dB, depending on the target. Measurement accuracy of σ^0 depends on those terms constituting (2.7), e.g., CF, G_{rec}, G_{ant}, A, and P_C. The statistical behavior of the scatterers that are included in the target and their fading deviate P_C as well as σ^0. Originally, σ^0 is defined as an expectation and the uniform and widely distributed target only provides it accurately. Thus, we deal with P_c as an expectation , and specify σ^0 accuracy as the product of four terms:

$$\Delta\left(CF / G_{rec} G_{ant}^2 A\right). \tag{2.10}$$

Consequently, the requirement becomes independent of σ^0. If the SAR is linear within the measurable range (this is the normal case), σ^0 accuracy is described by (2.10) at a known signal level. If the SAR is not linear, i.e., due to the saturation, the accuracy can be estimated by the maximum slope deviation from 1.0 and (2.10) at a known signal level (at high signal-to-noise ratio). Measurement requirements for the terrain gradient can be set individually. We therefore establish the following accuracy requirement instead of σ^0 in Table 2-1. We should note that the noise equivalent normalized radar cross section, σ_{ne}^0, is the lowest measurable σ^0, and is given by $\sigma_{ne}^0 = \left(P_{rec} + P_{sat}\right) R^2 CF / G_{rec} G_{ant}^2 A$.

Table 2-1 Rearranged accuracy requirement

	Item	Description and requirement
1	Stripes in range	Should be eliminated as much as possible.
		-> ΔG_{ant} < 0.1 dB
2.	Gradual intensity change in azimuth	
		Should be corrected.
3.	Terrain correction	Not necessary for the flat land and the ocean.
		Necessary for the moderate and high leaf areas.
		-> A < 0.2 dB
4.	Slope deviation	Δslope < 2% for σ^0 dynamic range of 50 dB
		This restricts σ^0 error less than 1.0 dB
	Standard deviation	< 1.0 dB at known signal level

Note that we will verify the real σ^0 accuracy in Chapter 6.

2.3.4 Definition of SAR validation

Within a measurable σ^0 range (larger than σ^0_{ne}), the true σ^0 and the measured (estimated) σ^0 are related linearly in the saturation-free case. In the saturation case, the proposed method overestimates the σ^0 at low signal-to-clutter ratios, and the current method underestimates the σ^0 for all the range (see Fig. 2-3 and Chap. 3). We will verify the measured σ^0 using the following procedure:

i) Determine the calibration factor from (2.8) using the active radar calibrator's responses in SAR image and its radar cross sections;
ii) Convert the responses of ARCs and corner reflectors in the SAR image to σ^0s using (2.7) and the calibration factor, then compare them with the true values, which are the radar cross sections divided by a pixel area;
iii) Use at least two different radar cross sections;
iv) Calculate the variance of the differences and the linearity;
v) Measure the intensity variation in along and across track to evaluate the saturation and antenna pattern correction errors.

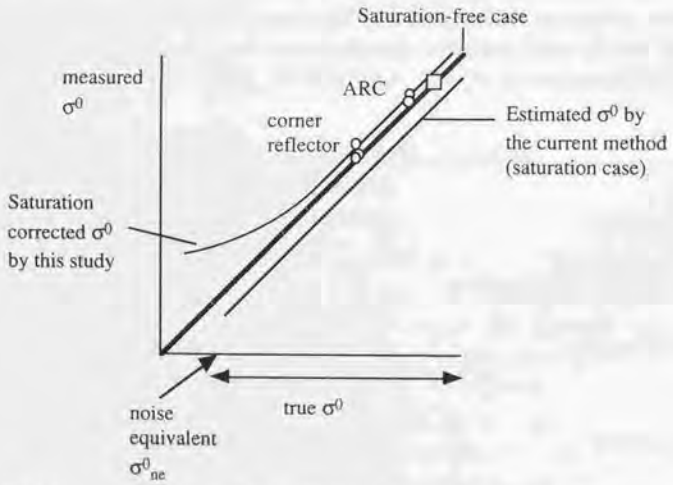

Fig. 2-3 Block diagram of the SAR validation. Here, σ^0_{ne} is subtracted.

2.4 SAR Instruments

The SAR generally consists of four components: transmitter, antenna, receiver, and signal processor. Among the typical SARs ever developed (Table 2-2), we here choose the JERS-1 SAR to introduce the SAR's functionality [7]. Most of the basic functions are the same as for other SARs, besides the JERS-1 SAR has two gain controllers in the receiver, which enables 3-bit digitization of the observation data and results small data transmission bandwidth of 60 MHz. An artist concept of JERS-1 and its simplified block diagram are shown in Figs 2-4 and 2-5. The following summarizes the key specification of the four components.

Transmitter generates the cascaded transmission pulses. Each pulse is frequency-modulated (chirp modulated) within the pulsewidth of 35 μs, amplified to 325 W, and sent to the antenna at the pulse repetition frequency of 1555 Hz. A pulse is generated by a surface acoustic wave (SAW) instrument.

Antenna is composed of eight 2.2 m x 2 m sub-paddles, each of which contains 128 planar patches. This produces a 3 dB down beamwidth of 5.4 degrees in range and 0.98 degrees in azimuth. Fig. 2-4 shows that the deployed antenna has 12.2 m length in the along track direction.

Receiver amplifies the received signal using the low noise amplifier (LNA), and demodulates it with the Coherent Oscillator's output. The level is always adjusted to around 0 dBm by changing the attenuator in one dB steps (the automatic gain control (AGC)). The sensitivity time control (STC) cancels the antenna pattern related power changes within the observation window (360 μs). Note that AGC and STC have become sources of difficulty in data calibration.

Signal processor divides the incoming signal into the in-phase component (I) and the quad-phase component (Q). The latter phase is made 90 degree ahead of the I component's phase using a phase shifter. These signals are digitized in a 3-bit and sampled by 17.076 MHz.

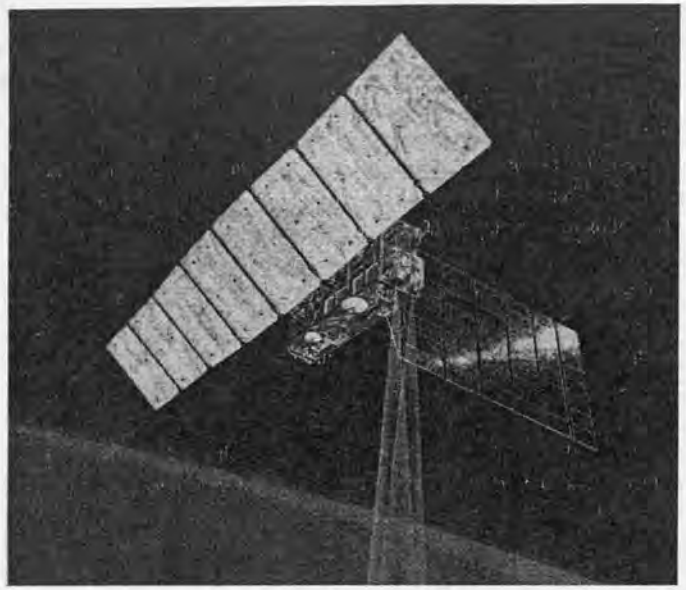

Fig. 2-4. Artists concept of the JERS-1 SAR.

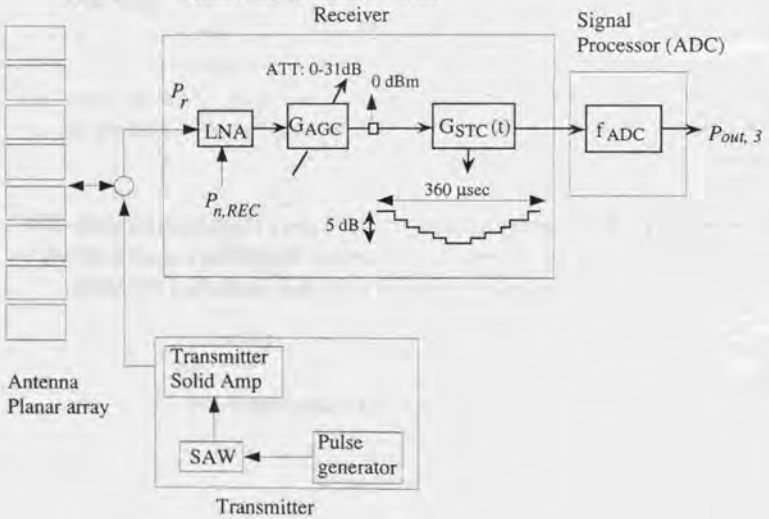

Fig. 2-5. Simplified block diagram of the Japanese Earth Resources Satellite - 1 Synthetic Aperture Radar (JERS-1 SAR).

Table 2-2. Representative spaceborne SARs

	JSAR	SEASAT	SIR-C	ERS-1/2	Radarsat	X-SAR
Off-nadir angle (deg)	35.2	20	20 - 55	20	20-49	
Swath (Km)	75	100	15-90	100	100	15-60
Resolution (m)	18(3)	20(4)	30*30	28*25 (4)		
Antenna gain (dB)	33.5	33	36.4(L) 42.7(C)		44.5	
Azimuth beam width (deg)	0.98		1.0(L) 0.25(C)			0.14
Elevation beam width (deg)	5.4	5	5 to 16(L) 5 to 16(C)			5.5
Antenna size (m)	11.92 *2.2	10.5*2.0	12.*2.9(L) 12*0.7(C)		15.0*1.5	12.*0.4
Wavelength (m)	0.235	0.235	0.235(L) 0.058(C)	0.056	0.056	0.031
Pol.	HH	HH	HH, HV, VH, VV	VV	HH	VV
Pulsewidth(µs)	35	33.8	33.17, 8.5		42.0	40
Peak power (W)	325	1000	4400(L) 1200(C)	4800	5000	1400
ADC bit number	3 I-Q	Analog	8/4	5 I-Q	4 I-Q	4, 6, IQ

For Radarsat: Standard beam's specification is given.

2.5 SAR Processing Algorithms

The Range Doppler method approximates two-dimensional correlation by two one-dimensional correlations: range correlation and azimuth correlation. A frequency domain correlation significantly shortens the throughput time compared with time domain correlation. However, the range migration curve crossing over several ranges makes the processing difficult. Furthermore, the range migration amount, Doppler frequency chirp rate, and Doppler centroid, depend on the slant range. The original Range Doppler method did not correct local dependency of these parameters, resulting in some un-focusing in the near range and the far range when a wider range image was processed. This range migration problem was partially solved by Jin [4] and Tsuboi [5]. Smith proposed another Range Doppler method [10]; its advantage is the simple algorithm, and its disadvantage is the difficulty in perfect focusing for the large range curvature.

The range migration problem was also solved by introducing the seismic radar imaging technology for underground imaging; the omega-kappa (ω-κ) developed by Caffirio et. al. [11], [12] has gained that the data focusing can be attained even for large range migration

[13], [14]. A true two-dimensional processing method was proposed by two Italian researchers individually. One is by Franceschetti [15] and employs many small computers to image the ERS-1 raw data. The other is by Lanari [16]. A Chirp Scaling method, proposed by Raney and Bamler [17], equalizes the dependence of the processing parameters on the slant range over a swath. This is not two-dimensional correlation, but is more like the ω–κ. The FFT of raw data is taken in range first. The azimuth correlation is conducted next using the reference function normalized by a chirp scaling. Finally, an inverse FFT of the above data multiplied by the range reference function is conducted. The advantage is that the interpolation of the range migration is eliminated.

2.6 Calibration Instruments and Sources

Corner reflectors (CRs), active radar calibrators (ARCs), and ground-based receivers are the representative instruments for absolute SAR calibration. As rainforest images are composed of the distributed targets, they become good sources for SAR characterization (SNR, AGC, STC, saturation, I-Q gain imbalance, etc.). Flat rainforest images for Amazon, Guyana, and Sumatra, are known to be the best.

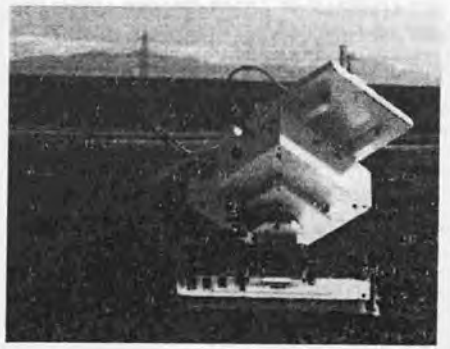

a) Active radar calibrator used for L-band SAR on JERS-1

b) 2.4 m trihedral corner reflector

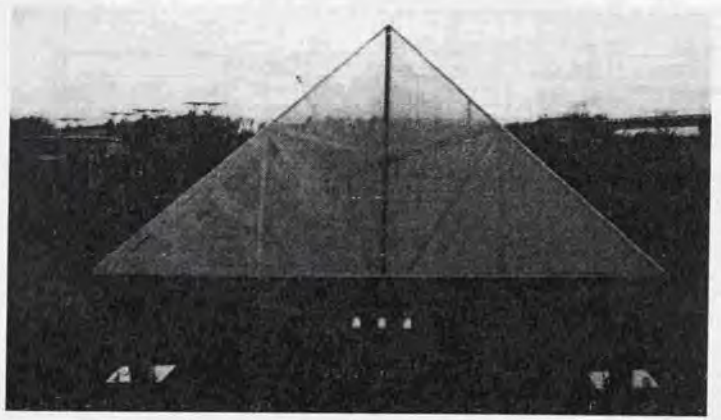

Fig. 2-6. Typical calibration instruments, ARC (top) and Trihedral Corner reflector (bottom)

2.6.1 Corner Reflectors

The corner reflectors can be circular, planar, dihedral, trihedral, or other shapes [18], [19], [20], as summarized in Table 2-3. Trihedral corner reflector is useful for calibrating like-polarization because of its larger radar cross section, wider 3 dB down beamwidth which allows slightly relaxed alignment, and relatively stronger structure (Fig. 2-6). Dihedral corner reflector is used for cross-polarization. A pentagonal corner reflector has been proposed to improve the reflected wave which may be degraded by the possible multipath between the ground and the leaves of the corner reflector [21]. The advantages of CRs are that they are easy to assemble and cheap to manufacture, and that they have relatively good accuracy when each leaf surface is reinforced and well conditioned [22], [23]. The disadvantages of CRs are the uncertainty due to undulation of the leaf (by the wind [24]) and relatively small radar cross section, especially for spaceborne SARs.

Table 2-3. Summary of the corner reflectors

No.	Type of target	Peak RCS	Half power beam width	Comments
1	Rectangular plate	$4\pi A^2/\lambda^2$	$0.44\lambda/a$	Large σ_{max}, very narrow beamwidth
2	Circular plate	$4\pi A^2/\lambda^2$	$0.44\lambda/b$	Large σ_{max}, very narrow beamwidth
4	Trihedral corner reflector	$\frac{4\pi a^4}{3\lambda^2}$	30 - 40 degrees	σ_{max}, about 3dB lower than that of a flat plate with same aperture
5	Dihedral corner reflector	$\frac{16\pi a^2 b^2}{\lambda^2}$	~ 40 degrees in elevation $\lambda/2b$ in azimuth	Narrow beamwidth in azimuth

Note: Refer to Ulaby [18] and Sarabandi [21], A is the area, λ the wavelength, a the length of leaf.

2.6.2 Frequency Tunable Active Radar Calibrators (ARC)

The ARC consists of an antenna, a receiver and a transmitter. Here we describe one developed for JERS-1 SAR. We show the ARC deployed in the filed in Fig. 2-6 a), and block diagram in Fig. 2-7, and the characteristics in Table 2-4. The antenna consists of two planar (square patch) elements; its azimuth and elevation beam widths are 30 degrees (3 dB down), so there is a wide allowance for the antenna setting angle [71], [20]. In order to prevent cross coupling, the receive and transmit antennas are separated by 50 cm and their polarizations are aligned perpendicularly. The receiver/transmitter amplifies the incoming signal by a low-noise amplifier, frequency-shifts it in the phase controller/shifter, re-amplifies it to the appropriate level, and transmits it to the satellite. The frequency-shifted signal (power) can be monitored by a spectrum analyzer through the directional coupler. Gain can be measured by using a signal generator and spectrum analyzer. A step-wise selective attenuator can set the σ from 15 to 60 dBm^2 in 5 dBm^2 step and frequency shifts of 0, 20, 40, 80, 180 Hz. While the SAR pulse is being detected, the phase controller mixes the signal (S_{ARC}) whose phase changes linearly with time.

Table 2-4. Characteristics of the representative ARCs (for JERS-1 SAR)

Satellite	JERS-1 SAR	Remarks
Radar cross section	15 - 60	In 5 dBm^2 steps
Frequency Shift	20, 40, 80, 180	Hz
Antenna beam width	(30, 32.4) deg	Azimuth and elevation
Frequency	L band	
Receiver monitor	Yes	Spectrum analyzer
Stability (2 hr)	$\pm$0.5 dB	
Battery	2 hr'	External operation
No. of units	2	

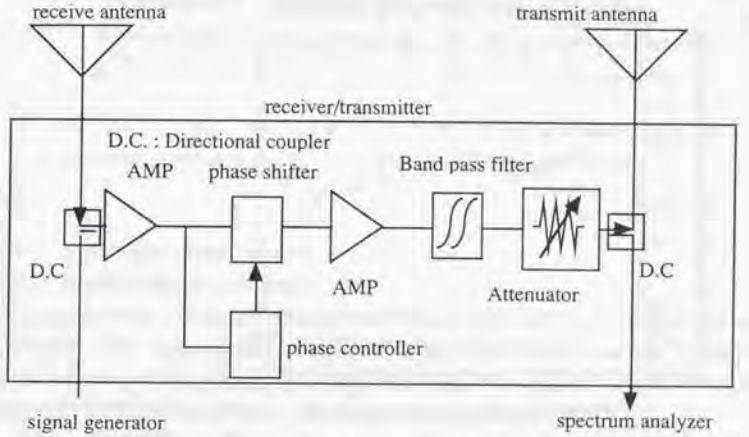

Fig. 2-7. Block diagram of the ARC for JERS-1 SAR.

2.6.3 Ground Based Receiver

A ground-based receiver measures the signal intensity transmitted from the SAR. Data analysis based on the radar equation estimates the SAR transmission power. It also provides the SAR antenna pattern as a function of the azimuth and elevation angles. A set of receivers deployed over the imaging swath measure the three-dimensional SAR antenna pattern [25], [26]. DLR and Univ. of Stuttgart jointly conducted the JERS-1 SAR antenna pattern measurement and pointed out its asymmetry [33], which may be due to the fact that SAR antenna was bended for fifty days until the final deployment was confirmed [33].

2.6.4 Rainforest Data

Because of the volume scattering mechanism, rain forest data is very useful for the calibration. The homogeneity of the scatterers shows the constancy of the NRCS for wide

range of incidence angles (see Fig. 2-8 obtained by AIRSAR of JPL/NASA over Belize rainforest), and shows the strong agreement with the mathematical expression for the intensity distribution (see Fig.2-9; the detailed explanation is given in (2.12)). However, the independence of the adjacent pixel is not perfect in actual images, so sub-sampling of the data is necessary for measuring the average and standard deviation (Azimuth and range auto-correlations for two different images are shown in Fig. 2-10. Distance of independence which shows 1/e of correlation is more than 1 pixel).

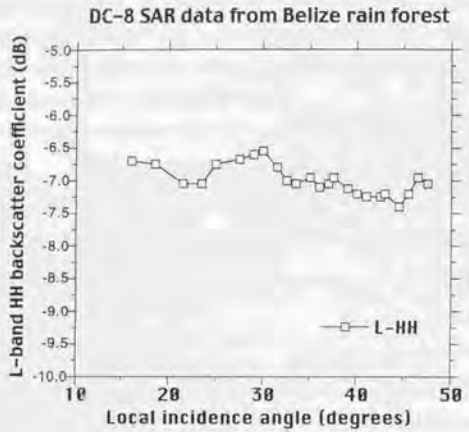

Fig. 2-8. Measured backscattering coefficients dependency on incidence angle in AIRSAR data over Belize (after [47]).

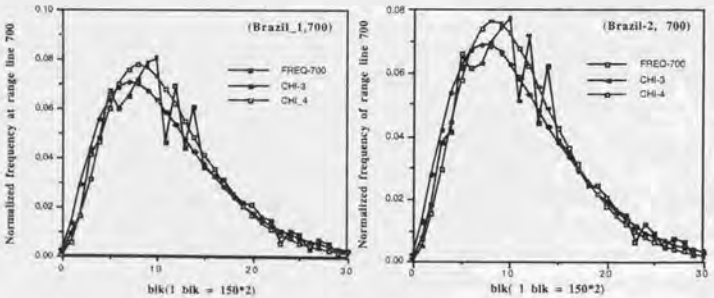

Fig. 2-9. The SIR-B image distribution for Brazil rainforest scenes. The measured distribution exists between the 3-look and 4-look distribution function. A "blk" is the size of the bin.

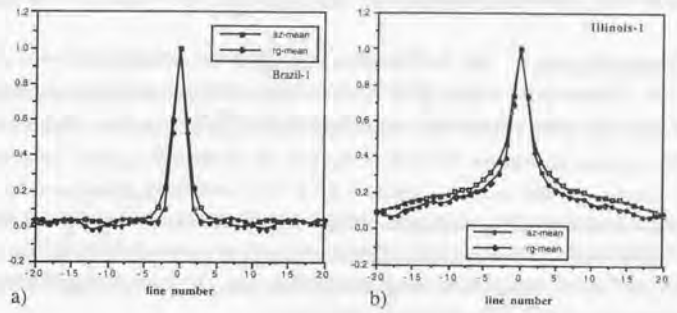

Fig. 2-10. Autocorrelation coefficients of SIR-B image for Brazil(a) and Illinois farmland(b), where the increment of the horizontal axis is the range line number.

2.7 SAR Image Characteristics

2.7.1 Received Signal and Noise

The output of the receiver of SAR consists of signals scattered from the targets and noise in the SAR. The former can be correlated. The latter (noise) can not be correlated. Additionally, speckle generates multiplicatively as a coherent system noise. Those signals and noise are summarized below.

Signals

i) Point target is an ideal type of scatterer and is isolated from (not interfered by) any adjacent scatterer. A point target does not generate speckle noise. A bright target with a coherent signal reflector, deployed within a SAR resolution cell with a relatively higher signal-to-background ratio, can be recognized as a point target.

ii) Distributed target contains a huge number of scatterers within a resolution cell. Therefore, the reflected signal suffers from the fading effect, and its intensity and phase change depend on the observation angle [36]. The correlation gain for each of scatterer is the same as that of the point target. The signal from the distributed target (real and imaginary parts of the reflection coefficient) behaves like a 2-D Gaussian in space but is repeatable in time at a fixed coordinate [37], [38].

Noise

i) Thermal noise is generated by the SAR receiver. The low noise amplifier at the front end of the receiver generates random noise dependent on the temperature and the noise figure.

The signal-to-noise ratio (SNR) of the raw data is primarily determined by the low noise amplifier (LNA). This noise is Gaussian.

ii) Saturation noise The SAR receiver is designed and manufactured to be as linear as possible. However, the limited SAR dynamic range often generates signal distortion in receiver, A/D converter, or protection amplifier before the A/D converter. This noise is not Gaussian.

iii) ADC bit redundancy noise is the uncertainty which arises during digitization. The distribution of the noise depends on that of the incoming signal [40]. If the incoming signal is uniformly distributed, redundancy noise becomes Gaussian. If the input signal is Gaussian, the output may be slightly different from Gaussian [39].

iv) Speckle is generated by the fading of the scattered signal from the distributed target. It is often modeled as a multiplicative noise:

$$P(u)=\frac{1}{\bar{u}}e^{-\frac{u}{\bar{u}}} \tag{2.11}$$

where P(u) is the speckle distribution function of intensity u, and $\bar{u}$ is the mean intensity. The feature of speckle is that the brighter the target is, the greater the speckle noise is. Reduction of the speckle noise is a major theme in image recognition. From the calibration point of view, the speckle is unwelcomed disturbance. A point target is not affected by the speckle and can thus be used as the signal source.

2.7.2 SAR Image Distribution Function

Incoherent summation of the single-look image power reduces the speckle noise. The distribution function of N (N>= 1) look images is expressed by

$$P(z_N)=\frac{N^N\cdot z_N^{(N-1)}}{(N-1)!\cdot\overline{z_N}^N}e^{-N\frac{z_N}{\overline{z_N}}}, \tag{2.12}$$

where $\overline{z_N}$ is the mean of the N look image and is equal to N times the mean of single look, i.e. $\overline{z_N}=N\cdot\overline{z_1}$. The ratio (RA) of the variance to the square of the mean is simply a function of the number of looks (N):

$$RA=\frac{\overline{x^2}}{\overline{x}^2}=\frac{N+1}{N} \tag{2.13}$$

This parameter estimates the effective number of looks for an image.

2.8 Calibration Status

Since the beginning of the 1980s, SAR calibration has been performed at several institutes. The calibration accuracy depends on the stability of the SAR instruments (antenna elevation pattern and gain change properties), that of the calibration devices, and the signal-to-clutter ratio of the calibration sites, not on the calibration algorithm. We summarize the current status of the calibration accuracy reported by the representative agency in Table 2-5. From this, current status of the calibration accuracy varies from 1 dB to 3 dB.

2.9 Conclusions

This chapter has summarized the current SAR calibration status as a preparation for the presentations given in Chap. 3 - Chap. 7.

Table 2-5. Calibration accuracy

Agency	Sensor	Freq.	Accuracy	Year	Method	Cal-device	Ref.
JPL	AIRSAR	P-HH	+-6.7 dB	1988	PM	CR	[35]
		P-VV	+-4.0	1988	PM	CR	[35]
		L-HH	+-2.4	1988	PM	CR	[35]
		L-VV	+-2.4	1988	PM	CR	[35]
		C-HH	+-7.6	1988	PM	CR	[35]
		C-VV	+-9.3	1988	PM	CR	[35]
CCRS	CCRS SAR	C-HH	+-0.8 dB	1991	IM	ARC	[27]
DLR	E-SAR		+-1.1 dB	1991	IM	ARC/CR	[28]
	DC-8		+-0.4 dB	1991	IM	ARC/CR	[28]
CCRS	CCRS-SAR		1.4 dB	1990	IM	ARC	[29]
JPL	SIR-C	L	+-2.3 dB	1995	IM	ARC/CR	[30]SRL-1
		L	+-2.0 dB	1995	IM	ARC/CR	[30]SRL-2
		C	+-2.2 dB	1995	IM	ARC/CR	[30]SRL-1
		C	+-3.2 dB	1995	IM	ARC/CR	[30]SRL-2
DLR	X-SAR	X	+-1dB	1995	IM	CR	[31]SRL-1/2
NASDA	JERS-1 SAR	L	+-0.99 dB	1993	IM	ARC/CR	[32]
DLR	JERS-1 SAR	L	+-2 dB(3σ)	1995	IM	CR	[33]
JPL	JERS-1 SAR	L	+-0.55 dB	1995	IM	CR	[34]
DRA	ERS-1 AMI	C	+-0.25	1993	IM	CR/ARC	[22]

PM Peak Method
IM Integral Method

References

[1] C. Wu, "A digital approach to produce imagery from SAR data," presented at the AIAA Syst. Design Driven by Sensors Conf., aper, no. 76-968, Pasadena, Ca, OCT. 18-20, 1976.

[2] M. R. Vant, G. E. Haslarn, and G. M. Royer, "A digital signal processing approach for satellite-borne synthetic aperture radar (SAR)," presented at the 2nd int. Conf. Radar, Paris, France, Dec., 1978, commun, VIII.

[3] W. J. Van de Lindt, "Digital technique for generating synthetic aperture radar images," IBM J. Res. Develop., vol. 21, no. 5, pp. 415-432, Sept. 1977.

[4] M. Y. Jin and C. Wu, "A SAR Correlation Algorithm which Accommodates Large-Range Migration," IEEE Trans. Geosci. Rem. Sens., vol. GE-22, no. 6, pp. 592-597, Nov. 1984.

[5] A Tsuboi, K Honma, and F Komura. "A SAR Image Restoration Using Time Variant Inverse Filter," Measurement Automatic Control Society, vol. 23, no. 11, pp. 1139-1144, Nov. 1987. In Japanese.

[6] A. Freeman, J. C. Curlander, "Radiometric Correction and Calibration of SAR images," Photogrammetric Engineering and Remote Sensing Journal, vol. 55, no. 9, pp. 1295-1301, Sept. 1989.

[7] Y. Nemoto, H. Nishino, M. Ono, H. Mizutamari, K. Nishikawa, and K. Tanaka, "Japanese Earth Resources Satellite-1 Synthetic Aperture Radar," Proc. of the IEEE. vol. 79, no. 6, pp. 800-809, June 1991.

[10] A. M. Smith, "A new approach to range-Doppler SAR processing," Int. J. Remote Sensing, vol. 12, pp. 235- 251, 1990.

[11] C. Caffirio, C. Prati, and F. Rocca, "SAR Data Focusing Using Seismic Migration Techniques," IEEE TAES, vol. 27, no. 2, pp. 194-207, March 1991.

[12] C. Caffirio, C. Prati, and F. Rocca, "Full resolution focusing of SEASAT SAR images in the frequency wave number domain," INT., J of remote sensing, vol. 12, no. 3, pp. 491-510, 1991.

[13] R. Bamler, "A Comparison of Range-Doppler and Wavenumber Domain SAR Focusing Algorithms," IEEE Trans. Geosci. Remote Sensing. vol. 30, no. 4, pp. 706-713, July 1992.

[14] A. S. Milman, "SAR imaging by w-k migration," Int. J. Remote Sensing, vol. 14, no. 10, pp. 1965-1979, 1993.

[15] G. Franceschetti, and G. Schirinzi, "A SAR processor based on two dimensional FFT codes," IEEE Trans. Aerosp. Electron. Syst., AES-26, pp. 356-366, 1990.

[16] R. Lanari and H. Hirosawa, "Synthetic Aperture Radar Data Processing Using Nonstandard FFT Algorithm: JERS-1, a Case Study," IEICE Trans Commun, vol. E76-B, no. 10, pp. 1271-1278, 1993.

[17] R. K. Raney, H. Runge, R. Bamler, I. G. Cunning, and F H. Wong, "Precision SAR Processing Using Chirp Scaling," IEEE Trans. Geosci. Remote Sensing., vol. 32, no. 4, pp. 786-799, July 1994.

[18] F. Ulaby, R.Moore, A. Fung, "Microwave Remote Sensing, Active and Passive," Vol. 2, "Radar remote sensing and surface scattering and emission theory," Chap 10, pp. 767-779, Addison-Wesley Publishing Company.

[19] A. Freeman, J. C. Curlander, P. D. Dubois, and J. Klein, "SIR-C Calibration Workshop Report," JPL Center for Radar Studies Publication, no. 88-003, Nov. 1988.

[20] A. Freeman, "SIR-C Calibration: An Overview," JPL D-6997, Feb. 1990.

[21] K. Sarabandi, and T-C Chiu, "An optimum corner reflector for calibration of imaging radars," Proceedings of the CEOS SAR calibration workshop, 28-30, Sept. 1994, The University of Michigan, pp. 52-79.

[22] P. J. Bird, G. E. Keyte, and D. R. D. Kenward, "Calibration of ERS-1 SAR," Proceedings of the CEOS SAR calibration workshop, 20- 24 Sept. 1993, ESTEC, Noordwijk, ESA WPP-048, pp. 257-281.

[23] D. R. D. Kenward, "A precision Corner Reflector for ERS-1 SAR Calibration," DRA working paper SP(92) WP90, Dec. 1992.

[24] P. J. Bird, et. al., "An Experiment for the Radiometric Calibration of the ERS-1 SAR," in Proc. of the first ERS-1 symposium, Nov. 1992.

[25] P. Seifert, H. Lentz, M. Zink, and F. Heel, "Ground-based Measurement of Inflight Antenna Patterns for Imaging Radar System," IEEE Trans. Geosci. Remote Sensing., vol. 30, no. 6, pp. 1131-1136, Nov. 1992.

[26] P. Seifert, H. Lentz, and M. Zink, "ERS-1 Preliminary Antenna Elevation Pattern Measured by Ground Receivers," Proceedings of the first ERS-1 symposium, ESA SP-359, pp. 157-159, March 1993.

[27] M. H. Ulander, R. K. Hawkins, C. E. Livingstone, and T. I. Lukowski, "Absolute Radiometric Calibration of the CCRS SAR," IEEE Trans. Geosci. Remote Sensing, vol. 29, no. 6, pp. 922-933, Nov. 1991.

[28] M. Zink, F. Heel, and H. Kietzmann, "The Oberpfaffenhofen SAR Calibration Experiment of 1989," Journal of Electromagnetic Waves and Applications, vol. 5, no. 9, pp. 935-951, 1991.

[29] A. L. Gray, P. W. Vachon, C. E. Livingstone, and T. I. Lukowski, "Synthetic Aperture Radar Calibration Using Reference Reflectors," IEEE Trans. Geosci. Remote Sensing, vol. 28, no. 3, pp. 374-383, May 1990.

[30] A. Freeman, M. Alves, B. Chapman, J. Cruz, Y. Kim, S. Shaffer, J. Sun, E. Turner, and K. Sarabandi, "SIR-C Data Quality and Calibration Results," IEEE Trans. Geosci. Remote Sensing, vol. 33, no. 4, pp. 848 - 857, July 1995.

[31] M. Zink and R. Bamler, "X-SAR Radiometric Calibration and Data Quality," IEEE Trans. Geosci. Remote Sensing, vol. 33, no. 4, pp. 840-847, July 1995.

[32] M. Shimada and M. Nakai "Inflight Evaluation of L band SAR of Japanese Earth Resources Satellite-1," Adv. Space Res. vol. 14, no. 3, pp. 231-240, 1994.

[33] M. Zink, "JERS-1 External Calibration Experiments," Final Report of JERS-1/ERS-1 System Verification Program, vol I, pp. 1-94 - 1-101, March 1995.

[34] B. Chapman, M. Alves, and A. Freeman, "Validation and Calibration of J-ERS-1 SAR Imagery," Final Report of JERS-1/ERS-1 System Verification Program, vol I, pp. 1-75 - 93, March 1995.

[35] A. Freeman, "Calibration and Image Quality assessment of the NASA/JPL aircraft SAR during spring 1988," JPL D-7197, Feb. 1990.

[36] C. Elachi, "Spaceborne Remote Sensing: Application and Techniques," IEEE press, 1988.

[37] R. K. Raney, "SAR Response to Partially Coherent Phenomena," IEEE Transactions on Antennas and Propagation, vol. AP-28, no. 6, pp. 777-787, Nov. 1980.

[38] A. Freeman, and J. C. Curlander, "Radiometric Correction and Calibration of SAR Images," JPL internal memo, 1990.

[39] D. M. Grieco, "Quantization and Saturation Noise Due to Analog-to-Digital Conversion," IEEE transactions of Aerospace and Electronic Systems, pp 222-223, Jan. 1971.

[40] GEC-Marconi, "SAR data quality assessment and rectification final report," ESA contract, no. 6635/86/HGE-I, March 1988.

[41] P. J. Meadows, and P. A. Write, "ERS-1 synthetic aperture radar analogue to digital converter saturation," Proceedings of the CEOS SAR calibration workshop, 28- 30, Sept. 1994, The Univ. of Michigan, pp. 24-37.

[42] P.S. Cooper, "ADC saturation effects and point target calibration," Proceedings of the CEOS SAR calibration workshop, 28- 30, Sept. 1994, The Univ. of Michigan, pp. 38-51.

[43] M. Shimada, "Radiometric correction of the saturated SAR image," Proceedings of the CEOS SAR calibration workshop, 28- 30, Sept. 1994, The Univ. of Michigan, pp. 123-142.

[44] P. Seifert, H. Lentz, M. Zink, and F. Heel, "Ground-Based Measurements of Inflight Antenna Patterns for Imaging Radar Systems," IEEE Trans. Geosci. Remote Sensing, vol. 30, no. 6, pp. 1131-1136, 1992.

[45] R. K. Moore and M. Hemmat, "Determination of the vertical pattern of the SIR-B antenna," Int. J. Remote Sensing, vol.9, no.5, pp. 839-847, 1988.

[46] R. K. Moore, V. S. Westmoreland, D. Frank, and M. Hemmat, "Determining the vertical antenna pattern of a spaceborne SAR by observation of uniform targets," Proc. IGARSS '86 Symp., Zurich, Switzerland, vol. 1, pp. 469-472.

[47] M. Shimada, and A. Freeman, "A technique for Measurement of Spaceborne SAR Antenna Patterns Using Distributed Targets," IEEE Trans. Geosci. Remote Sensing, vol. 33, no. 1, pp. 100-114, Jan. 1995.

[48] R. K. Hawkins, "Determination of antenna elevation pattern for airborne SAR using the rough target approach," IEEE Trans. Geosci. Remote Sensing, vol. 28, no. 5, pp. 896- 905, Sept. 1990.

[49] M. C. Dobson, F. T. Ulaby, D. R. Brunfeldt, and D. N. Held, "External calibration of SIR-B imagery with area extended and point targets," IEEE Trans. Geosci. Remote Sensing, vol. 24, no.4, pp. 453-461, 1986.

[50] D. R. Brunfeldt and F. T. Ulaby, "Active Reflector for Radar Calibration," IEEE Trans. Geosci. Remote Sensing, vol. GE-22, no. 2, pp. 165-169, March 1984.

[51] M. Shimada, H. Oaku, and M. Nakai, "Calibration Using Frequency-Tunable Active Radar Calibrators," IEEE Trans. Geosci Remote Sensing, 1997, in press.

[52] M. Fujita, "An Active Reflector for SAR Calibration Having a Frequency Shift Capability," IEICE TRANS. COMMUN., vol. E75-B, no. 8, pp. 791-793, Aug. 1992.

[53] M. Shimada, M. Nakai, and S. Kawase, "Inflight Evaluation of L band SAR of JERS-1," Canadian Journal of Remote Sensing, vol 19, no. 3, ISSN 0703-8992, pp. 247-258, Aug. 1993.

[54] M. Shimada, M. Nakai, "First result of the SAR characterization (in Japanese)," Technical Report of IECE SANE92-58, Nov. 1992.

[55] H. Laur, P. Meadows, J. I. Sanchez, E. Dwyer, "ERS-1 SAR radiometric Calibration," 20-24 Sept. 1993, ESTEC, Noordwijk, the Netherlands. CEOS calibration/validation working group SAR calibration sub-group, pp. 257-281

[56] M. Shimada, "An estimation of JERS-1's SAR antenna pattern using Amazon rain forest images," Proc. 1993 SAR Calibration Workshop, Noordwijk, The Netherlands, Sept. 1993, pp. 185-208.

[57] J. J. V. Zyl, B. D. Chapman, P. Dubois, and J. Shi, "The Effect of Topography on SAR Calibration," IEEE Trans. Geosci. Remote Sensing, vol. 31, no. 5, pp. 1036-1043, Sept. 1993.

[58] L. M. H. Ulander, "Radiometric Slope Correction of Synthetic Aperture Radar Images," IEEE Trans. Geosci. Remote Sensing, vol. 34, no. 5, pp. 1115-1122, Sept. 1996.

[59] M. Satake, et. al., "Calibration experiment of ESA ERS-1 SAR using the active microwave reflector (Japanese)," in Proc. of the 15th symposium of Japan Remote sensing society, Dec. 1993, pp. 29-30.

[60] M. Nakai, M. Shimada, and H. Wakabayashi, "Calibration of the synthetic aperture radar installed on JERS-1 - part 2 - (Japanese)," in Proc. of 17th Japan remote sensing symposium, Oct. 2, 1991, pp. 21-22.

[61] Y. L. Desnos, J-L. Valero, and M. Loiselet, "J-ERS-1 and ERS-1 SAR calibration Experiments over Flevoland," in Proc. of IGARSS'93, pp. 955-957.

[62] M. Shimada, "Calibration of the JERS-1 SAR image and the image quality (Japanese)," Journal of Japan remote sensing society, vol. 14, no. 2, pp. 35-47, 1994.

[63] A. Freeman, et al, "Spaceborne Imaging Radar-C, SIR-C ground calibration plan," JPL D-6999, February 1990.

[64] N. Kodaira, "Possibility of the use of a Transponder as an active SAR calibration target," IGARSS'89, Vancouver, CANADA, July 10-14, pp. 258-260.

[65] T. I. Lukowski, R. K. Hawkins, P.S. Daleman, and L. M. H Ulander, "CCRS Synthetic Aperture Radar Data Calibration - Status Report," in proceedings of IGARSS '90, Remote sensing: pp. 791-794, College park, Maryland.

[66] P.S. Daleman, R. K. Hawkins, and T. I. Lukowski, "Experience with Active Radar Calibrators for Airborne SAR," in proceedings of IGARSS '90, Remote sensing: College park, Maryland, pp. 795-798.

[67] T. I. Lukowski, R. K. Hawkins, B. Brisco, R. Brown, R. Ford, and P.S. Daleman, "The Saskatoon SAR Calibration Experiment," in proceedings of IGARSS'89, Remote sensing: Vancouver, Canada, pp. 254-257.

[68] D. R. Brunfeldt, "SAR Response to modulated target," in proceedings of IGARSS'89, Remote sensing: , College park, Maryland, pp. 2901-2905.

[69] S. Dill, D. Hounam, and K. H Wagel, "Generation of Invisible SAR targets using coded transponder," SAR calibration workshop of CEOS CAL/VAL working group, 20- 24 Sept. 1993, ESTEC, pp. 65-76.

[70] L. M. H. Ulander, "Accuracy of Using Point Targets for SAR Calibration," IEEE Trans. on Aerospace and Electronic Systems, vol. 27, no. 1, pp. 139-148, Jan. 1991.

[71] NASDA contract report CDA-3-727, "Development of the active radar calibrator for JERS-1/ERS-1 SAR," Mitsubishi Electric Corporation, 1989.

[72] M. Shimada, "Radiometric Correction of Saturated SAR Data," IEEE Trans. Geosci Remote Sensing, 1998, in Press.

[73] ERSDAC, "Synthetic Aperture Radar: Chapter 2,1992.

CHAPTER 3 RADAR EQUATION FOR SAR CORRELATION POWER

3.1 Introduction

SAR imaging is a linear process as long as the signal is within the dynamic range of the SAR instrument and the ground processor. When the received signal exceeds the dynamic range of SAR's Analog-to-Digital Converter (ADC), the saturated signal component reduces the correlation power with slightly different gains for the correlative targets and the noise. This chapter investigates a process which reduces the correlation power due to saturation. A radar equation of the correlated signal power which considers saturation noise, A/D conversion noise, and thermal noise is derived. A radiometric correction method (power recoverage), that amplifies the range correlation output or raw data by a gain depending on the local saturation rate, is proposed.

3.2 Theory

3.2.1 Assumptions

From data reception and digitization points of view, a SAR is composed of three units: the low-noise amplifier (LNA), the intermediate amplifier with receiver gain adjuster, and the ADCs (Fig. 3-1). The LNA amplifies the incoming signals received by the antenna to an intermediate power level and generates the thermal noise additionally. The intermediate amplifier adjusts the output of the LNA to the final level, in which the gain can be selected manually; by Manual Gain Control (MGC), or automatically; by Automatic Gain Control (AGC). The noise generated in the intermediate amplifier is negligibly smaller than the thermal noise. Redundancy noise and saturation noise may occur in the AD conversion process as the difference between the input and digitized code. Although redundancy noise occurs only when the input is within the AD conversion range, saturation noise occurs when the input exceeds the AD conversion range. Thus, redundancy noise and saturation noise do not exist simultaneously.

Within the SAR observation scheme, a series of pulses is transmitted to the target as the SAR moves. These signals are then scattered by the target and received by the SAR. In each process from pulse transmission to reception, there are three modulations: a gradual phase change which is due to the relative movement of SAR and the scatterer; an amplitude change which depends on the scatterer's reflectivity; and a quick phase change which depends on the scatterer's complex reflectivity. Because each modulation is a linear process, summation of the processes over all the scatterers in the illuminated area expresses the signal to be received by the SAR. The scatterers are distributed randomly in space, not in time, so the scattered signals can

be approximated by a random process. Note that the received signal is a stationary independent Gaussian process in space, and the thermal noise is a stationary Gaussian process in time.

We assume the following for the ADC and the receiver:

(i) The ADC has a quantization interval, h, and a saturation level, C, of $h*2^{(L-1)}$, where L is the number of bits;
(ii) The ADC causes redundancy noise and saturation noise; the former is Gaussian with zero mean and the latter is not Gaussian as discussed later;
(iii) A receiver is a linear instrument, and does not cause any nonlinear noise;
(iv) The LNA generates Gaussian thermal noise.

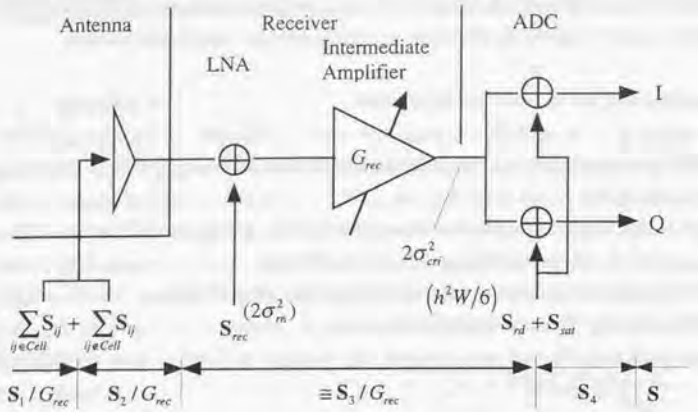

Fig. 3-1. Simplified block diagram of SAR. Gaussian noise is generated in the LNA and ADC: saturation noise (S_4) is generated in the ADC.

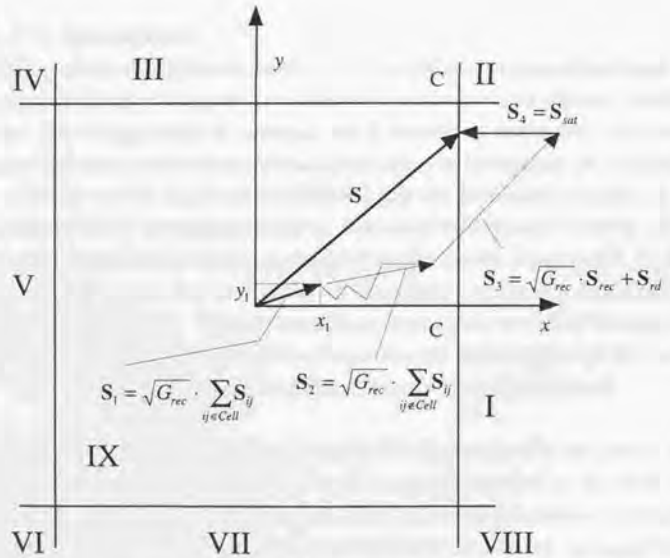

Fig. 3-2. Coordinate system of A/D conversion. S_1, S_2, S_3 and S_4 are the amplified signal from the resolution cell, the amplified signal outside resolution cell, the amplified thermal and ADC redundancy noise, and ADC saturation noise. C is the maximum input voltage. ADC saturation noise differs in each region (I to IX).

3.2.2 SAR raw data expression

A instantaneous SAR raw data at the output of ADC can be expressed by (see Fig 3-2)

$$\mathbf{S} = \sqrt{G_{rec}(t_r,t_a)} \cdot \sum_{ij\in Cell} \mathbf{S}_{ij} + \sqrt{G_{rec}(t_r,t_a)} \cdot \sum_{ij\notin Cell} \mathbf{S}_{ij} + \sqrt{G_{rec}(t_r,t_a)} \cdot \mathbf{S}_{rec} + \mathbf{S}_{rd} + \mathbf{S}_{sat}, \qquad (3.1)$$

where

$$\mathbf{S}_{ij} = a_{ij} e^{j\delta_{ij}} e^{2\pi j\left(\frac{k_r}{2}t_r^2 + \frac{k_a}{2}t_a^2\right)} \qquad (3.2)$$

is the received signal from the ij[th] scatterer within an IFOV; $G_{rec}(t_r, t_a)$ is the receiver gain at an azimuth time, t_a, when pulse is transmitted and at a range time, t_r, when the pulse is received;; S_{rec} is the thermal noise of the receiver; S_{rd} is the redundancy noise of ADC; S_{sat} is the saturation noise; k_r and k_a are the range and azimuth chirp rate; a_{ij} is the amplitude of the received signal from the ij[th] scatterer; δ_{ij} is the phase for the ij[th] scatterer. δ_{ij} contains information on the distance from the satellite and the scatterer's physical characteristics (Fig. 3-3). The first term on the right side of (3.1) sums up all the correlative scatterers in a resolution cell (Cell). If we focus on the scatterers in a Cell, the remaining four terms should be non-correlative components or noise. The second, third, and fourth terms are two-dimensional Gaussian signals, whose variances are the amplified signal power, amplified thermal noise power, and ADC redundancy noise power. The fifth term represents nonlinear noise with an unknown distribution function.

Eq. (3.1) is rewritten under the above assumptions by

$$\mathbf{S} = \sum_{i=1}^{4} \mathbf{S}_i, \qquad (3.3)$$

where

$\mathbf{S}_1$ Amplified correlative signal from the scatterers within a Cell. $\mathbf{S}_1$'s x-y component is (x_1, y_1). Its power, P_1, is given by using the signal-to-clutter ratio (SCR) and the averaged background power, a_d^2, from each resolution cell as:

$$\mathbf{S}_1 \equiv \sqrt{G_{rec}(t_r,t_a)} \sum_{ij\in Cell} \mathbf{S}_{ij} \qquad (3.4)$$

$$P_1 = a_d^2 \cdot SCR \cdot G_{rec} \qquad (3.5)$$

$$SCR \equiv \frac{\sum_{ij\in Cell} a_{ij}^2}{a_d^2} \qquad (3.6)$$

S_2 Amplified non-correlative signal from an IFOV, excluding S_1. Its power, $2\sigma_n^2$, is given by using M and N, which are the sizes of the instantaneous field of view divided by the pixel spacing in azimuth and range directions:

$$S_2 \equiv \sqrt{G_{rec}(t_r, t_a)} \sum_{ij \in Cell} S_{ij} \tag{3.7}$$

$$2\sigma_n^2 = a_d^2 \cdot (MN-1) \cdot G_{rec} \tag{3.8}$$

S_3 Summation of the amplified thermal noise and ADC redundancy noise. Its Gaussian component is (x_3, y_3) and its power is $2\sigma_{rn}^2$.

$$S_3 = \sqrt{G_{rec}(t_r, t_a)} \cdot S_{rec} + S_{rd} \tag{3.9}$$

$$2\sigma_{rn}^2 \equiv 2\sigma_{rn0}^2 \cdot G_{rec}(t_r, t_a) + \frac{h^2}{6} W \tag{3.10}$$

where $2\sigma_{rn0}^2$ is the thermal noise power. The second term on the right side of (3.10) is the ADC redundancy noise power, which depends on the power input to the ADC (see Appendix 3-1). W is a weighting factor. Combining (3.5), (3.8), and (3.10), the SNR of the raw data can be expressed by

$$SNR = \frac{(MN-1+SCR) \cdot a_d^2 \cdot G_{rec}}{2\sigma_{rn}^2 \cdot G_{rec} + \frac{h^2}{6} W}$$

$$\cong \frac{(MN) \cdot a_d^2 \cdot G_{rec}}{2\sigma_{rn}^2}. \tag{3.11}$$

Usually, SCR is less than 10,000 even for the brightest target. M and N are typically several hundred to thousand, or more. Thus the approximation in Eq. (3.11) is valid.

S_4 ADC saturation noise (x_4, y_4) generated when real, x, and/or imaginary, y, components of $S_1 + S_2 + S_3$ exceed C.

The saturation noise, S_4, introduced here is a non-stationary noise because it is driven by the stationary noise, S_3, and the time-dependent signal, $S_1 + S_2$.

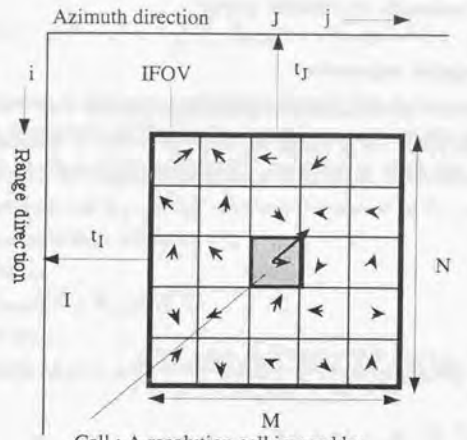

Fig. 3-3. Coordinate system of SAR imaging and the composition of the illuminated area.

3.2.3 Range and azimuth correlation power

General approach for model expression

SAR correlation, which means range and azimuth correlation processing, is performed in range and azimuth directions with different gains. Saturation in the ADC affects both correlations, causing loss of amplitude and phase information. Correlation of (3.1) can be expressed as follows:

$$\mathbf{S}_C(t',t'') = \sum_{m=1}^{4} \mathbf{S}_{cra,m}(t',t'') \tag{3.12}$$

$$\begin{aligned}\mathbf{S}_{cra,m}(t',t'') &\equiv \mathbf{S}_m \oplus \mathbf{g}_r^* \oplus \mathbf{g}_a^* \\ &= \frac{1}{\Delta\tau\Delta T}\int_{-T/2}^{T/2}\int_{-\tau/2}^{\tau/2}\sqrt{G_{rec}(t_1+t',t_2+t'')}\,\frac{\mathbf{S}_m(t_1+t',t_2+t'')}{\sqrt{G_{rec}(t_1+t',t_2+t'')}}\mathbf{g}_r^*(t_1)\mathbf{g}_a^*(t_2)dt_1dt_2 \\ &= \frac{\sqrt{G_{rec}(t',t'')}}{\Delta\tau\Delta T}\int_{-T/2}^{T/2}\int_{-\tau/2}^{\tau/2}\frac{\mathbf{S}_m(t_1+t',t_2+t'')}{\sqrt{G_{rec}(t_1+t',t_2+t'')}}\mathbf{g}_r^*(t_1)\mathbf{g}_a^*(t_2)dt_1dt_2\end{aligned} \tag{3.13}$$

$$\overline{\sqrt{G_{rec}(t',t'')}} = \frac{1}{\Delta\tau\Delta T}\int_{-T/2}^{T/2}\int_{-\tau/2}^{\tau/2}\sqrt{G_{rec}(t_1+t',t_2+t'')}dt_1dt_2 \tag{3.14}$$

$$\mathbf{g}_r(t) = \begin{cases} e^{-2\pi j\frac{k_r}{2}t^2} & |t| \le \tau/2 \\ 0 & |t| > \tau/2 \end{cases} \tag{3.15a}$$

$$\mathbf{g}_a(t) = \begin{cases} e^{-2\pi j\frac{k_a}{2}t^2} & |t| \le T/2 \\ 0 & |t| > T/2 \end{cases} \tag{3.15b}$$

where $\mathbf{S}_C$ is the SAR correlation output; $\mathbf{g}_r$ and $\mathbf{g}_a$ are the range and azimuth reference functions; "*" is the complex conjugate; $\oplus$ is the correlation operation; τ and T are the range and azimuth correlation durations; $\Delta\tau$ and ΔT are the Range and azimuth sampling intervals; and $\mathbf{S}_{cra,m}$ is the SAR correlation output for the m^{th} signal normalized by the receiver gain. $G_{rec}()$ is not correlated with the reference functions, so the moving average of receiver gain centered at t' and t'' is taken out of the integration. Then, the remained term is almost separated from the receiver gain. (t_1, t') and (t_2, t'') are the range and azimuth times. Note that the range curvature in azimuth processing is ignored for simplicity.

$\mathbf{S}_3$ is stationary Gaussian, and $\mathbf{S}_2$ is Gaussian in space but correlative in time. $\mathbf{S}_4$ and $\mathbf{S}_C$ are random processes. $\mathbf{S}_c$'s power, denoted by P_C, is given by two steps expectations, 1) an expectation over $\mathbf{S}_3$ leaving $\mathbf{S}_1$+$\mathbf{S}_2$ fixed, then, 2) an expectation over $\mathbf{S}_2$ as:

$$P_C(t',t'') = \left\langle \mathbf{S}_C(t',t'')\cdot\mathbf{S}_C^*(t',t'')\right\rangle = \sum_{m=1}^{4}\sum_{n=1}^{4}\left\langle \mathbf{S}_{cra,m}(t',t'')\cdot\mathbf{S}_{cra,n}^*(t',t'')\right\rangle , \tag{3.16}$$

where $\langle\cdot\rangle$ stands for the two step expectations mentioned above. Hereafter, "an expectation" is used for this meaning. It should be noted that $\mathbf{S}_2$ and $\mathbf{S}_3$ are essentially different processes: $\mathbf{S}_2$ correlates with the SAR reference signal; $\mathbf{S}_3$ is white noise. Introducing $\mathbf{R}_{mn}$, an expectation of the mutual correlation of $\mathbf{S}_m$ and $\mathbf{S}_n^*$, a mutual correlation of $\mathbf{S}_{cra,m}$ and $\mathbf{S}_{cra,n}^*$, denoted by $\mathbf{P}_{mn}$, can be expressed more effectively [3]:

$$\begin{aligned}P_{mn}(t',t'') &\equiv \left\langle \mathbf{S}_{cra,m}(t',t'')\cdot\mathbf{S}_{cra,n}^*(t',t'')\right\rangle \\ &= \frac{\overline{\sqrt{G_{rec}(t',t'')}}^2}{(\Delta\tau\Delta T)^2}\int_{-T/2}^{T/2}\int_{-T/2}^{T/2}\int_{-\tau/2}^{\tau/2}\int_{-\tau/2}^{\tau/2}\mathbf{R}_{mn}(t_1+t',t_2+t',t_3+t'',t_4+t'')\mathbf{g}_r^*(t_1)\mathbf{g}_r(t_2)\mathbf{g}_a^*(t_3)\mathbf{g}_a(t_4)dt_1dt_2dt_3dt_4\end{aligned} \tag{3.17}$$

$$\mathbf{R}_{mn}(t_1,t_2,t_3,t_4) = \frac{\left\langle \mathbf{S}_m(t_1,t_2)\cdot\mathbf{S}_n^*(t_3,t_4)\right\rangle}{G_2\cdot G_4}, (m,n \ge 2) \tag{3.18}$$

where $G_2 \equiv \sqrt{G_{rec}(t_2)}$ and $G_4 \equiv \sqrt{G_{rec}(t_4)}$. The expectations are calculated for m, n >= 2. In the following, the variables t_1, t_2, t_3, and t_4 are not written except when important. SAR correlation power can be calculated term-by-term.

Calculation of $\mathbf{P_{11}}$

$$\begin{aligned}\mathbf{R}_{11} &= \frac{\mathbf{S}_1\cdot\mathbf{S}_1^*}{G_2\cdot G_4} \\ &= \sum_i\sum_j a_{ij}e^{2\pi j\frac{k_r}{2}(t_1-\tau_i)^2+2\pi j\frac{k_a}{2}(t_2-\tau_j)^2+j\delta_{ij}}\cdot\sum_k\sum_l a_{kl}e^{-2\pi j\frac{k_r}{2}(t_3-t_k)^2-2\pi j\frac{k_a}{2}(t_4-t_l)^2-j\delta_{ij}},\end{aligned} \tag{3.19}$$

where t_i is the time delay in range and t_j is the azimuth time. An expectation is not applied because $\mathbf{S}_1$ does not depend on $\mathbf{S}_2$ or $\mathbf{S}_3$. Substituting (3.19) into (3.17), we have

$$\begin{aligned}P_{11} = \frac{\overline{\sqrt{G_{rec}(t',t'')}}^2}{(\Delta\tau\Delta T)^2}\sum_i\sum_j\sum_k\sum_l a_{ij}a_{kl}\tau^2T^2\frac{\sin\{\pi k_r\tau(t_i+t')\}}{\pi k_r\tau(t_i+t')}\cdot\frac{\sin\{\pi k_r\tau(t_k+t')\}}{\pi k_r\tau(t_k+t')}\cdot \\ \frac{\sin\{\pi k_aT(t_j+t'')\}}{\pi k_aT(t_j+t'')}\cdot\frac{\sin\{\pi k_aT(t_l+t'')\}}{\pi k_aT(t_l+t'')}\cdot e^{2\pi j\frac{k_r}{2}(t_i^2-t_k^2)+2\pi j\frac{k_a}{2}(t_j^2-t_l^2)+j(\delta_{ij}-\delta_{kl})},\end{aligned} \tag{3.20}$$

This is valid only when k = i and l = j as:

$$P_{11} = \overline{\sqrt{G_{rec}}}^2 \sum_i \sum_j a_{ij}^2 (MN)^2 \left[\frac{\sin\{\pi k_r \tau(t_i + t')\}}{\pi k_r \tau(t_i + t')}\right]^2 \left[\frac{\sin\{\pi k_a T(t_j + t'')\}}{\pi k_a T(t_j + t'')}\right]^2 \tag{3.21}$$

t_i and t_j distribute around t' and t'' respectively. Using SCR, (3.21) is modified to

$$P_{11} = \overline{\sqrt{G_{rec}}}^2 SCR \cdot a_d^2 \cdot (MN)^2 \cdot D \tag{3.22}$$

$$D = \sum_i \sum_j \left[\frac{\sin\{\pi k_r \tau(t_i + t')\}}{\pi k_r \tau(t_i + t')}\right]^2 \left[\frac{\sin\{\pi k_a T(t_j + t'')\}}{\pi k_a T(t_j + t'')}\right]^2 \Big/ \sum_i \sum_j 1 \tag{3.23}$$

Here, D is the weighting function for forming a resolution cell.

Calculation of $P_{14} + P_{41}$

S_1 is not a random process, so $\mathbf{R}_{14}+\mathbf{R}_{41}$ is given by:

$$\mathbf{R}_{14} + \mathbf{R}_{41} = \frac{\mathbf{S}_1 \cdot \langle \mathbf{S}_4^* \rangle + \langle \mathbf{S}_4 \rangle \cdot \mathbf{S}_1^*}{G_2 \cdot G_4} \tag{3.24}$$

$$\langle \mathbf{S}_4^* \rangle = \langle x_4 \rangle - j\langle y_4 \rangle \tag{3.25}$$

$$\langle x_4 \rangle = \frac{C - x_1}{2} Erfc\left(\frac{C - x_1}{\sqrt{2}\sigma}\right) - \frac{C + x_1}{2} Erfc\left(\frac{C + x_1}{\sqrt{2}\sigma}\right) - \frac{\sigma}{\sqrt{2\pi}} e^{-\frac{(C-x_1)^2}{2\sigma^2}} - \frac{\sigma}{\sqrt{2\pi}} e^{-\frac{(C+x_1)^2}{2\sigma^2}} \tag{3.26}$$

$$Erfc(x) = \frac{2}{\sqrt{\pi}} \int_x^\infty e^{-t^2} dt \tag{3.27}$$

The derivation of $\langle x_4 \rangle$ is given in Appendix 3-2, together with the other expectations. $\langle y_4 \rangle$ is obtained by replacing x_1 of $\langle x_4 \rangle$ by y_1. Erfc() is the Gaussian complementary error function. Because x_1 in $\langle x_4 \rangle$ is much smaller than C, $\langle x_4 \rangle$ can be Taylor expanded in x_1, and the first order terms are mixed up as,

$$\langle x_4 \rangle \equiv E \cdot x_1 \tag{3.28}$$

$$E \equiv -Erfc\left(\frac{1}{\sqrt{2}\eta}\right) \tag{3.29}$$

where $\eta = \sigma/C$. Then, (3.25) is rewritten as the correlative form.

$$\langle \mathbf{S}_4^* \rangle = E \cdot \mathbf{S}_1^* \tag{3.30}$$

Furthermore, (3.17) is rewritten as

$$\mathbf{R}_{14} + \mathbf{R}_{41} = 2 \cdot E \cdot \mathbf{R}_{11}. \tag{3.31}$$

Finally, we have

$$P_{14} + P_{41} = 2a_d^2 \cdot SCR \cdot (MN)^2 \cdot D \cdot E \cdot \overline{\sqrt{G_{rec}}}^2. \tag{3.32}$$

The reduction of the correlation power due to the saturation is clearly expressed in (3.32). The negative sign, contained in E, in this term arises from $\langle \mathbf{S}_4 \rangle$ and is reasonable because this instantaneous $\mathbf{S}_4$ generated in the saturation process is generally in the negative direction of $\mathbf{S}_1+\mathbf{S}_2+\mathbf{S}_3$. $\mathbf{S}_3$ is the Gaussian process with zero mean. An expectation of $\mathbf{S}_4$ over $\mathbf{S}_3$ becomes proportional to $-\mathbf{S}_1$, where the proportional factor is related to the saturation.

Calculation of P_{44}

S_4 consists of a deterministic component and a random component. The random component may make $\mathbf{R}_{44}$ to behave as a delta function at only around $t_1=t_3$, and $t_2=t_4$. The deterministic component behaves just as the square of $\langle \mathbf{S}_4 \rangle$ because $\mathbf{S}_4(t_1,t_2)$ and $\mathbf{S}_4^*(t_3,t_4)$ are independent of each other except when $t_1=t_3$ and $t_2=t_4$. $\mathbf{R}_{44}$ is given by

$$\begin{aligned}\mathbf{R}_{44}(t_1,t_2,t_3,t_4) &= \frac{\langle \mathbf{S}_4 \cdot \mathbf{S}_4^* \rangle (t_1,t_2,t_3,t_4)}{G_2 G_4} + \frac{\langle \mathbf{S}_4 \cdot \mathbf{S}_4^* \rangle\big|_{t_1=t_3, t_2=t_4}}{G_2 G_4} \delta(t_1 - t_3)\delta(t_2 - t_4) \\ &= E^2 \cdot \mathbf{R}_{11} + \frac{\langle \mathbf{S}_4 \cdot \mathbf{S}_4^* \rangle\big|_{t_1=t_3, t_2=t_4}}{G_2 G_4} \delta(t_1 - t_3)\delta(t_2 - t_4).\end{aligned} \tag{3.33}$$

The expectation power is then given by

$$P_{44} = \overline{\sqrt{G_{rec}}}^2 \left\{ E^2 \cdot SCR \cdot a_d^2 (MN)^2 \cdot D + \frac{\langle x_4^2 \rangle + \langle y_4^2 \rangle}{G_{rec}} (MN) \right\}. \tag{3.34}$$

Calculation of Remaining terms

The remaining terms are derived similarly to the above as:

$$P_{12} + P_{21} = 0 \tag{3.35}$$

$$P_{24} + P_{42} = 0 \tag{3.36}$$

$$P_{32} + P_{23} = 0 \tag{3.37}$$

$$P_{34} + P_{43} = 2\frac{\langle x_3 x_4 \rangle + \langle y_3 y_4 \rangle}{G_{rec}}(MN)\overline{\sqrt{G_{rec}}}^2 \tag{3.38}$$

$$P_{13} + P_{31} = 0 \tag{3.39}$$

$$P_{22} = 0 \tag{3.40}$$

$$P_{33} = \frac{2\sigma_m^2}{G_{rec}}(MN)\overline{\sqrt{G_{rec}}}^2 \tag{3.41}$$

Thematic expression of the correlation power

Rearranging (3.22), (3.32), and (3.34) to (3.41) and using $\langle x_3 x_4 \rangle$, $\langle x_4^2 \rangle$, $\langle y_3 y_4 \rangle$, and $\langle y_4^2 \rangle$, we get P_C:

$$P_C = \left\{ (MN)^2 \cdot SCR \cdot a_d^2 \cdot D \cdot V + (MN)\frac{2\sigma^2}{G_{rec}} U \right\} \overline{\sqrt{G_{rec}}}^2$$

$$= (MN)^2 a_d^2 \cdot (SCR \cdot D \cdot V + Q \cdot U)\overline{\sqrt{G_{rec}}}^2 \tag{3.42}$$

$$V = (1+E)^2 \tag{3.43}$$

$$U = \frac{1+2E}{1+SNR} - \left(1 + \frac{1}{\eta^2}\right) \cdot E - \sqrt{\frac{2}{\pi}}\frac{1}{\eta} e^{-\frac{1}{2\eta^2}} \tag{3.44}$$

$$2\sigma^2 = a_d^2 (MN) G_{rec} Q \tag{3.45}$$

$$S_a = Erfc\left(\frac{1}{\sqrt{2}\eta}\right) \tag{3.46}$$

$$Q = 1 + SNR^{-1} \tag{3.47}$$

where S_a is the saturation rate (described later), and D is the processing efficiency that is 1.0 for the point target and 0.73 for the distributed target. There are three important parameters in (3.42): V, U, and σ/C. V is the saturation-caused correlation gain loss for the correlative signal for the Cell; U is the correlation gain loss for the non-correlative signal outside the Cell, thermal noise, and ADC redundancy noise; and σ/C is the input power to ADC saturation level ratio, or "ISL." ISL depends on the signal-to-noise ratio (SNR), receiver gain (G_{rec}), and target brightness ($a_d^2 MN$). SNR depends on G_{rec}, $a_d^2 MN$, thermal noise, ADC quantization interval, and so on. Thus, ISL can be assumed to depend on the receiver gain and the target brightness.

Equation (3.42) means that the SAR image power of each pixel is composed of the correlation power of all the received signals from the scatterers within the Cell, the non-correlation power for all the remaining scatterers within the IFOV but not in Cell, the thermal noise, and ADC redundancy noise; the saturation reduces correlation and non-correlation powers rated by V and

U, respectively; the correlation gain loss depends on ISL, but not on the pixel brightness itself (SCR).

Consistency with the ADC-error-free case

We consider a case in which ADC does not generate saturation and redundancy noise. The SAR raw data then consists of signals from the resolution cell of interest, background signals, and thermal noise. Setting the saturation-related terms to zero in the above equation, we have

$$P_C = (MN)^2 a_d^2 \cdot \left(SCR \cdot D + \frac{Q}{1+SNR} \right) \overline{\sqrt{G_{rec}}}^2. \tag{3.48}$$

This is consistent with Freeman et al's result [4].

Standard deviation of the correlation signal power

The expectation of the standard deviation of the correlation power is calculated (Appendix 3-3) as the normalized standard deviation (K_{pc}), which is the standard deviation (σ_{PC}) divided by an average (P_C) as

$$K_{PC} \equiv \frac{\sigma_{PC}}{P_C} = \frac{\left[Q^2 \cdot U^2 / 4 + 2 \cdot SCR \cdot U \cdot V \cdot Q \right]^{1/2}}{SCR \cdot D \cdot V + Q \cdot U}. \tag{3.49}$$

3.2.4 A radar equation for the SAR correlation power

The radar equation for the background power (a_d^2) is

$$a_d^2 = \frac{P_t G_0^2 G_{ele}^2 \lambda^2}{(4\pi)^3 R^4} \sigma^0 \frac{\delta_a \delta_r}{\sin\theta} L, \tag{3.50}$$

where P_t is the transmission power; G_0 is the antenna peak gain (one way); G_{ele} is the antenna elevation gain (one way); λ is the wavelength; R is the slant range; σ^0 is the normalized radar cross section; δ_r and δ_a are the slant range and azimuth pixel spacings; θ is the local incidence angle; and L is a system loss. Generally, the N_L independent data are incoherently summed to suppress the speckle noise. This is so called look summation. Combining this with (3.42), the generalized radar equation for SAR correlation power becomes

$$P_C = (MN)^2 \frac{P_t G_0^2 G_{ele}^2 \lambda^2}{(4\pi)^3 R^4} N_L \sigma^0 \frac{\delta_a \delta_r}{\sin\theta} \cdot L \cdot (SCR \cdot D \cdot V + Q \cdot U)\overline{\sqrt{G_{rec}}}^2, \tag{3.51}$$

which we can use as the base for the SAR calibration. The equation (3.51) governs the relationships among the correlated signal power, the target backscattering characteristics, and the radar parameters. When P_C is expressed by a short integer value, such as 16-bit data, it is converted to

$$DN_{PC} = C_f \cdot N_L (MN)^2 \frac{P_t G_0^2 G_{ele}^2 \lambda^2}{(4\pi)^3 R^4} \sigma^0 \frac{\delta_r \delta_a}{\sin\theta} L(SCR \cdot D \cdot V + Q \cdot U) \overline{\sqrt{G_{rec}}}^2, \qquad (3.52)$$

where DN_{PC} is the digital number for the correlation power and C_f is the conversion factor. In (3.52), unknown parameters are constants and functions of slant range.

1) Constants

P_t, MN, δ_a, δ_r, λ, C_f, N_L, and L are radar and processor parameters. Some of these can be estimated from ground measurements acquired before launch. The possible gradual change of the sensor characteristics on orbit may, however, degrade the estimation.

2) Functions of slant range

The antenna elevation pattern (G_{ele}) and the slant range (R) change across the swath, so they must be accurately determined to calibrate SAR products. Determination of the slant range (R) requires the precise characterization of the time delay in the SAR transmitter and the receiver. The antenna elevation pattern can be determined in two ways. One is to deploy several reference targets with known radar cross sections at known locations over a swath and use them to derive the pattern. The other is to use a natural target with the same normalized radar cross section. The Amazon rain forest data can be used in the latter method, which will be discussed in Chapter 4.

3) Calibration method

After G_{ele} and R are determined precisely, the remaining problem is to determine the unknown parameters. If we set P_t, MN, λ, δ_r, δ_a and L to the representative values (ie., ground measurement values), C_f can be adjusted to make most of the DNs fit within the dynamic range of SAR product and also to relate DNs to σ^0. This is how to convert DN to σ^0. This will be discussed again in Chapter 5.

3.2.5 Several expressions for the real SAR data

We summarize several expressions for the real SAR products based on (3.51). For the SAR product that maintains the same azimuth resolution across the swath, Doppler band width should be constant. This implies that the azimuth correlation number (M) is proportional to the

slant range (R) and is expressed by the satellite ground speed (V_g), pulse repetition frequency (PRF), theoretical azimuth resolution (ρ_a), and wave length (λ). The range correlation number (N) is determined by the radar parameters, pulse duration (τ) and sampling frequency (f_{sample}):

$$M = \frac{PRF}{2V_g\rho_a}\lambda R \qquad (3.53)$$

$$N = \tau \cdot f_{sample} \qquad (3.54)$$

If we use scattering coefficient (γ) instead of σ^0, the final expression for the correlation signal power becomes:

$$P_C = \left(\text{tf}_{sample}\frac{PRF}{2V_g\rho_a}\lambda\right)^2 \frac{P_t G_0^2 G_{ele}^2 \lambda^2}{(4\pi)^3} N_L \frac{\gamma\cot\theta}{R^2} \cdot \delta_a \delta_r L \cdot (SCR \cdot D \cdot V)\overline{\sqrt{G_{rec}}}^2 + \left(\text{tf}_{sample}\frac{PRF}{2V_g\rho_a}\lambda\right)\frac{\overline{\sqrt{G_{rec}}}^2}{G_{rec}} RN_L 2\sigma_m^2(1+SNR)\cdot U \qquad (3.55a)$$

In case of the saturation-free, a more simplified equation is derived.

$$P_C = \left(\text{tf}_{sample}\frac{PRF}{2V_g\rho_a}\lambda\right)^2 \frac{P_t G_0^2 G_{ele}^2 \lambda^2}{(4\pi)^3} N_L \frac{\gamma\cot\theta}{R^2} \cdot \delta_a \delta_r L \cdot (SCR \cdot D)\overline{\sqrt{G_{rec}}}^2 + \left(\text{tf}_{sample}\frac{PRF}{2V_g\rho_a}\lambda\right)\frac{\overline{\sqrt{G_{rec}}}^2}{G_{rec}} RN_L 2\sigma_m^2 \qquad (3.55b)$$

3.3 Analysis of the Parameters

In the correlation power model of (3.42), U and V represent the power reduction quantities. In order to retrieve the saturation free signal power, U and V should be evaluated under the possible saturation condition represented by (σ/C). This section discusses the saturation rate, a comparison of the ADC output power and correlated signal power, an analysis of these parameters under JERS-1 SAR conditions, a model comparison with JERS-1 SAR data, and the receiver gain mode. Only three-bit ADC is considered.

3.3.1 Saturation rate

To express the saturation quantitatively, "Saturation rate," denoted by S_a, is introduced as the expected occurrence that the x or y component of $\mathbf{S}_1+\mathbf{S}_2+\mathbf{S}_3$ exists in all ADC conversion regions except IX (Fig. 3-2). Because the distribution functions $P(x_1+x_2)$ and $P(x_3)$ are Gaussian, the saturation rate of the x component is obtained as

$$Saturation\ rate = \int_{-\infty}^{\infty} P(x_1+x_2)\left\{\int_{C_{AD}-x_1-x_2}^{\infty} + \int_{-\infty}^{-C_{AD}-x_1-x_2} P(x_3)dx_3\right\}d(x_1+x_2) = Erfc\left(\frac{1}{\sqrt{2}\eta}\right). \tag{3.56}$$

This parameter has been already introduced in (3.42) as S_a. Because the two ADCs have the same characteristics, their saturation rates are the same. Fig. 3-4 shows the relation between the saturation rate and σ/C. The saturation rate increases simply with σ/C of greater than 0.4. JERS-1 SAR data, which is always slightly saturated with S_a = 4 to 5%, has a σ/C of 0.5 [1], [2].

3.3.2 Comparison of correlation and non-correlation power ratio

It is important to know the dependencies of the correlation power and the non-correlation power on the saturation and SNR. These power ratios, $\left(1+SNR^{-1}\right)U/(SCR\cdot D\cdot V)$, were calculated for SCR = 1, 10, and 100, and for SNR = 5 dB, 10 dB, and 20 dB. For these values, SCR = 1 corresponds to a wide area with similar brightness; SCR ≥ 100 corresponds to a bright point target (e.g., a corner reflector deployed on a dark target); and SNR = 20 dB is typical for the land (noise equivalent σ^0 for JERS-1 SAR is -20.5 dB, and σ^0 of land ranges from -10 dB to 0 dB [6]). Fig. 3-5 shows that the correlation power always exceeds the non-correlation power in the given η range; the correlation power becomes much more dominant than the non-correlation power as the SNR increases. Representative power ratios are listed in Table 3-1. From this table, the non-correlation power is around 30% of correlation power at SCR = 1, SNR = 5 dB and σ/C = 0.5; and the ratio at SNR = 20 dB and σ/C = 0.8 is 15%. The non-

correlation power therefore cannot be neglected. The expectation of the ADC output power (P_{raw}) is obtained in the same way that P_C has been derived (see Appendix 3-4):

$$P_{raw} = 2\sigma^2\left\{1-\frac{E}{\eta^2}-\sqrt{\frac{2}{\pi}}\frac{1}{\eta}e^{-\frac{1}{2\eta^2}}+\frac{SCR}{(MN)}\left(1-2S_a\right)\right\} \tag{3.57}$$

Dependence of the correlation gain loss in raw data power (P_{raw}) and the SAR image power (P_C) on the ISL is evaluated by using the parameters, $\Delta P_{raw} = P_{raw}/2\sigma^2$ and $\Delta P_C = P_C/\left\{(MN)^2\cdot a_d^2\cdot SCR\cdot D\right\}$. The results in Fig. 3-6 show that these two powers decrease as the ISL increases; the SAR image power decreases more than raw data power as the ISL increases (e.g., at σ/C of 0.8, ΔP_C is about -2 dB for SCR = 1 and ΔP_{raw} about -0.6 dB; at σ/C of 0.5, ΔP_C is -0.4 dB and ΔP_{raw} -0.2 dB); as SCR increases, the SAR image power asymptotically approaches the final curve.

Table 3-1. Representative non-correlation power to correlation power ratio

No.	SNR	0.5 of σ/C	0.8 of σ/C
1	5 dB	33%	47%
2	10 dB	11%	24%
3	20 dB	2%	15%

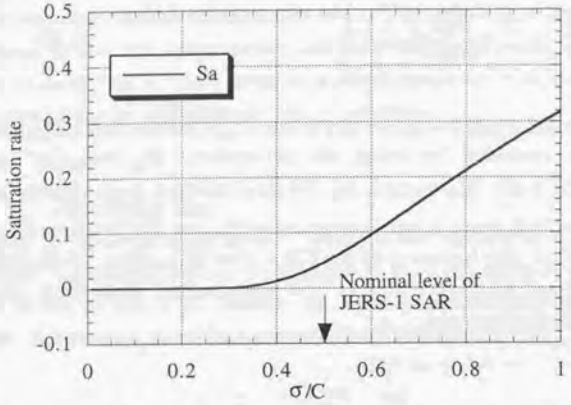

Fig. 3-4. Saturation rate vs. σ/C. Saturation rate increases simply with σ/C greater than 0.4. JERS-1 SAR data with a normal saturation rate of 4 to 5% corresponds to 0.5 of σ/C.

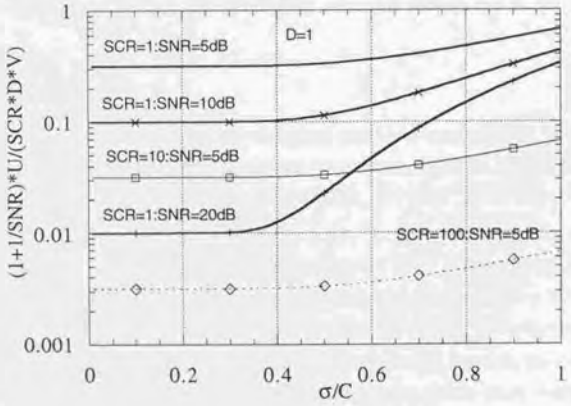

Fig. 3-5. Dependence of the ratio of the non-correlation power to the correlation power on saturation.

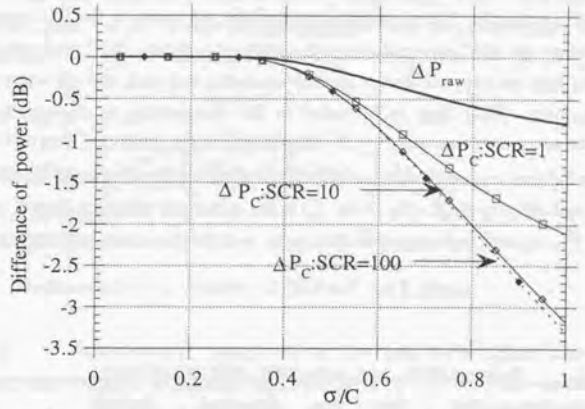

Fig. 3-6. Dependence of the raw data power and the SAR image power on saturation. As saturation increases, the correlation power decreases more with more SCR and raw data power decreases the least.

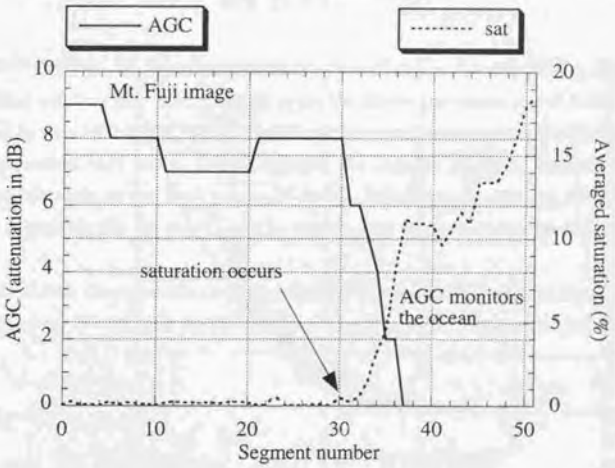

Fig. 3-7. AGC and saturation patterns for the Mt. Fuji image. When AGC monitors the ocean, AGC value goes to zero and the saturation goes up.

3.3.3 Comparing S_a for model and data

Two saturated raw data areas, south of Mt. Fuji and west of Beppu city, both in Japan, (Table 3-2) were evaluated for the saturation rate and the raw data power. As shown in Fig. 3-7, the measured saturation rate (Appendix 3-5) - averaged over all the segments in the full range - reaches 19% at worst, when the AGC monitoring window views the ocean. AGC value ranges from 0 to 9 dB when the data are not saturated or slightly saturated, and goes to 0 dB when the signal is heavily saturated. Note that AGC value is the attenuation in the receiver. Relationships between the saturation rate and P_{raw}/h^2 are plotted for the measured data and the model in Fig. 8. The solid line represents the model for which the output of the intermediate amplifier is controlled to 4 dBm as AGC (Fig. 3-1). ○ is the measured value for Beppu, and △ is that for Mt. Fuji. The models and measured data agree well for the saturation rate and the raw data power.

Table 3-2. Evaluated JERS-1 SAR images (refer [5] for path and row)

No.	Location	Lat. (deg)	Lon. (deg)	Path	Row	Acquisition	Remarks
1	Mt. Fuji	35.32	138.57	65	241	Sept. 7, 1995	325W of trans. power
2	Beppu	33.25	131.5	78	245	Nov. 3, 1995	325W ditto

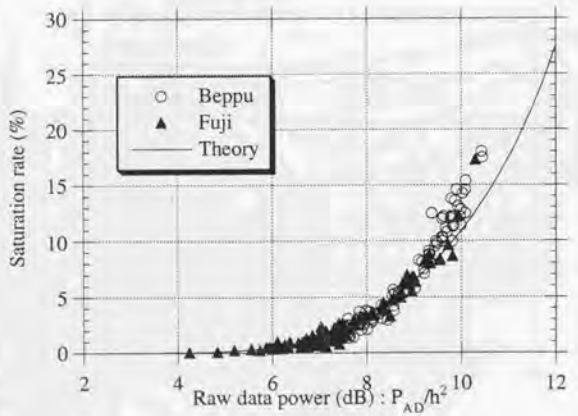

Fig. 3-8. Comparison of the measured saturation rate and the model using Ohita image (78-245) observed by JERS-1 SAR.

3.3.4 Receiver gain and the Gaussian power $2\sigma^2$

Two gain selecting modes are available in the JERS-1 SAR receiver: Manual Gain Control (MGC) and Automatic Gain Control (AGC). In the MGC mode, a constant gain is selected. In the AGC mode, the gain is selected automatically every 64 pulses to keep the ADC input power almost equal to $2\sigma_{cri}^2$ in 1 dB steps. Using the Gaussian notation $[\cdot]$, the noise power is

$$2\sigma^2 = (MN)a_d^2 \cdot Q \cdot 10^{0.1 \cdot IG_{rec}} \tag{3.58}$$

$$IG_{rec} = \left[10\log_{10}\left\{ \left(2\sigma_{cri}^2 - \frac{h^2}{6} W(\sigma_{cri}) \right) \Big/ \left((MN)a_d^2 + 2\sigma_{rn}^2 \right) \right\} \right] \tag{3.59}$$

3.4 Radiometric Correction of JERS-1 SAR Data

3.4.1 Radiometric correction of the saturated signal power

Since U and V behave differently depending on SNR and SCR, the received signal power can not be estimated accurately by subtracting the non-correlation power from the SAR image power. Allowing an error of 15% in the seriously saturated case (σ/C of 0.8 and SNR = 20 dB in Table I), we define the saturation-corrected SAR image power as

$$P_C' \equiv \frac{P_C}{V} = (MN)^2 a_d^2 SCR \cdot D \cdot \left(1 + \frac{1 + SNR^{-1}}{SCR \cdot D} \frac{U}{V} \right) \cong (MN)^2 a_d^2 SCR \cdot D, \tag{3.60}$$

for which V requires the measured saturation rate. If σ/C = 0.5 and SNR = 20 dB, the final modification can be valid. If we simply apply the above correction to the SAR image power (produced by considering G_{rec} only), S_a may not be exactly co-registered with the SAR image power and artifact may occur. This is because the location matching between raw data and SAR image depends on the SAR processor design, especially the azimuth reference function. Even if it is possible, the interpolation of S_a at each pixel location may cause artifacts.

Our proposal is to convolve the correction factor with the receiver gain correction during the SAR correlation. We call this the M-1 method. (see Fig. 3-9 for the correction flow)

M-1)

$$P_C' \propto \mathbf{f}_C' \cdot \mathbf{f}_C'^* \tag{3.61}$$

$$\mathbf{f}_C' \propto \left\{ \left(\sum_{m=1}^{4} \mathbf{f}_m \oplus \mathbf{g}_r^* \right) \cdot G_c \right\} \oplus \mathbf{g}_a^* \quad or \quad \left\{ \left(\sum_{m=1}^{4} \mathbf{f}_m \right) \cdot G_c \oplus \mathbf{g}_r^* \right\} \oplus \mathbf{g}_a^* \tag{3.62}$$

$$G_c = \frac{1}{\sqrt{G_{rec}} \cdot (1 - S_a)} \tag{3.63}$$

where P_c and $\mathbf{f}_c$ are the saturation-corrected SAR image power and its complex expression, respectively. For comparison, we define two simple methods, M-2 and M-3:

M-2) $G_{cr} \cong \frac{1}{\sqrt{G_{rec}}}$ (3.64)

M-3) $G_{cr} \cong 1$ (3.65)

M-1 requires measurement of S_a and the receiver gain G_{rec}, and may require more execution time with better accuracy. M-2 only corrects the receiver gain, which does not provide sufficient correction for heavy saturation. M-3 does not correct receiver gain (AGC).

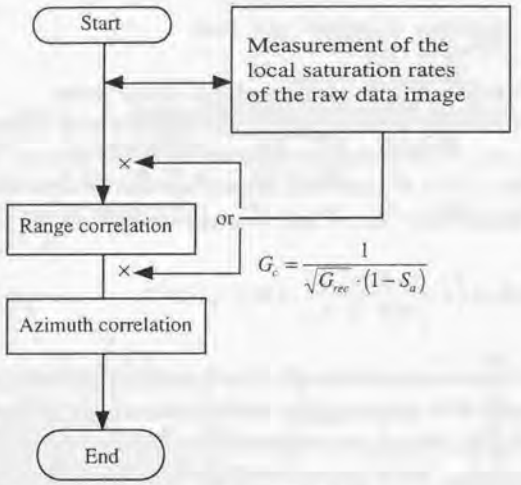

Fig. 3-9. A correction flowchart for M-1.

3.4.2 Simulation

A simulation study is conducted to estimate the saturation-free SAR image power for MGC and AGC modes and for the methods M-1 and M-2 (Table 3-3). Three cases (SCR = 1, 10, and 100) are examined in this simulation. Fig. 3-10 shows the correction error in MGC and Fig. 3-11 in AGC.

i) MGC In general, the error increases as the ISL increases. In M-2, the normal JERS-1 SAR conditions cause an error of -0.4 dB; the error becomes around -2 dB at a

saturation rate of 20% ($\sigma/C = 0.8$). M-1 succeeds in saturation correction even for SCR = 1, yielding an error of 0.5 dB for a saturation rate of 20%.

ii) AGC There are several differences. First, M-2 reduces the error to less than 0.3 dB and produces a saw pattern, which is driven by the AGC's step-like operation. Second, M-1 succeeds almost perfectly in saturation correction regardless of SCR (error is around 0.04 dB at SCR = 1).

The normalized standard deviations (K_{pc}s) for SAR image power saturation-corrected by M-1 are shown in Figs 3-12 and 3-13. The MGC case (Fig. 3-12) shows that the correction error increases as SCR decreases and as saturation increases. This is because the non-correlation powers are produced by a random process and K_{PC} may gradually approach 1.0 for SCR = 1. The AGC case (Fig. 3-13) shows that the correction error does not depend on the σ/C). The slight stepwise pattern is due to the AGC gain changes. Up to $\sigma/C = 0.5$, MGC and AGC yield the same K_{PC} value. Above that input level, MGC becomes less accurate but AGC remains accurate.

From the above, we conclude that M-1 corrects the saturated SAR data more accurately than M-2 for both AGC and MGC, that a combination of M-1 and AGC is the best for saturation correction, and that M-1 attains a correction accuracy of 0.04 dB at SCR = 1 and saturation rate of 20% and smaller value for high SCR.

Table 3-3. Simulation condition

No.	Items	Description
1	ADC	3-bit ADC with h=0.128 V and C = 0.512 V
2	$\overline{SNR}$	20 dB
3	MGC	Constant gain is used. G_{rec} = 0 dB
4	AGC	Selects the receiver gain in 1 dB steps to keep the ADC input power less than 0 dBm.
5	Impedance	50 ohm
6	SCR	1, 10, 100, 1000

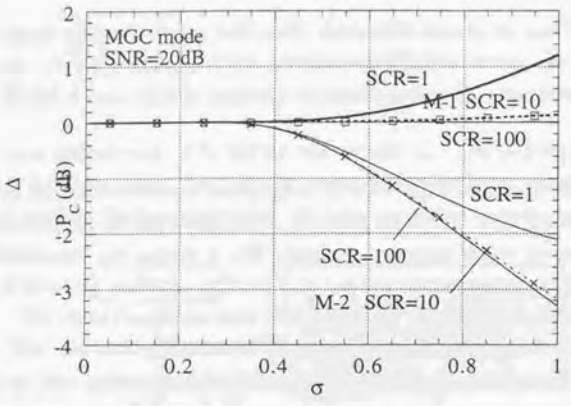

Fig. 3-10. Saturation correction error for the data acquired in MGC mode. The error in M-1 in the high σ/C region is much smaller than that in M-2.

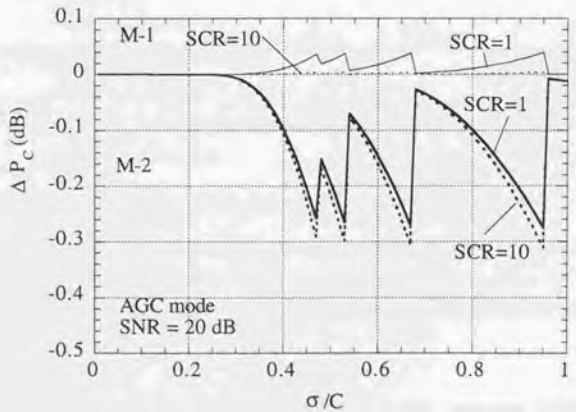

Fig. 3-11. Saturation correction error for the data acquired in AGC mode. M-1 produces the smaller errors than M-2; both M-1 and M-2 encounter the smaller error than these in MGC and do not vary at high σ/C.

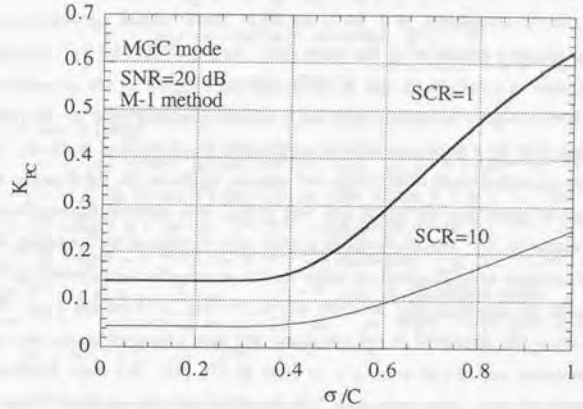

Fig. 3-12. Accuracy of the power estimation by M-1 in MGC mode.

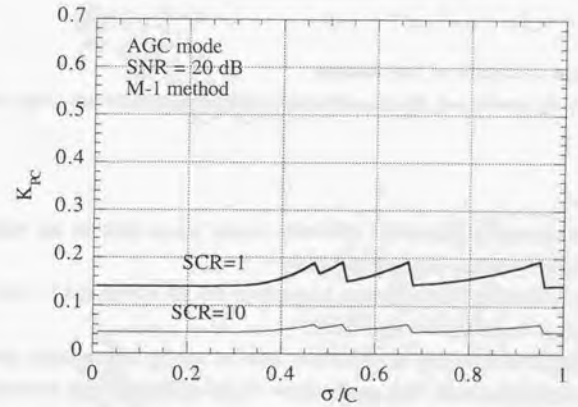

Fig. 3-13. Accuracy of the power estimation by M-1 in AGC mode.

3.4.3 Comparison of images corrected by M-1, M-2, and M-3

A 40 Km (south) x 6.1 km (east) image, which includes Mt. Fuji (lat. 33 19', lon 131 34'), Japan, the north side of which is a non-saturated area and the south side of which is a saturated area, were corrected by the three methods, M-1, M-2, and M-3. Their related figures (Figs 3-14 (a), (b), and (c)) were visually enhanced in the same way. As shown in Fig. 3-7, the right half of the image is saturated at a maximum rate of 20%, and the left half is not so saturated (2.5% or so). Because both a highly saturated area and a normal intensity area are included simultaneously, this image may be a good example for evaluating the correction method. The original image looks fully saturated south of Mt. Fuji and appears bright in (c). M-2 makes the north side of the mountain brighter than the south side area in (b). M-1 corrects the brightness uniformly over the full image in (a). The along-track profile was calculated by averaging the intensity over 8 pixels in azimuth and 320 pixels in range for the rectangular area (boxed in Fig. 3-14-b), and the two results are shown in Fig. 3-15 for Beppu and Fig. 3-16 for Mt. Fuji. The calibration instruments were not deployed in the saturated and non-saturated areas, thus we cannot discuss the radiometric correction accuracy as done in [7], [8]. We may, however, assume the average normalized radar cross section of both saturated and non-saturated areas to be the same. We conclude that M-1 can recover the saturated images. In contrast, M-2 undercorrects the Beppu image by 1 dB and the Fuji image by 2 dB ("undercorrect" means that the corrected image for the saturated area is darker than the non-saturated area). M-3 does not correct the saturation or AGC.

3.4.4 Merits and demerits of the method

We will now summarize the merits and the demerits of the proposed method (M-1) and the current method (M-2).

Proposed method (M-1):

Merits	It can accurately correct the saturation caused power loss for the bright target, depending on the SNR and SCR. It can correct the clutter with an accuracy of 0.6 dB in bias and 1.7 dB in random at the saturation rate of 20%.
Demerits	It requires a saturation measurement over an image, and requires more computational power. It is not available for the extremely high saturation case (when the denominator becomes zero).

Current method (M-2):

Merits	Simple operation.
Demerits	It can not correct the saturation caused power loss and leaves the gradual intensity change along the azimuth.

The estimated σ^0 has bias error of 1.5 dB and random error of 1.7 dB for clutter at a saturation rate of 20%.

The estimated σ^0 has bias error of 2.0 dB and the smaller random error for the brighter target at a saturation rate of 20%.

3.5 Conclusions

A radiometric correction method for the saturated SAR images has been proposed. This method corrects the decreased correlation gain, which is due to the raw data saturation. The theoretical models are derived for the expected retrieved signal power and its normalized standard deviation as a function of the saturation rate. The distribution of the saturation rate over an image is then required. Correction can be conducted either for range correlation or azimuth correlation. Several simulations using the JERS-1 SAR saturated images have shown that the proposed method can correct the saturation.

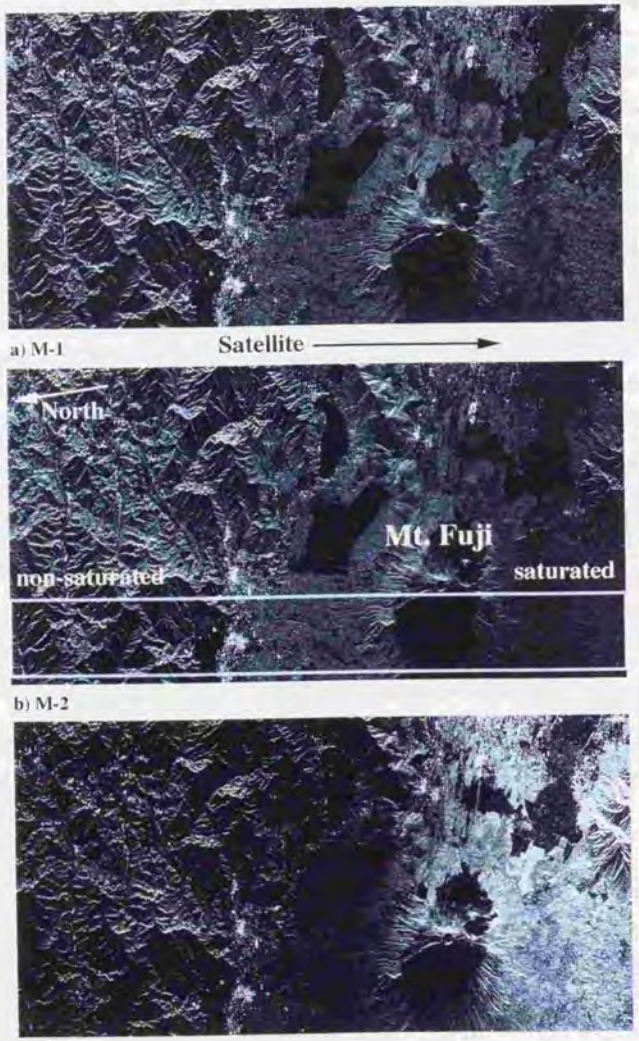

Fig. 3-14. SAR slant range 45 km (south) x 22.5 km (east) image of the Fuji area. (a), (b), and (c), are corrected by M-1, M-2, and M-3.

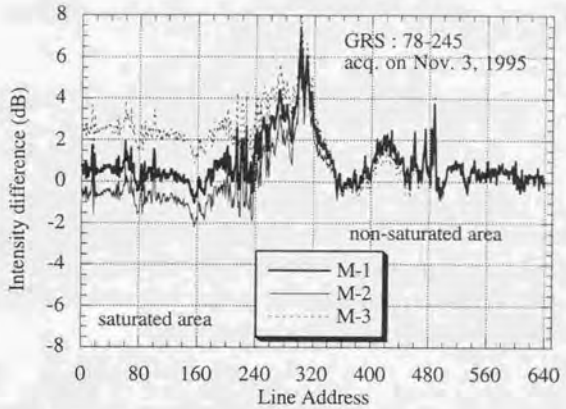

Fig. 3-15. Averaged power profile of Beppu image.

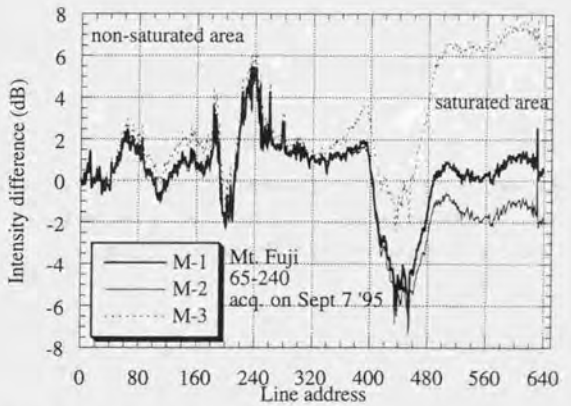

Fig. 3-16. Averaged power profile of Mt. Fuji image.

Appendix 3-1 ADC redundancy noise

ADC redundancy noise, σ^2_{ADC}, is given by

$$\sigma^2_{ADC} = \left\langle \left(X_{ADC} - X\right)^2 \right\rangle, \tag{3A-1.1}$$

where

$$X_{ADC} = \left[\frac{X}{h} + 0.5\right] \cdot h \tag{3A-1.2}$$

is the ADC output; X is the input voltage to ADC; h is the ADC conversion interval; [ ] is the truncation operation; and $\langle\ \rangle$ is the expectation. A Gaussian distributed signal with $2\sigma^2$ of power is the input. The above expression can be calculated for each ADC interval. Integration over 2^L interval gives the final expression for the ADC redundancy noise

$$\sigma^2_{ADC} = \frac{\sigma^2}{2} Erfc\left(-\frac{2^{L/2}\cdot h}{\sqrt{2}\sigma}\right) - \sqrt{\frac{2}{\pi}}\frac{h\sigma}{2}\sum_{i=-2^{L/2}}^{2^{L/2}-1}\left\{e^{-\frac{(i+1)^2h^2}{2\sigma^2}} + e^{-\frac{i^2h^2}{2\sigma^2}}\right\}$$
$$+\frac{h^2}{2}\left(2^L + 0.5\right)Erfc\left(-\frac{2^{L/2}\cdot h}{\sqrt{2}\sigma}\right) + \frac{h^2}{2}\sum_{i=-2^{L/2}}^{2^{L/2}-1}\left\{i\cdot Erfc\left(\frac{i\cdot h}{\sqrt{2}\sigma}\right) + (i+1)Erfc\left(\frac{(i+1)\cdot h}{\sqrt{2}\sigma}\right)\right\}. \tag{3A-1.3}$$

We define a weighting factor

$$W = \sigma^2_{ADC}\cdot\frac{12}{h^2}, \tag{3A-1.4}$$

which is normalized by the variance of a signal that is normally distributed and not saturated. W vs. $2\sigma^2$ is shown for the 3 bit ADC in Fig 3A-1. The figure shows that for a power less than 9 dBm, W exceeds 1.0 and when P_{in} exceed 5 dBm, W becomes less than 1.0.

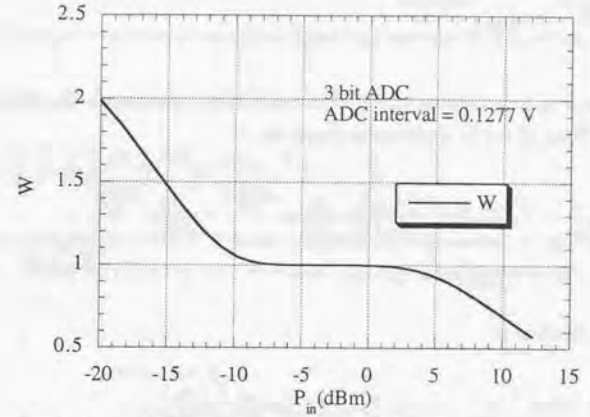

Fig. 3A-1. Weighting factor vs. the ADC input power

Appendix 3-2 Expectation of x_4

An expectation of x_4 is given by:

$$\langle x_4\rangle = \int_{-\infty}^{\infty} F(x_1, x_2)\cdot P(x_2)dx_2 \tag{3A-2.1}$$

$$F(x_1, x_2) = \int_{C-x_1-x_2}^{\infty}(C - x_1 - x_2 - x_3)P(x_3)dx_3 + \int_{-\infty}^{-C-x_1-x_2}(-C - x_1 - x_2 - x_3)P(x_3)dx_3 \tag{3A-2.2}$$

$$P(x_2) = \frac{1}{\sqrt{2\pi}\sigma_n}e^{-\frac{(x_2)^2}{2\sigma_n^2}} \tag{3A-2.3}$$

$$P(x_3) = \frac{1}{\sqrt{2\pi}\sigma_m}e^{-\frac{(x_3)^2}{2\sigma_m^2}} \tag{3A-2.4}$$

$$2\sigma^2 = 2\sigma_n^2 + 2\sigma_m^2 = 2\sigma_m^2(SNR+1) \tag{3A-2.5}$$

The term-by-term calculation gives

$$F(x_1,x_2)=\frac{C-x_1-x_2}{2}Erfc\left(\frac{C-x_1-x_2}{\sqrt{2}\sigma_m}\right)-\frac{C+x_1+x_2}{2}Erfc\left(\frac{C+x_1+x_2}{\sqrt{2}\sigma_m}\right)$$
$$-\frac{\sigma_m}{\sqrt{2\pi}}e^{-\frac{(C-x_1-x_2)^2}{2\sigma_m^2}}-\frac{\sigma_m}{\sqrt{2\pi}}e^{-\frac{(C+x_1+x_2)^2}{2\sigma_m^2}} \quad (3A\text{-}2.6)$$

(3A-2.1) means that x_2+x_3 is a variable which distributes in the convoluted distribution function of x_2 and x_3. Then, (3A-2.1) is expressed simply by

$$\langle x_4\rangle=\frac{C-x_1}{2}Erfc\left(\frac{C-x_1}{\sqrt{2}\sigma}\right)-\frac{C+x_1}{2}Erfc\left(\frac{C+x_1}{\sqrt{2}\sigma}\right)-\frac{\sigma}{\sqrt{2\pi}}e^{-\frac{(C-x_1)^2}{2\sigma^2}}-\frac{\sigma}{\sqrt{2\pi}}e^{-\frac{(C+x_1)^2}{2\sigma^2}} \quad (3A\text{-}2.7)$$

A similar expression is obtained as

$$\langle x_4^2\rangle=\frac{1}{2}\left\{(C-x_1)^2+\sigma^2\right\}Erfc\left(\frac{C-x_1}{\sqrt{2}\sigma}\right)+\frac{1}{2}\left\{(C+x_1)^2+\sigma^2\right\}Erfc\left(\frac{C+x_1}{\sqrt{2}\sigma}\right)$$
$$-\frac{\sigma}{\sqrt{2\pi}}\left\{(C-x_1)e^{-\frac{(C-x_1)^2}{2\sigma^2}}+(C+x_1)e^{-\frac{(C+x_1)^2}{2\sigma^2}}\right\}$$
$$\equiv\left(C^2+\sigma^2\right)\cdot Erfc\left(\frac{C}{\sqrt{2}\sigma}\right)-\sqrt{\frac{2}{\pi}}C\sigma e^{-\frac{C^2}{2\sigma^2}}. \quad (3A\text{-}2.8)$$

$\langle x_3x_4\rangle$ is expressed by

$$\langle x_3x_4\rangle=\int_{-\infty}^{\infty}P(x_2)\cdot G(x_1,x_2)dx_2,$$

$$G(x_1,x_2)=-\frac{\sigma_m^2}{2}\left\{Erfc\left(\frac{C-x_1-x_2}{\sqrt{2}\sigma_m}\right)+Erfc\left(\frac{C+x_1+x_2}{\sqrt{2}\sigma_m}\right)\right\}.$$

Numerical simulation solves the above formula as

$$\langle x_3x_4\rangle\equiv-\frac{\sigma^2}{1+SNR}Erfc\left(\frac{C}{\sqrt{2}\sigma}\right). \quad (3A\text{-}2.9)$$

Appendix 3-3 Normalized standard deviation

Normalized standard deviation K_{PC} is given by

$$K_{PC}\equiv\frac{\sqrt{V_{PC}-P_C^2}}{P_C}. \quad (3A\text{-}3.1)$$

The fourth order moment of correlated signal f is expressed by V_{PC} and is given by

$$V_{PC}=\left\langle\left(\mathbf{S}_C\cdot\mathbf{S}_C^*\right)^2\right\rangle$$
$$=\sum_{m=1}^{4}\sum_{n=1}^{4}\sum_{k=1}^{4}\sum_{l=1}^{4}\left\langle\mathbf{S}_{cra,m}\cdot\mathbf{S}_{cra,n}^*\cdot\mathbf{S}_{cra,k}\cdot\mathbf{S}_{cra,l}^*\right\rangle. \quad (3A\text{-}3.2)$$

Summation of 256 (=4*4*4*4) terms produces the expectation of squared correlated signal power. Using the following two conditions, K_{PC} can be calculated to be (3.31).

$$x_1\equiv y_1\equiv 0 \quad (3A\text{-}3.3)$$

$$\begin{aligned}\langle x_1x_2x_3x_4\rangle&=\langle x_1\rangle\langle x_2\rangle\langle x_3\rangle\langle x_4\rangle\\&+\langle x_1\rangle\langle x_2x_3x_4\rangle\delta(t_2-t_3)\delta(t_3-t_4)+.....\\&+\langle x_1x_2\rangle\langle x_3x_4\rangle\delta(t_2-t_1)\delta(t_4-t_3)+.....\\&+\langle x_1x_2x_3x_4\rangle\delta(t_1-t_2)\delta(t_2-t_3)\delta(t_3-t_4)\\&+\langle x_1\rangle\langle x_2\rangle\langle x_3x_4\rangle\delta(t_3-t_4)+.....\end{aligned} \quad (3A\text{-}3.4)$$

Appendix 3-4 ADC output power (Raw data power)

Raw data power, denoted by P_{raw}, is obtained in two steps in the same way as $\mathbf{R}_{mn}$ of Section 2.

$$P_{raw}\equiv\left\langle\mathbf{S}_4\cdot\mathbf{S}_4^*\right\rangle$$
$$=\left\langle\mathbf{S}_1\cdot\mathbf{S}_1^*\right\rangle+\left\langle\mathbf{S}_2\cdot\mathbf{S}_2^*\right\rangle+\left\langle\mathbf{S}_3\cdot\mathbf{S}_3^*\right\rangle+\left\langle\left(\mathbf{S}_1\cdot\mathbf{S}_2\right)^*\right\rangle+\left\langle\left(\mathbf{S}_2\cdot\mathbf{S}_3\right)^*\right\rangle+\left\langle\left(\mathbf{S}_1\cdot\mathbf{S}_3\right)^*\right\rangle \quad (3A\text{-}4.1)$$

$$\left\langle\mathbf{S}_1\cdot\mathbf{S}_1^*\right\rangle=\left\langle x_1^2\right\rangle+\left\langle y_1^2\right\rangle=G_{rec}a_d^2\cdot SCR \quad (3A\text{-}4.2)$$

$$\left\langle\mathbf{S}_2\cdot\mathbf{S}_2^*\right\rangle=\left\langle x_2^2\right\rangle+\left\langle y_2^2\right\rangle=2\sigma^2 \quad (3A\text{-}4.3)$$

$$\left\langle\mathbf{S}_3\cdot\mathbf{S}_3^*\right\rangle=\left\langle x_3^2\right\rangle+\left\langle y_3^2\right\rangle \quad (3A\text{-}4.4)$$

$$\left\langle\left(\mathbf{S}_1\cdot\mathbf{S}_2\right)^*\right\rangle=\left\langle\mathbf{S}_1^*\cdot\mathbf{S}_2+\mathbf{S}_1\cdot\mathbf{S}_2^*\right\rangle=\left\langle 2x_1\langle x_2\rangle+2y_1\langle y_2\rangle\right\rangle=\langle 2x_1 0+2y_1 0\rangle=0 \quad (3A\text{-}4.5)$$

$$\left\langle\left(\mathbf{S}_2\cdot\mathbf{S}_3\right)^*\right\rangle=\left\langle\mathbf{S}_2^*\cdot\mathbf{S}_3+\mathbf{S}_2\cdot\mathbf{S}_3^*\right\rangle=2\langle x_2x_3\rangle+2\langle y_2y_3\rangle \quad (3A\text{-}4.6)$$

$$\left\langle\left(S_1\cdot S_3\right)^*\right\rangle=\left\langle\mathbf{S}_1^*\cdot\mathbf{S}_3+\mathbf{S}_1\cdot\mathbf{S}_3^*\right\rangle=\left\langle 2x_1\langle x_3\rangle+2y_1\langle y_3\rangle\right\rangle \quad (3A\text{-}4.7)$$

In the right side of (3A-4.1), the first, second, and third terms are positive. The fifth term is negative because x_3 is opposite to x_2. The sixth term is also negative because x_1 and $\langle x_3\rangle$ are

opposite. Therefore, the saturation reduces the non-saturated ADC output power [1], [6]. Finally, we obtain

$$P_{raw} = 2\sigma^2\left\{1-\frac{E}{\eta^2}-\sqrt{\frac{2}{\pi}}\frac{1}{\eta}e^{-\frac{1}{2\eta^2}}+\frac{SCR}{(MN)}(1-2\cdot S_a)\right\}. \quad \text{(3A-4.8)}$$

Appendix 3-5 Measured saturation rate, $\overline{S_a}$

The actual saturation rate, $\overline{S_a}$, can be measured from the raw data as follows. An image is segmented into small pieces, each of which is 512 pixels in range and 64 pixels in azimuth. Normalized histogram, $h_m[i]$ with i = 0 to 7, is measured for each segment. The histogram $h_m[i]$ for i = 1 to 6 is Gaussian distributed. Then, the following equation is obtained:

$$\int_{0.5}^{6.5}\frac{1}{\sqrt{2\pi\sigma}}e^{-\frac{(x-\mu)^2}{2\sigma^2}}dx=\sum_{i=1}^{6}h_m[i]. \quad \text{(3A-5.1)}$$

μ is calculated by the measurement, then the unknown σ is determined by the iteration method. Finally the measured saturation rate can be obtained by the following parameter:

$$\overline{S_a}=1-\int_{-0.5}^{7.5}\frac{1}{\sqrt{2\pi\sigma}}e^{-\frac{(x-\mu)^2}{2\sigma^2}}. \quad \text{(3A-5.2)}$$

References

[1] M. Shimada, M. Nakai, and S. Kawase, "Inflight Evaluation of the L-band SAR of JERS-1," Canadian Journal of Remote Sensing, vol. 19, no. 3, pp. 247- 258, Aug. 1993.

[2] M. Shimada, and M. Nakai, "Inflight Evaluation of L band SAR of Japanese Earth Resources Satellite-1," Adv. Space Res. 14, 3, pp. 231-240, 1994.

[3] A. Papoulis, "Signal Analysis Part three, Data smoothing and spectral estimation," McGRAW-HILL BOOK COMPANY.

[4] A. Freeman and J. C. Curlander, "Radiometric correction and calibration of SAR images," Photogrammetric Engineering and Remote Sensing, vol. 55, no. 9, pp. 1295-1301, 1989.

[5] M. Shimada, T. Nagai, and S. Yamamoto, "JERS-1 Operation Interface Specification," NASDA document, HE-89033, Nov. 07 1991 revision-3.

[6] Y. Nemoto, H. Nishino, M. Ono, H. Mizutamari, K. Nishikawa, and K. Tanaka, "Japanese Earth Resources Satellite-1 Synthetic Aperture Radar," Proc. of the IEEE. vol. 79, no. 6, pp. 800-809, June 1991.

[7] A. Laurence Gray, P. W. Vachon, C. E. Livingstone, and T. I. Lukowski, "Synthetic Aperture Radar Calibration Using Reference Reflectors," IEEE Trans. Geosci. Rem. Sens., vol. 28, no. 3, pp 374-383, May 1990.

[8] L. M. H. Ulander, "Accuracy of Using Point Targets for SAR Calibration," IEEE Trans. Aerosp. Electronic Systems, vol. 27, no. 1, pp. 139-148, Jan. 1991.

CHAPTER 4 MEASUREMENT OF SPACEBORNE SAR ANTENNA PATTERNS USING DISTRIBUTED TARGETS

4.1 Introduction

From the studies on the inflight antenna elevation pattern determination conducted by Moore et al [1], [2], Shimada el. al. [13], Hawkins [5], and Dobson et. al. [3], it has been known that distributed target data offer the best prospects for precise measurement of the elevation antenna patterns of SARs. This is mainly because of an availability of the large number of data points, which results in reduction of the statistical errors. The major uncertainty in this approach is in the reliability of the scattering coefficients. For most spaceborne SARs, however, in which the imaged swath mainly represents a few degrees of variation in off-nadir angle, the incidence angle variation in scattering coefficient is much less of a problem than for airborne SARs.

This chapter focuses on obtaining the antenna pattern of a spaceborne SAR antenna utilizing scattering data from a set of possible distributed targets, including the Amazon and Sumatra rain forests, the Illinois farm land and the Canadian boreal forest. In this method, we assume that the image swath is so small that the scattering coefficient does not change there. The novel features of this study are (1) in the use of a screening process to ensure similarity between scattering areas from the selected scenes on the basis of texture analysis, (2) reduction of the noise power from the correlated image and (3) stochastic estimation of the antenna pattern as the solution of a maximum likelihood estimation. We discuss how to determine the size of the image for evaluation in azimuth and range, confidence value criteria for the screening process, the polynomial order of the antenna pattern model, the repeatability of the evaluation, and the effects of noise reduction.

The ANNEX 4 of this chapter describes a study on the JERS-1 SAR case. JERS-1 SAR is a more complicated system comparing to, for example, SIR-B, because of its two time variable functions, sensitivity time control (STC) and automatic gain control (AGC).

4.2 Principle

In this study we assume that the SAR amplitude images are correlated in the range and azimuth directions, with neither radiometric correction nor geographic mapping transformation. Further we assume that images are generated from saturation-free signals; the only noise considered in this study is the thermal noise. We will use SIR-B data, because SIR-B imaged several distributed target areas, such as in the Amazon, Illinois, Canada, etc. during its mission life. It can be supposed that a fully-developed distributed target is composed of a huge amount of small point targets, and the electric characteristics of the reflected signals from it follow the Rayleigh distribution for the amplitude and uniform distribution for the phase. The signal received by SAR becomes a sum of Gaussian signals from these small targets and internal noise of the SAR receiver. The receiver noise can be assumed to be time-invariant noise. The expectation of the correlated image power is obtained as a product of the processor gain and the expected raw signal power. Each pixel's expectation, P_C, is then given by a sum of the signal part P_{CS} and the noise part P_{CN} in reference to the previous chapter and to Freeman and Curlander [12] (related coordinate systems are shown in [A] of Figs 4-1 and 4-2):

$$P_C = P_{CS} + P_{CN} \tag{4.1}$$

$$P_{CS} = \left(\frac{PRF \cdot \lambda}{2V_g\rho_a}\right)^2 L_W N_L \cdot \frac{P_t\lambda^2\delta_a\delta_r}{(4\pi)^3} \cdot G^2(\phi) \cdot \frac{\gamma \cot\theta}{R^2} \tag{4.2}$$

$$P_{CN} = B \cdot R \tag{4.3}$$

$$B = \frac{PRF \cdot \lambda}{2V_g\rho_a} L_W \cdot N_L \cdot \overline{P_N} \tag{4.3a}$$

where V_g is the platform ground speed; PRF is the pulse repetition frequency; L_W is the loss in the peak signal strength due to the azimuth and range reference function weighting; N_L is the number of looks; ρ_a is the azimuth theoretical resolution; δ_a is the azimuth pixel spacing; δ_r is the range pixel spacing; G is the antenna elevation pattern (one way); γ is the scattering coefficient ($= \sigma^0/\cos\theta$: constant); R is the slant range; θ is the local incidence angle; ϕ is the off nadir angle; P_t is the transmitted peak power; λ is the wavelength; and $\overline{P_N}$ is the mean noise power. The SAR image is designed to keep the azimuth resolution constant over the full image swath by selecting the azimuth correlation length proportional to the slant range. P_{CS} is then proportional to R^{-2}, P_{CN} to R.

If we know γ as a function of θ, the estimated value of P_{CN} (from system tests or analysis of the range spectrum), and the estimated value of P_C, then the antenna pattern can be estimated by a simple rearrangement of (4.1), where P_C is converted to G point-by-point over the whole image. This formulation requires a knowledge of the local incidence angle, for which we may take two approaches: to select a flat and uniform area or to utilize a Digital Elevation Model (DEM) for the scene.

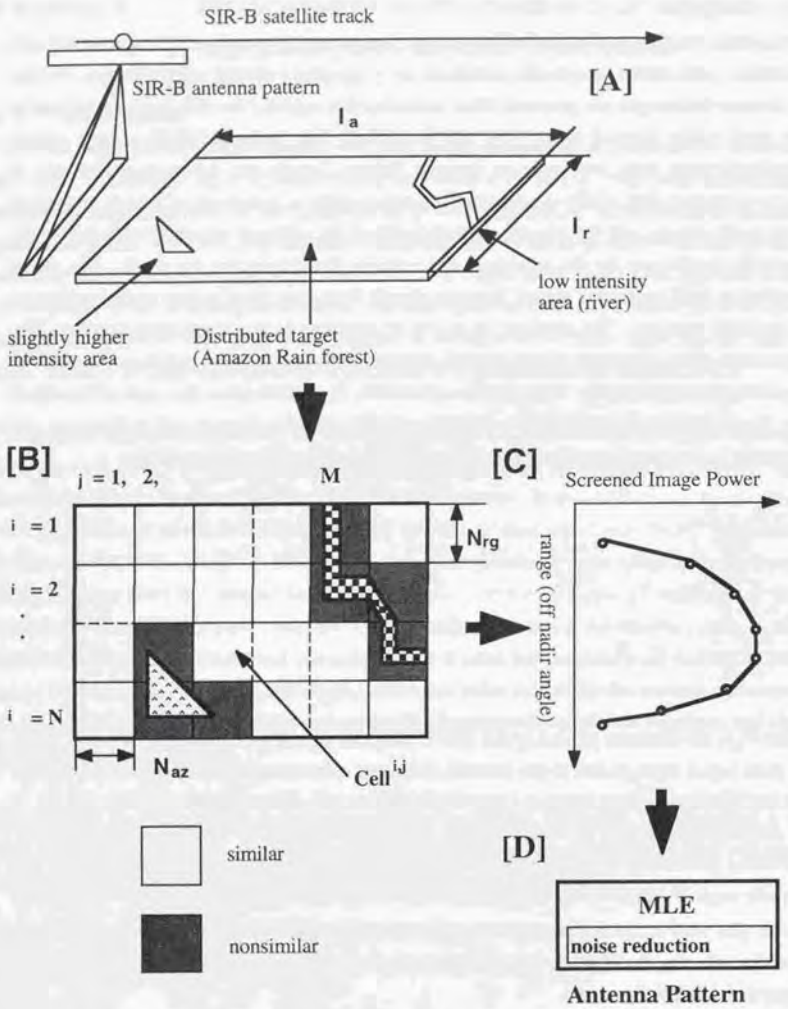

Fig. 4-1. General processing flow of this study. [A] SAR images the distributed area. [B] the image is divided into many Cells, each of which has the size of Nrg and Naz, so that they can be screened using the χ^2 similarity test. [C] Averaged image power versus off nadir angle is obtained. [D] Finally, the antenna pattern is modeled and fitted to the image powers.

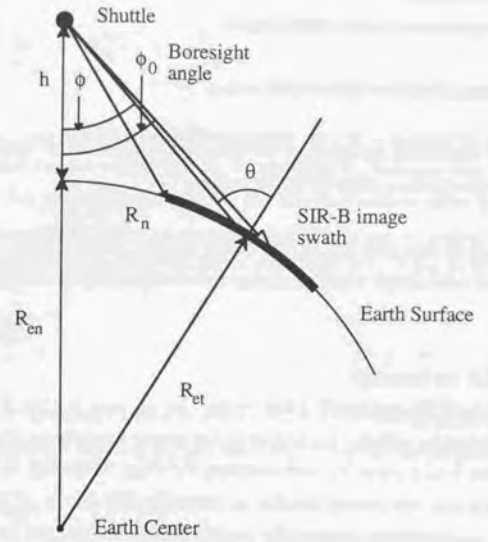

Fig. 4-2. Coordinate system of SAR imaging, where R_{en} and R_{et} mean the earth radii at sub satellite point or scene center, respectively.

4.2.1 Accuracy requirements

We define the accuracy requirement for this theme below.

The antenna elevation pattern should be determined so that

i) the backscattering coefficient (γ) image of the flat and dense rainforest shows the across track constancy (from the near range to the far range);

ii) the variation should be less than 0.1 dB (including random and bias error : 1 sigma) to eliminate the across track stripe when mosaicing two contiguous path images.

4.2.2 Error criteria for an average

We consider the statistics of the averaged image power for an area A (See Fig. 4-1) and determine the measurement error criteria. Each pixel image power (correlation power) follows the $2N_L$-degree χ^2 function with a mean, P_C, and variance, P_C^2/N_{EL}, where N_{EL} is the effective number of looks (N_L and N_{EL} are almost similar as shown in Fig 2-11). If the area A is comparatively small, the error depends only on the number of the samples and its distribution function. As the area A increases, the error due to the P_C variation over A increases. Because P_C changes slightly in range and azimuth in area A, the variance of the image power, $\sigma_{C,A}^2$ contains the second moment of the P_C, σ_E^2, and the variance of image power for distributed components, $\sigma_{C,D}^2$:

$$\sigma_{C,A}^2 = \sigma_E^2 + \sigma_{C,D}^2 \tag{4.4}$$

$$\sigma_E^2 = \frac{1}{A}\iint_A (P_C(A) - \overline{P_C(A)})^2 dA \tag{4.5}$$

$$\overline{P_C(A)} = \frac{1}{A}\iint_A P_C(A) dA \tag{4.6}$$

Two adjacent pixels even in Amazon SAR image is not independent [13]. Therefore, we need thinning out the image by every D pixels, whose auto-correlation ρ_1 is less than 0.1 in range and azimuth directions. The resultant variance, $\sigma_{C,D}^2$, of the averaged image power over N D-spaced samples is given by (see Appendix 4-1):

$$\sigma_{C,D}^2 = \frac{1 + 2\rho_1 + 2\rho_2}{N_L \cdot N}\frac{P_C^2}{N_L} \tag{4.7}$$

where, ρ_2 is the auto-correlation in 2D distance. Differentiating (4.1) (neglecting the noise) and taking the root sum square of its expansion, we get the limitation to $\sigma_{C,A}^2$.

$$\sigma_{C,A}^2 \le P_C^2 \cdot \left\{ \left(\frac{\Delta\gamma}{\overline{\gamma}}\right)^2 + \left(\frac{2\Delta G}{\overline{G}}\right)^2 + \ldots\ldots \right\} \tag{4.8}$$

where, $\overline{G}$ and $\overline{\gamma}$ are the estimated antenna pattern and the estimated back scattering coefficient. We have ignored the deviations in P_t, λ, R, $\tan\theta$ and V_g, because they are much smaller than ΔG and $\Delta\gamma$. We ignore $\Delta\gamma$ further since the standard passive array antenna (like the SIR-B type antenna) covers less than 6 degrees of off-nadir-angle region and we have actually measured the constancy of γ over the Belize rain forest [13]. Thus, (4.8) can be simplified to:

$$\sigma_{C,A}^2 \le P_C^2 \cdot \left(\frac{2\Delta G}{\overline{G}}\right)^2 \tag{4.9}$$

The criterion for the antenna pattern error, ΔG, can be considered as the averaged root sum square of the difference between the estimated and measured antenna patterns:

$$G(\phi) = \overline{G}(\phi) + \Delta G \tag{4.10}$$

Referring to the error analysis for the SIR-C data (see [6]-[8]), we apply the following criterion:

$$\left|\frac{\Delta G}{\overline{G}}\right| = 0.3dB\ (3\ sigma) \tag{4.11}$$

Arranging (4.4), (4.7), and (4.9), we obtain an inequality (4.12). This inequality allows the selection of the area A and the number of the uncorrelated image data points, N, in meeting the antenna pattern measurement requirement (4.11).

$$\frac{\sigma_E^2}{P_C^2} + \frac{1 + 2\rho_1 + 2\rho_2}{N_L^2 \cdot N} \le \left(\frac{2\Delta G}{\overline{G}}\right)^2 \tag{4.12}$$

4.2.3 Number of data to be averaged

The left side of (4.12) consists of two types of variances. The first one is a continuous function of the location; the second one follows some distribution function and becomes smaller with averaging over large data. Many combinations of unknown parameters N and A should exist for (4.12). For simplicity, we assume that the total is shared equally by two terms. The error criteria for each of them is then:

$$\frac{\sigma_{\hat{\varepsilon}}}{P_C} \le 0.142\ dB \tag{4.13}$$

$$\sqrt{\frac{1+2\rho_1+2\rho_2}{N_L^2 \cdot N}} \le 0.142\ dB \tag{4.14}$$

We use N_{min} as the minimum number of data points which satisfies (4.14) and may rearrange (4.14) to describe this condition:

$$N_{min} = \frac{1+2\rho_1+2\rho_2}{N_L^2 \cdot \left(10^{0.0142}-1\right)^2} \tag{4.15}$$

4.3 Screening Process for the Distributed Targets

To obtain the antenna pattern from SAR images of distributed targets, the distributed targets should behave uniformly in their backscattering characteristics (i.e., the scattering coefficient should be independent of incidence angle or vary in a known fashion). Here, we use the word "uniformly" with the meaning that every datum in some specific area distributes under the same specific distribution function. The Amazon rain forest generally satisfies this requirement because the rain forest scatters the radar signal by the mechanism of volume scattering [1].

Some images archived in the JPL Radar Data Center show that the Amazon area appears uniform visually. Four Amazon data sets from SIR-B, designated Brazil-1, Brazil-2, Brazil-3 and Colombia, and a Sumatra data set may probably satisfy the requirement of uniformity. Looking at the pictures carefully, however, we see some dark areas filled with rivers and some high-intensity areas visible. In Fig. 4-3, we show pictures of the Canadian forest, and Colombia images used in the study.

Removing the nonuniform intensity areas in the images may increase the credibility of the evaluation results. The first thing to do is thus to identify all these small nonuniform areas and eliminate them from consideration. For this task, a similarity test has been applied. As shown in [B] of Fig. 4-1, a whole image is divided into many small rectangular areas (Cells), each of which has N_{az} pixels in the azimuth and N_{rg} pixels in the range direction. A Cell is designated as $Cell^{i,j}$, where i stands for the stripe number and j for the column number. After we specify the size of the Cell properly within the error criterion, we can eliminate all the non-uniform Cells by using a screening process, which is based on the chi-square test.

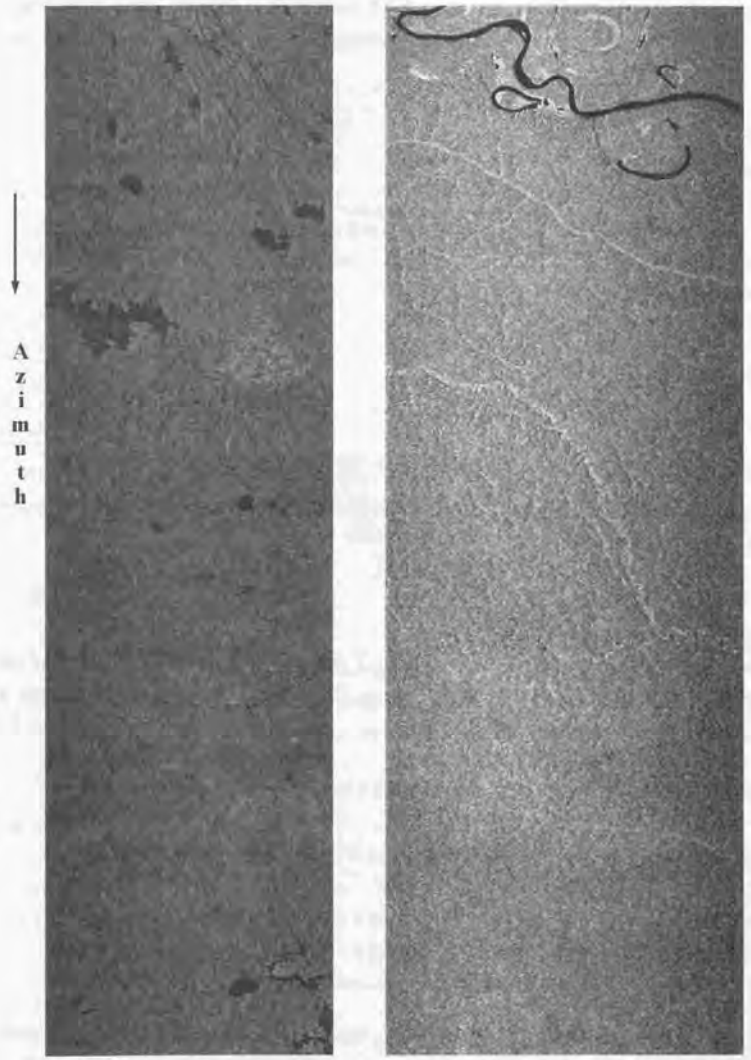

a) Canada b) Colombia

Fig. 4-3. a) Canadian forest image, b) Colombia image.

4.3.1 Similarity check by Chi-square test

The similarity test is based on the chi-square test, which asks "Are these two distributions different?"([10], [11]). Supposing that $C_l^{i,j}$ and $\mathbf{C}_l^i$ are the measured histograms at the l^{th} bin of $Cell^{i,j}$ and i^{th} stripe area, the following chi-square parameter χ^2 can be used to evaluate this problem:

$$\chi^2 = \sum_{l=1}^{N} \frac{(C_l^{i,j} - \mathbf{C}_l^i)^2}{C_l^{i,j} + \mathbf{C}_l^i} \tag{4.16}$$

The accumulated chi-square distribution function defined in (4.17) with r degrees of freedom and the gamma function $\Gamma()$ give the criterion X_α, under which statistical value χ^2 exists with the confidence of α% ([11]):

$$Q(\chi^2 \le X_\alpha \mid r) = \int_0^{X_\alpha} \frac{1}{\Gamma(\frac{r}{2}) \cdot 2^{\frac{r}{2}}} \cdot w^{\frac{r}{2}-1} \cdot e^{-\frac{w}{2}} dw \tag{4.17}$$

If a χ^2 is less than or equal to the value X_α with α% confidence, we can say, "These two distribution functions are not different." Hereafter, four values of (95, 97.5, 99, and 100%) are used for the levels of confidence.

4.3.2 Determination of N_{rg}

We consider σ_E^2. In a Cell, P_C depends only on R, then, integrations in (4.5) and (4.6) are simplified to one-dimensional ones. Using the first order Taylor expansion of $P_C(R)$ around the center of the strip, where $R = R_0$, σ_E^2/P_C^2 is approximated by:

$$\frac{\sigma_E^2}{P_C^2} = \frac{1}{P_C^2 \cdot L_{rg}} \int_{-L_{rg}/2}^{L_{rg}/2} \left(\left. \frac{\partial P_C(R)}{\partial R} \right|_{R=R_0} \right)^2 R^2 dR$$

$$= \frac{1}{P_C^2} \left(\left. \frac{\partial P_C(R)}{\partial R} \right|_{R=R_0} \right)^2 \frac{L_{rg}^2}{12} \tag{4.18}$$

$$L_{rg} = N_{rg} \cdot \frac{C}{f_{sample}} \tag{4.19}$$

where C is the speed of light, f_{sample} the sampling frequency, and L_{rg} the width of the Cell in the range direction. A calculation has been conducted simulating the Brazil case with a boresight angle of 34.7 degree and the published antenna pattern model [3] has been used. Fig. 4-4 shows the dependency of σ_E/P_C on the stripe location, R_0, with the parameter of N_{rg},

which takes values 5, 10, 20, and 40. At the near edge, N_{rg} of 40 almost meets the limitation requirement of 0.14 dB. However, we pick 20 for N_{rg} to obtain better results.

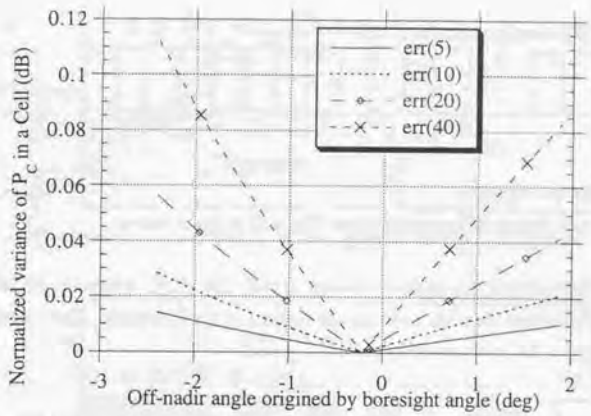

Fig. 4-4. Simulation of $10*\log_{10}(1+\sigma_E/P_C)$ for Brazil-1 using representative parameters of SIR-B, where the edges of the image swath have higher values even controlled less than 0.14 dB.

4.3.3 Determination of N_{az} and I_a

Regarding the azimuth sizes of the Cell (N_{az}) and entire image (I_a), we set the following conditions:

i) The number of sub-samples to obtain the averaged image power should be more than N_{min} (4.15).

ii) The stripes, whose similar Cells are more than a half, are considered appropriate to produce the averaged image power.

iii) A priori, a ratio of I_a and N_{az} (N_{raz}) is set to 16 because the following screening results can be easily handled on the computer monitor and paper. This means the whole image is 16 fold in azimuth for the evaluation. Conditions i) and ii) place the following requirement on N_{az}:

$$\frac{N_{raz}}{2} \cdot \left[\frac{N_{az}}{D} \right] \cdot \left[\frac{N_{rg}}{D} \right] \ge N_{min} \tag{4.20}$$

where, [] means the Gauss notation. This gives the requirement for N_{az} :

$$N_{az} \geq (\frac{2 \cdot N_{min}}{N_{raz}} \cdot \left[\frac{N_{rg}}{D}\right]^{-1} + 1) \cdot D \qquad (4.21)$$

Once N_{az} is obtained, I_a is simply given by:

$$I_a = N_{raz} \cdot N_{az} \qquad (4.22)$$

4.3.4 Similarity test procedure

There are 16 Cells in each stripe. The procedure (see Fig. 4-5) is given below:

i) Calculate the histogram of the image intensities in each Cell ($C_l^{i,j}$), where i is the stripe number, j the column number in azimuth, and l the bin number of the histogram. The reference histogram for the i^{th} stripe, $\mathbf{C}_l^i$, is obtained by :

$$\mathbf{C}_l^i = \frac{1}{16}\sum_{j=1}^{16} C_l^{i,j} \qquad (4.23)$$

ii) Obtain χ^2 by (4.16) between $Cell^{i,j}$ and the i^{th} reference.

iii) If χ^2 is less than **Q** which is calculated with a given confidence level, the $Cell^{i,j}$ is similar to the majority of cells in the i^{th} stripe.

iv) If there are more than eight similar Cells, the averaged image power and additional physical parameters are calculated only using the similar Cells. If not, the stripe is discarded.

v) This procedure is repeated over the full swath.

Applying this screening process to the Colombia image shown in Fig. 4-3-b, we find that the algorithm successfully picks out the non-uniform points visibly, such as the river running across the swath on the right-hand side. 5% of the data Cells in the Colombia image are rejected as non-uniform. We found little difference among the results using 95, 97.5, and 99% confidence levels, so we adopted 99% as the confidence level for the similarity test.

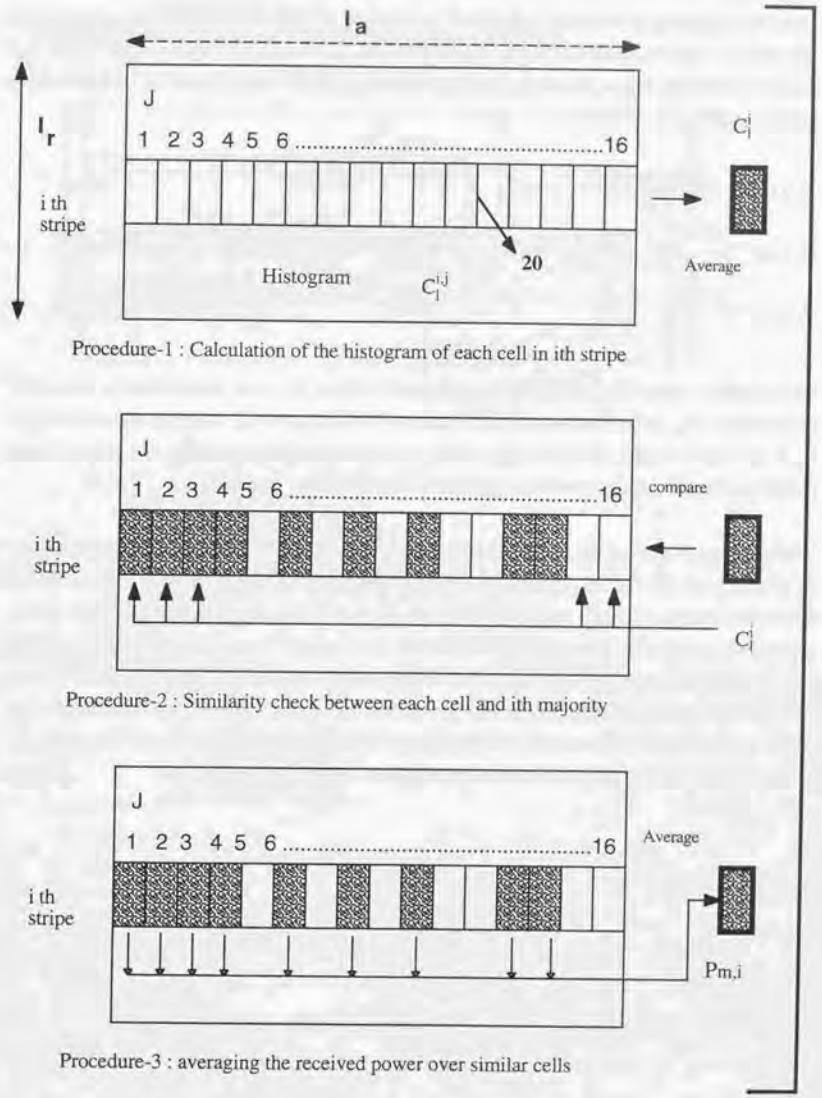

Fig. 4-5. Screening procedure for each stripe's data in azimuth.

4.4 SAR Correlation Power Model for Each Stripe

Once the screening processing is finished, each stripe is represented by several geophysical parameters, such as incidence angle, off-nadir angle, and averaged image power. Here, the expectation of the image power, $P_{C,i}(m,\mathbf{u})$, is derived for the i^{th} stripe based on (4.1) and SAR geometry (Figs 4-2 and 4-6).

$$P_{C,i}(m,\mathbf{u}) = \frac{g_m^2(\phi_i \mid \mathbf{u})\cot\theta_i}{R_i^2} + B \cdot R_i \tag{4.24}$$

$$\phi_i = \cos^{-1}\{\frac{(h+R_{en})^2 + (R_n + N_{rg}\cdot C\cdot(i+0.5)/f_{sample})^2 - R_{et}^2}{2\cdot(h+R_{en})\cdot(R_n + N_{rg}\cdot C\cdot(i+0.5)/f_{sample})}\} \tag{4.25}$$

$$\theta_i = \sin^{-1}\{\frac{(h+R_{en})\cdot\sin\phi_i}{R_{et}}\} \tag{4.26}$$

where suffix i means the quantity at the center of i^{th} stripe; R_{et} is the Earth radius at the center of the image; R_{en} is the Earth radius at the nadir of the SAR (see Fig. 4-6); h is the orbit height; R_n is the slant range to the near edge of the whole image; B is the unknown constant; and $g_m(\phi_i|\mathbf{u})$ is the m^{th} antenna pattern model with characterization vector, $\mathbf{u}$.

While the expectation of the image power is formulated by several SAR processing parameters as shown in (4.1) - (4.3a), most of them are constants, regardless of their determination difficulty, except off-nadir angle, boresight angle and antenna pattern. Even if all of the processing parameters are carefully determined in a straight forward manner using orbital information and geophysical parameters, the absolute calibration of the SIR-B image should be qualified by using a more reliable source for calibration, such as corner reflectors. The image power model (4.24) is then formed by $g_m(\phi_i|\mathbf{u})$, which corresponds to the relative antenna pattern $G(\mathbf{u})$ multiplied by an unknown constant, and terms varying with R.

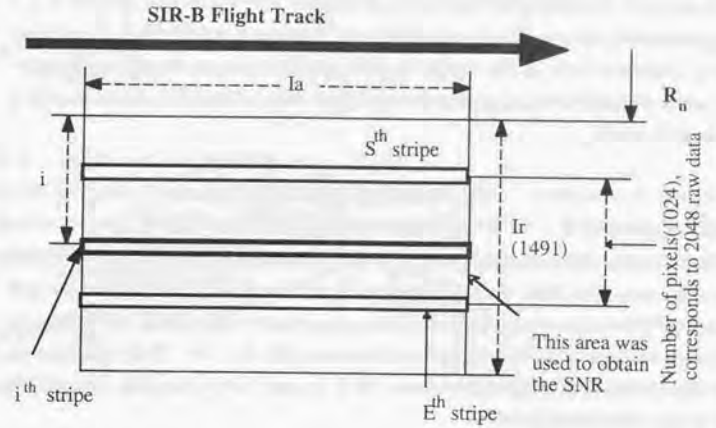

Fig. 4-6. Image coordinate system including the strip number

4.4.1 Antenna pattern Model

We will compare three types of antenna pattern models:

Model A

$$g_1(\phi \mid \mathbf{u}) = 10^{0.1\{a\cdot(\phi-\phi_0)^2 + b\}} \tag{4.27}$$

$$\mathbf{u} = \{\phi_0, a, b\} \tag{4.27a}$$

Model B

$$g_2(\phi \mid \mathbf{u}) = 10^{0.1\{a\cdot(\phi-\phi_0)^2 + b + c\cdot(\phi-\phi_0)^4\}} \tag{4.28}$$

$$\mathbf{u} = \{\phi_0, a, b, c\} \tag{4.28a}$$

Model C

$$g_3(\phi \mid \mathbf{u}) = d\left\{\sin c(\frac{\pi L_R \sin(\phi-\phi_0)}{\lambda}) + \sin c(\frac{\pi L_R \sin(\phi+\phi_0)}{\lambda})\right\}^2 \cos(\phi-\phi_0) \tag{4.29}$$

$$\mathbf{u} = \{\phi_0, d, e, L_R\} \tag{4.29a}$$

where a, b, c, L_R, and e are the unknown parameters, and ϕ_0 the boresight angle of the antenna.

Model A is similar to that used in reference [1]. Model C is a fit to the ground-based (preflight) antenna pattern for SIR-B, as measured by the antenna manufacturers, Ball Aerospace, of Denver, Colorado. The Model C curve was used in the SIR-B image correlator, with e and L_R

fixed at 0.3π and 2.16, for radiometric correction of standard SIR-B products. Model B is a fourth order polynomial, which gives a greater degree of freedom in the antenna pattern shape than Model A. A simple Taylor series expansion of the pre-flight pattern Model C reveals that fourth order terms are significant, suggesting that the higher order of Model B should provide a needed degree of freedom.

4.4.2 Determination of B

Unless we subtract noise component from image power, the estimated antenna pattern will be broader than the actual. The SNR, which is listed in the processing parameter file or obtained by 2048-sample FFT based power spectrum for 756 contiguous raw data points, can be used to estimate the noise component in the image power or directly *BR* of (4.24). Although *B* can be estimated in the maximum likelihood estimation, MLE, routine, its convergence accuracy is degraded. *B* is then determined as below.

$P_{total}(\boldsymbol{u})$, the integration of the image power model over the area where the signal-to-noise ratio was estimated, is determined as follows :

$$P_{total}(\mathbf{u}) = \sum_{i=S}^{E} \int_{R_{n,i}}^{R_{f,i}} \{\frac{g_m^2(\phi \mid \mathbf{u})\cot\theta}{R^2} + B \cdot R\} dR \tag{4.30}$$

where S is the start stripe in the integration area (see Fig. 4-6); E is the end stripe in the integration area; $R_{f,i}$ and $R_{n,i}$ are the slant ranges to far and near edges of i^{th} stripe; and **u** is the unknown parameters (4.27a, 4.28a, 4.29a). Introducing $P_{int}(\mathbf{u})$ for the integration of the first term of the right hand side of (4.30), and the SNR for this integration area, $P_{total}(\boldsymbol{u})$ is expressed in three ways.

$$P_{total}(\mathbf{u}) = P_{int}(\mathbf{u}) + \sum_{i=S}^{E} \frac{B}{2}(R_{f,i}{}^2 - R_{n,i}{}^2) \tag{4.31a}$$

$$= P_{int}(\mathbf{u}) \cdot (1 + \frac{1}{SNR}) \tag{4.31b}$$

$$= \sum_{i=S}^{E} \overline{P}_i \cdot \Delta R \tag{4.31c}$$

where $\overline{P}_i$ is the averaged image power for the screened i^{th} stripe, and ΔR is the range spacing, C/f_{sample}. Deleting $P_{int}(\mathbf{u})$ from (4.31a) and (4.31b), *B* is given as;

$$B = \frac{2 \cdot \sum_{i=S}^{E} \overline{P}_i \cdot \Delta R}{(SNR+1)\sum_{i=S}^{E}(R_{f,i}{}^2 - R_{n,i}{}^2)} \tag{4.32}$$

4.5 MLE and Its Solution

In the final step, the maximum likelihood estimation (MLE) method determines the antenna pattern models. The following chi-square parameter $[\chi_m{}^2(\mathbf{u})]$ is defined as the likelihood of the parameter estimation for the m^{th} model.

$$\chi_m^2(\mathbf{u}) = \sum_{i=S}^{E} \frac{[\overline{P}_i - P_{C,i}(m,\mathbf{u})]^2}{\sigma_i^2} \tag{4.33}$$

$$\sigma_i^2 = \sigma_E^2 + \frac{1 + 2\rho_1 + 2\rho_2}{N_L \cdot N_i} \cdot \left(\overline{P}_i\right)^2 \cdot \left(R_{A,i} - 1\right) \tag{4.34}$$

where $\sigma_i{}^2$ is the variance of the image power of the i^{th} stripe; N_i is the number of samples for the averaged image power of the i^{th} stripe; $R_{A,i}$ is the ratio of variance to the square of average for image power in the i^{th} stripe. The solution of the MLE problem, **u**, which minimizes (4.33) is given by the L^{th} order simultaneous nonlinear equations by differentiating (4.33) with respect to **u** and its arrangement.

$$\sum_{i=S}^{E} \frac{\overline{P}_i - P_{C,i}(m,\mathbf{u})}{\sigma_i^2} \frac{\partial P_{C,i}(m,\mathbf{u})}{\partial u_k} = \mathbf{0} \qquad \text{k=1,2,3,...L} \tag{4.35}$$

Replacement of **u** by $\mathbf{u}+\Delta\mathbf{u}$ and its expansion around **u** simplifies (4.35).

$$M_k^l \cdot \Delta u_l = N_k \tag{4.36}$$

where

$$M_k^l = \sum_{i=S}^{E} [\frac{\{\overline{P}_i - P_{C,i}(m,\mathbf{u})\}}{\sigma_i^2} \cdot \frac{\partial^2 P_{C,i}(m,\mathbf{u})}{\partial u_k \cdot \partial u_l} - \frac{\partial P_{C,i}(m,\mathbf{u})}{\partial u_k} \cdot \frac{\partial P_{C,i}(m,\mathbf{u})}{\partial u_l}]$$

$$N_k = -\sum_{i=S}^{E} [\frac{\{\overline{P}_i - P_{C,i}(m,\mathbf{u})\}}{\sigma_i^2} \cdot \frac{\partial P_{C,i}(m,\mathbf{u})}{\partial u_k}]$$

Applying the Levenberg-Marquardt method [10] to the above equations, only first order derivatives are necessary to give good convergence .

4.6 A case Study for the High Dynamic Range SAR :SIR-B

We applied the above method to determine the inflight SIR-B antenna elevation pattern. We have selected the SIR-B as a representative SAR because of high dynamic range and simple radiometric scheme. The evaluated images are selected from the Amazon, Colombia, Sumatra, Canada, and Illinois farm lands as listed in Table 4-1.

Table 4-1. Characteristics of evaluated images

a) Summary of image data used

Number of scenes evaluated	8
Image data type	slant range correlated image/ not radiometric converted
Contents of data	amplitude
Number of bits per pixel	8 (0 - 255)
Number of looks	4
Pixel spacing in range/azimuth	9.88/9(m)

b) Summary of image data used (cont.)

Area	Brazil-1	Colombia	Brazil-2	Illinois-1
Data take[1]	118.30	118.30	118.30	070.10
Scene center	-4,17.4	3,22.0	-4,48.1	38,12.2
(lat., lon.)[2]	-64,35.1	-68,54.8	-64,17.4	-88,23.5
Incidence angle[3]	35.6	36.6	35.6	49.0
Altitude (km)	222.41	222.14	222.46	231.92
SNR (dB)	9.22	9.28	9.22	4.48
Record length[4]	4352	4352	4352	4608
Number of records[4]	1491	1491	1491	1441
Area	Illinois-2	Brazil-3	Canada	Sumatra
Data take	97.20	118.30	053.20	086.60
Scene center	40,16.8	-3,36.3	55,51.8	-2,49.6
(lat., lon.)[2]	-90,56.6	64,58.9	-100,5.0	103,12.2
incidence angle[3]	30.4	34.6	33.7	44.5
Altitude (km)	229.04	222.37	237.79	222.79
SNR (dB)	10.9	8.9	7.8	6.2
Record length[4]	4608	4352	4352	4096
Number of records[4]	1492	1491	1202	1697

remark)

1) All these data were kindly supplied from SAR Data Catalogue Center in Jet Propulsion Laboratory. Data take is a unique number assigned for each SIR-B operation duration.
2) lat. and lon. are the abbreviation of latitude and longitude in units of deg. and min.
3) Defined at the center of the image.
4) Unit is Byte

In Table 4-2, we show ρ_1, ρ_2, and N_{min} values estimated from each of the eight scenes analyzed in this study. From this, we see that the worst case is for the Illinois farm land scene. Here the correlation is significant out to 10 pixels, so a large number of pixels must be used in averaging. I_a (N_{az}) is calculated to be less than 928 (58), except for Illinois images. Most of the images can satisfy these conditions.

Table 4-2. N_{min}, N_{az}, and I_a

Scene	ρ_1	ρ_2	N_{min}	D	N_{rg}	I_a	N_{az}
Brazil-1	0.08	0.03	316	3	20	368	23
Colombia	0.10	0.05	337	3	20	400	25
Brazil-2	0.06	0.03	306	3	20	368	23
Illinois-1	0.17	0.09	394	10	20	4112	257
Illinois-2	0.18	0.07	389	10	20	4064	254
Brazil-3	0.13	0.07	363	3	20	416	26
Canada	0.10	0.05	337	5	20	928	58
Sumatra	0.06	0.02	301	3	20	352	22

*) N_{min}, D are in pixels. Effective look number N_L is 3.5.

Table 4-3 shows the coefficient B for all the evaluated scenes. The estimation of the noise level in each SAR image is very important for obtaining more accurate values for the antenna 3dB or 1.5 dB beam width.

Table 4-3. Coefficient B

Scene_ID	Scene_name	B	SNR(dB)
0	Brazil-1	1.45	9.2
1	Colombia	1.56	9.3
2	Brazil-2	1.47	9.2
3	Illinois	0.42	4.5
4	Illinois-2	0.49	8.9
5	Brazil-3	1.56	10.9
6	Canada	0.38	7.8
7	Sumatra	1.36	6.2

4.6.1 Results

In total, 96 combinations (8 scenes, 3 models, 4 confidence levels) have been examined to determine evaluate i) which confidence level to use, ii) which antenna pattern model, and iii) the best scene. The residual error (RE) has been selected as the parameter to evaluate whether the result is good or not.

$$RE = \sqrt{\overline{x^2} - \bar{x}^2}$$

$$\overline{x^2} = \frac{1}{N}\sum_{i=1}^{N}\{10\cdot\log_{10}\overline{P_i} - 10\cdot\log_{10}P_{C,i}(m,\mathbf{u})\}^2$$

$$\bar{x} = \frac{1}{N}\sum_{i=1}^{N}\{10\cdot\log_{10}\overline{P_i} - 10\cdot\log_{10}P_{C,i}(m,\mathbf{u})\} \qquad (4.37)$$

4.6.2 Confidence level

Figs 4-7-a and 4-7-b show typical relationships between the residual errors and the confidence levels used in the screening process. In Fig. 4-7-a, which corresponds to the Canada scene of

Fig. 4-3-a, the residual error tends to increase with confidence levels. Fig. 4-7-b for Colombia scene pictured in Fig. 4-3-b exhibits almost the same tendency as the Canada scene in that the first three confidence levels yield almost the same residual errors while the 100% confidence level yields worse residual errors. 99% level is adopted as the confidence level for the rest of this study since it maximizes the number of points used in the calculations and gives results similar to those of the 95% and 97% levels.

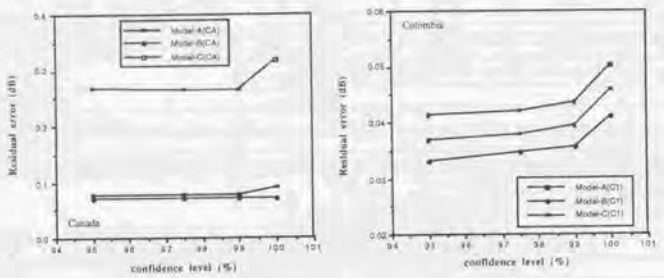

Fig. 4-7. Residual error dependency on confidence levels in Canada (a) and Colombia (b) scenes.

4.6.3 Antenna pattern model

From Figs 4-7-a and 4-7-b, we see that Model B produces a smaller residual error than Model A or C. This is generally the case for the other six scenes analyzed. Through the estimation, Model C seems to be too sensitive to archive good convergence of the solution, partially because of the larger number of parameters to be estimated. Furthermore the solutions depend on the initial values set, especially the boresight angle, ϕ_0. Except for the boresight angle estimation, these three models can be easily fitted to the data. Two different methods have been tried to evaluate the accuracies of the MLE estimations following convergence of the models in terms of boresight angle initialization: Case A in which the boresight angle used in the image correlation (listed in the image header) is assigned and Case B in which the estimated boresight angle is obtained by using Model B and which gives the smallest residual error is assigned. Using Case A, errors of estimation have been found to increase in the order of Model B, A and C (as shown in Fig. 4-7-a). However, using Case B, Model A is found to have a worse error than the other two models (see Fig. 4-7-b). The effect of the error in boresight angle on SIR-B was previously noted in [3]. Based on these results, Model B has been selected as the best model for the rest of the study.

4.6.4 Best image data

For each of the images used in the study, Figs 4-8-a to -h show how the screened data have been fitted to the best model (Model B). Fig. 4-9 shows the residual error distribution for the best fit over the images tested.

As seen in Fig. 4-9, the smallest residual error occurs for the Brazil-1 scene. This is mainly because there are very few nonuniform intensity patterns within that scene. It can be seen from Fig. 4-8-a how well the model fits the data for this case. The Colombia data gives the second smallest residual error in the rain forest data set. From Fig. 4-8-b, we can see that the errors are slightly larger than in Fig. 4-8-a around the peak of the antenna pattern.

The worst fit is to the Illinois-1 data shown in Fig. 4-8-d. Even though the data are screened, there is still a wide spread around the fitted curve. The Illinois-2 scene contains similar types of scatterers (mixed agricultural fields), yet has a much smaller residual error. We believe there are two explanations for this: First, the Illinois-1 scene only covers about 2° of the elevation pattern (roughly one-third), whereas the Illinois-2 scene covers about 5°, which gives a better chance of a good fit. Second, the Illinois-1 scene has an SNR of only 4.5 dB, whereas the Illinois-2 scene has an SNR of 10.9 dB. This again gives a greater chance of a good fit for the Illinois-2 data.

The Brazil-3 scene includes a large river in part of the image. This is successfully eliminated by the screening process, as evidenced by the gap in the screened data, seen in Fig. 4-8-f. The Canadian forest data is located in the northern part of the Canada. The screened data are well fitted to the estimated antenna pattern, except for a few points near the edge and peak area. The final figure shown is from the Sumatra rain forest (Fig. 4-8-h). Due to the large boresight angle and the constraints on the SIR-B swath width, the antenna pattern covers only 3° of the off-nadir angle width. This data gives a fairly small residual error of 0.04 dB. From the above results, we select Brazil-1 as our best image data for the rest of the study.

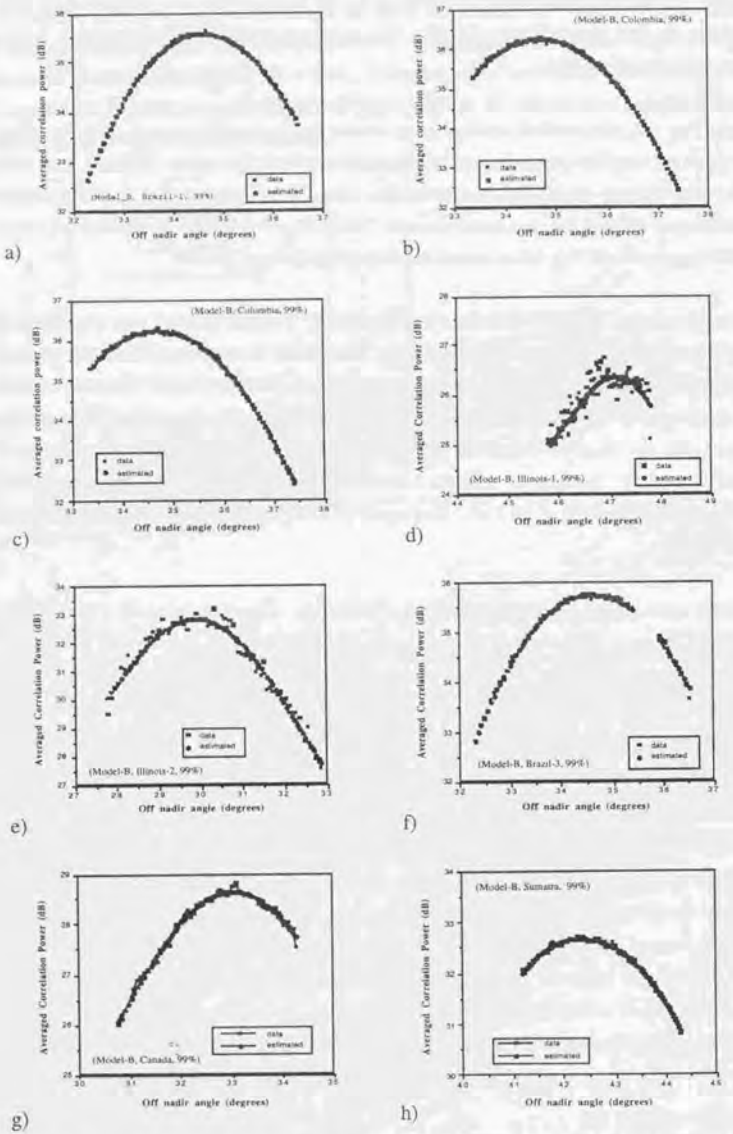

Fig. 4-8. Data fitting for Brazil-1, Colombia-1, Brazil-2, Illinois-1, Illinois-2, Brazil-3, Canada, and Sumatra Scenes by Model B with 99% confidence.

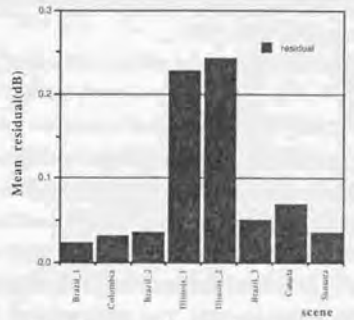

Fig. 4-9. Mean residual distribution over eight evaluated scenes.

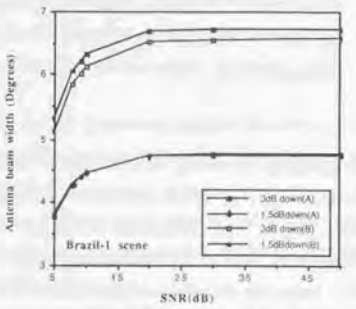

Fig. 4-10. Relationship between Antenna beam width and SNR of the image data, where two lines are so close for 1.5 dB width.

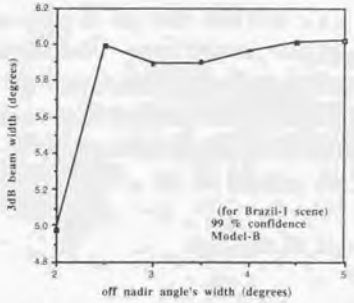

Fig. 4-11. Estimated Beam width and data window width used for Brazil-1.

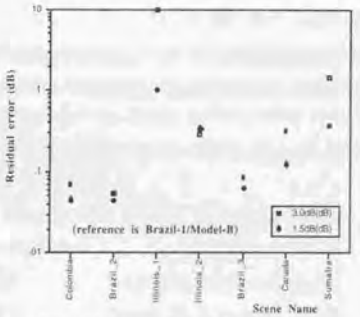

Fig. 4-12. Repeatability of the evaluation in terms of the residual error.

4.6.5 Effect of noise reduction

A simulation has been conducted to evaluate the effect of SNR on antenna beam width using the screened Brazil-1 data with 99% confidence, Model A, and Model B. In the simulation, SNR has been assumed between 5 and 50 dB, then the related noise has been subtracted. Thus, in Fig. 4-10, the beam width corresponding to an SNR of 9dB should be correct if the SNR is indeed 9 dB. The beam width corresponding to 50 dB of SNR is the same as the measurement which would result if no noise reduction are performed.

As shown in Fig. 4-10 :

i) Model B with no noise reduction gives 6.5° as the 3 dB beam width. This is 0.5° bigger than the result obtained when noise reduction is performed, assuming that the SNR is the same as that given in the image header, approximately 9dB.

ii) Using Model A without noise correction appears to give similar results to those in [1].

4.6.6 Relation between the antenna beam width and off-nadir angle's width

As shown in Fig 4-8, SIR-B data cover the off-nadir angles from 2° to 5°, depending on the boresight angle. The estimation accuracy of MLE depends on the type of the unknown function, the number of data points accommodated, and how wide the off-nadir angles are. Fig. 4-11 indicates the relation between the 3 dB beam width and the off-nadir angle's width using Model B on Brazil-1 data screened at the 99% confidence level. This figure indicates that if the off-nadir angle width is less than 2.5°, the estimated 3 dB beam width is smaller than the true.

4.6.7 Repeatability of the antenna pattern fit

The optimum antenna pattern results are summarized below.

$$10 \cdot \log_{10} g_2(\phi \mid \phi_0, a, b, c) = a \cdot (\phi - \phi_0)^2 + b + c \cdot (\phi - \phi_0)^4 \qquad (4.38)$$

a, b, c	-0.286, 41.203, -0.00487
residual error	0.024 dB
ϕ_0, ϕ	boresight angle, off nadir angle
Beam width (3 dB down)	6.0°
Beam width (1.5 dB down)	4.4°

We calculate the RMS error between two antenna patterns, one of which is the target and the other of which is the reference defined in (4.38), and we call this repeatability. This error is defined as the standard deviation between two antenna patterns including residual errors, as follows:

$$RMS\ error = \sqrt{\overline{\Delta G_{ref}^2} + \overline{\Delta G_{target}^2} + (\overline{G_{ref}} - \overline{G_{target}})^2} \qquad (4.39)$$

where ΔG_{ref} is the residual error of reference antenna pattern, ΔG_{target} the residual error of the target scene, $\overline{G_{ref}}$ the antenna pattern model for the reference, and $\overline{G_{target}}$ the antenna pattern model derived from the target $\overline{G_{ref}}$ and $\overline{G_{target}}$ are calculated at the 3dB and 1.5 dB down points and correspond to the RMS errors shown in Fig. 4-12. Between the Amazon scenes, the RMS error is less than 0.08 dB at the 3dB down points. This error increases to 0.3 dB for the

Canadian forest image and is worse than 1dB for the Sumatra and Illinois-1 images, both of which have poor SNRs.

4.6.8 Comparison

Table 4-4 compares results of this study with previous SIR-B antenna pattern estimates. From this, it seems that our result is 0.7° smaller than that of Ball aerospace and 0.9° smaller Moore's result. The possible reasons for the difference of 0.9° are:

(1) *The model for the antenna pattern* The best fitted antenna model is confirmed as the fourth order power model. If a second order model is used instead, the lack of freedom gives a 0.2° wider estimation in the 3 dB width result.

(2) *Noise reduction* Noise increases the total power in the image. The image with noise also gives a 0.5° wider estimation.

The combination of reasons (1) and (2) may explain why Moore's result is bigger than ours because some of the same data were used. However, the reason the Ball Aerospace measurement is 0.7° bigger than our result and the model used in the SIR-B processor is not clear. Fig. 4-13 shows the angular dependence of the three antenna patterns in comparison with Model-B. This shows that the Moore's pattern and the Ball's pattern differ from the Model-B more than 0.3 to 0.5 dB and may cause stripes between two neighbor images' border.

Table 4-4. Summary of the antenna pattern width

Item	1.5 dB beam width (deg)	3.0 dB beam width (deg)
This study	4.4°	6.0°
Ball data	4.8°	6.7°
JPL	4.2°	5.9°
Moore	5.0°	6.9°

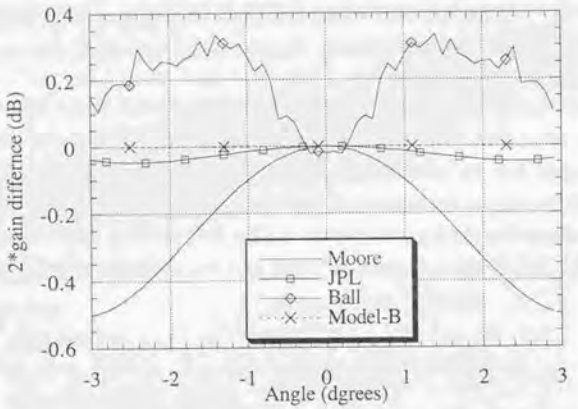

Fig. 4-13 Angular dependencies of the three antenna patterns in comparison with Model-B. Twice the difference is shown on the vertical axis because of the direct relationship with γ.

4.7 Conclusions

This chapter has showed a method of obtaining the antenna pattern of an in-orbit SAR instrument based on correlated SAR images obtained mainly over the Amazon rain forest. Using this result, the SIR-B antenna pattern has been estimated to have the 3 dB beam width of 6.0°. The conclusions about this methodology and about the parameters to be selected for its use are as follows:

(1) **Area of interest** The Amazon rain forest is a very good target because of its uniformity.

(2) **Signal-to-Noise ratio** Choose an image with a good SNR.

(3) **Noise reduction** Noise reduction for the SAR image is necessary to ensure a properly estimated antenna pattern.

(4) **Antenna pattern model** The recommended antenna pattern model is Model B (fourth order polynomial) for SIR-B type antennas.

(5) **Boresight angle** It is necessary to select the boresight angle so that the widest range of off-nadir angles can be included in the image power pattern to obtain a better estimate by MLE.

(6) **Error criterion** The final results have shown that the antenna error (residual) is normally less than 0.08 dB for the Amazon data. The error criteria for the antenna pattern (0.3 dB as 3 sigma) is thus confirmed to be appropriate.

(7) **Repeatability** Over the Amazon, the antenna pattern estimate from one scene has been shown to be repeatable for others with less than 0.1 dB RMS error.

Appendix 4-1

Suppose that there are N data sets (X_i), each of which is governed by the same distribution function, $P(X_i)$, where i=1, 2,,,,, L.

(1) Each data set (Xi) is composed of M elements,

x_k, k=1, 2, ..., M (4A-1.1)

(2) The N data sets have the same variance, σ^2, where x_i is its mean, and suffix i stands for the i^{th} data set.

$$\sigma_i^2 = \overline{(x_i - \overline{x_i})^2} = \sigma^2 \,, i = 1,2,,,,,N \tag{4A-1.2}$$

(3) The correlation coefficient is symmetrical like the autocorrelation function.

$$\rho_{i,j} = \begin{cases} \rho_l & l = |i-j| \\ 1 & i = j \end{cases} \tag{4A-1.3}$$

$$\rho_{i,j} = \frac{\sigma_{i,j}^2}{\sigma_i \cdot \sigma_j} \tag{4A-1.4}$$

$$\sigma_{i,j}^2 = \overline{(x_i - \overline{x_i}) \cdot (x_j - \overline{x_j})} = \overline{x_i \cdot x_j} - \overline{x_i} \cdot \overline{x_j} \tag{4A-1.5}$$

The average over M data, z, and its variance, σ_z^2, is calculated as follows:

$$z = \overline{x_j} \tag{4A-1.6}$$

$$\begin{aligned} \sigma_z^2 &= \overline{z^2} - \overline{z}^2 \\ &= \frac{1}{N^2}\{(\sum_{i=1}^{N} \overline{x_i^2} + \sum_{i>j,i=2}^{N} 2\overline{x_i \cdot x_j}) - (\sum_{i=1}^{N} \overline{x_i}^2 + \sum_{i>j,i=2}^{N} 2\overline{x_i} \cdot \overline{x_j})\} \\ &= \frac{1}{N^2}\{\sum_{i=1}^{N} (\overline{x_i^2} - \overline{x_i}^2) + \sum_{i>j,i=2}^{N} 2(\overline{x_i \cdot x_j} - \overline{x_i} \cdot \overline{x_j})\} \\ &= \frac{1}{N^2}(\sum_{i=1}^{N} \sigma_i^2 + \sum_{i>j,i=2}^{N} 2\rho_{i,j} \cdot \sigma_i \cdot \sigma_j) \end{aligned} \tag{4A-1.7}$$

Using above relation, we have:

$$\sigma_z^2 = \frac{1}{N^2}(N\sigma^2 + 2N\overline{\rho}\sigma^2) = \frac{\sigma^2}{N}(1 + 2\overline{\rho}) \tag{4A-1.8}$$

where,

$$\overline{\rho} = \frac{1}{N} \sum_{i>j,i=2}^{N} \rho_{|i-j|} = \frac{1}{N} \sum_{l=1}^{N} (N-1)\rho_l \tag{4A-1.9}$$

The variance, σ_z^2, is then given by:

$$\sigma_z^2 = \frac{1 + 2\overline{\rho}}{N} \sigma^2 \tag{4A-1.10}$$

References

[1] R. K. Moore and M. Hemmat, "Determination of the vertical pattern of the SIR-B antenna," Int. J. Remote Sensing, vol.9, no.5, pp. 839-847, 1988.

[2] R. K. Moore, V. S. Westmoreland, D. Frank, and M. Hemmat, "Determining the vertical antenna pattern of a spaceborne SAR by observation of uniform targets," in Proc. IGARSS'86 symp.(Zurich, Switzerland), vol.1, pp. 469-472, 1986.

[3] M. C. Dobson, F. T. Ulaby, D. R. Brunfeldt, and D. N. Held, "External calibration of SIR-B imagery with area extended and point targets," IEEE Trans. Geosci. Remote Sensing, vol. 24, no.4, pp. 453-461, 1986.

[4] D. R. Brunfeldt and F. T. Ulaby, "Active Reflector for Radar Calibration," IEEE Trans. Geosci. Remote Sensing, vol. GE-22, no. 2, pp. 165-169, March 1984.

[5] R. K. Hawkins, "Determination of antenna elevation pattern for airborne SAR using the rough target approach," IEEE Trans. Geosci. Remote Sensing, vol. 28, no. 5, pp. 896- 905, Sept. 1990.

[6] A. Freeman, "SIR-C calibration plan: An Overview," JPL Report, JPL-D-6997, Feb. 1990.

[7] A. Freeman, "Spaceborne imaging RADAR-C/SIR-C ground calibration plan," JPL Report JPL-D-6999, Feb. 1990.

[8] J. D. Klein, "Spaceborne imaging RADAR-C/Engineering calibration Plan," JPL Report JPL-D-6998, Feb. 1990.

[9] J. B. Cimino, B. Holt and A. Richardson, "The shuttle imaging radar B (SIR-B) experiment report," JPL Publication 88-2, 1988.

[10] W. H. Press, B. P. Flannery, S. A. Teukolsky, and W. T. Vetterling, "Numerical recipes in C, The art of scientific Computing," Cambridge University Press, pp. 487-490, pp. 517-547, 1989.

[11] R. V. Hogg and A. T. Craig, "Introduction to mathematical statistics," Macmillan, 1978.

[12] A. Freeman and J. C. Curlander, "Radiometric correction and calibration of SAR images," Photogrammetric Engineering and Remote Sensing, vol. 55, no. 9, pp. 1295-1301, 1989.

[13] M. Shimada, and A. Freeman, "A Technique for Measurement of Spaceborne SAR Antenna Patterns Using Distributed Targets," IEEE Trans. Geosci. Remote Sensing, vol. 33, no. 1, pp. 100-114, Jan. 1995.

ANNEX 4 Small Dynamic Range Case : JERS-1 SAR

The JERS-1 SAR antenna elevation pattern has been measured using the method introduced in the main part of this chapter. The differences with the SIR-B case (dealt previously) are summarized in Table 4AN-1. The representative differences are: 1) SAR correlation power model is modified to fit the JERS-1 SAR receiving function, which contains two time-variant attenuators. 2) Error criteria is reconsidered including uncertainty of the Sensitivity Time Control (STC). The 17 Amazon SAR images have been analyzed to increase the credibility of the results.

Table 4AN-1. Procedure comparison between Chapter 4 and SAR

No.	Items described in Chapter 4	SAR
1	Error criteria	Almost same, but STC is included.
2	Amount of data to be averaged	Same
3	Screening processing	Same
4	N_{rg}, N_{az}, I_a	Same
5	Similarity test	Same
6	Correlation power model	Different
7	Antenna pattern model	Model B is adopted.
8	Determination of B	Same. Special consideration of SNR added.
9	MLE and solution	Same
10	Confidence level	99%
11	Image data	Amazon data is used.
12	Repeatability	Same

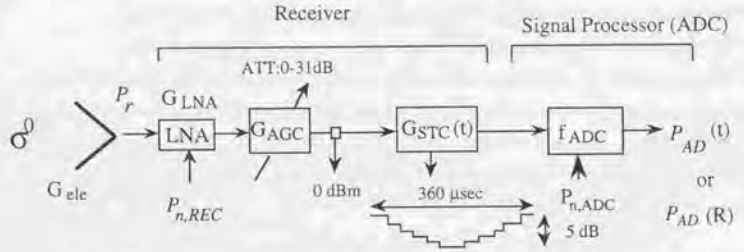

Fig. 4AN-1. SAR block diagram

A.4.1 SAR Correlation Power Model

A.4.1.1 Received signal power

The Automatic Gain Control (AGC) selects the receiver gain appropriately and maintains the signal power level almost 0 dBm regardless of the target intensity. The signal is then modulated by the STC to cancel the power intensity change due by AEP (see Fig. 4AN-1, [5], [6]). The raw data power (after AD conversion), $P_{AD}(R)$, is expressed as follows:

$$P_{AD} = \left(\frac{P_t G_0^2 G_{ele}^2 \lambda^2}{(4\pi)^3 R^3} \gamma \cdot \cos\theta \frac{C\tau}{2\sin\theta} \beta \cdot G_{LNA} + P_{n,REC} \right) \cdot G_{AGC} \cdot G_{STC} + P_{n,AD} \qquad (4AN\text{-}1)$$

where R is the slant range; G_{LNA} is the LNA gain; $P_{n,REC}$ is the noise power generated by LNA and receiver; G_{STC} is the STC gain; G_{AGC} is the AGC gain; $P_{n,AD}$ is the noise by ADC, which contains saturation and bit redundancy noises; G_0 is the antenna one-way peak gain; P_t is the transmission power; G_{ele} is the antenna relative elevation pattern; λ is the wavelength; γ is the backscattering coefficient; θ is the incidence angle; C is the speed of Light; and β is the azimuth antenna half width.

A.4.1.2 Correlation signal power

The SAR data consists of the signal scattered from the rain forest (distributed target) and the noise generated at the SAR receiver and signal processor. The correlation gain for those two components are almost the same (see. (3.56) with SCR = 1 in Chapter 3 and refer the Section 4.2 of this Chapter: General - SIR-B Antenna Pattern Measurement). The correlation power is given by the following [1]:

$$P_c(R) = A \cdot \frac{G_{ele}(R)^2 \cot\theta}{R^3} \cdot \overline{\sqrt{G_{STC}(R)}}^2 + R \cdot B(R) \qquad (4AN\text{-}2)$$

$$A = \frac{P_t G_0^2 \lambda^2 \gamma C \tau \beta G_{LNA}}{2(4\pi)^3} \cdot \overline{tf}_{sample} \frac{PRF \cdot \lambda}{2V_g \rho_{res}} \cdot G_{AGC} \qquad (4AN\text{-}3)$$

$$B(R) = \overline{tf}_{sample} \frac{PRF \cdot \lambda}{2V_g \rho_a} \cdot \left\{ P_{n,REC} \cdot \overline{\sqrt{G_{AGC}}}^2 \cdot \overline{\sqrt{G_{STC}(R)}}^2 + P_{n,AD} \right\} \qquad (4AN\text{-}4)$$

where f_{sample} is the sampling frequency; PRF is the pulse repetition frequency; V_g is the satellite's ground speed; ρ_a is the theoretical azimuth resolution; and τ is the pulse width. Because γ is assumed to be constant and $\overline{\sqrt{G_{STC}(R)}}$ the moving average of $\sqrt{G_{STC}(R)}$ over τ, compensates the relative antenna elevation pattern, the first term of the right side of (4AN-2) is proportional to R^{-2}. B(R) is complex over an observation window. We estimate the order of B(R) and its components using the Amazon data and onground data.

Fig. 4AN-2 shows two raw data (power) patterns. The upper curve (Curve 1) is typical Amazon data acquired for Grid Reference System, GRS, 395-306 on May 17, '92 (refer [9] for GRS). The lower curve (Curve 2) is receiver noise data which was acquired at factory before launch. The AGC levels are 4 dB for Amazon data and 0 dB for noise data. The AGC level is the attenuation applied to the maximum receiver gain. This means that as the target becomes brighter, the AGC level increases. Based on the error analysis ([2], [3], [8] and Fig. 3-6 of Chapter 3), the averaged A/D-conversion error is 0.45 dB when A/D output power distributes

between 5 and 10 dB. Therefore, the noise power included within Amazon data is almost constant of 0.45 dB. Therefore, we can assume that B(R) is almost constant over the imaging swath.

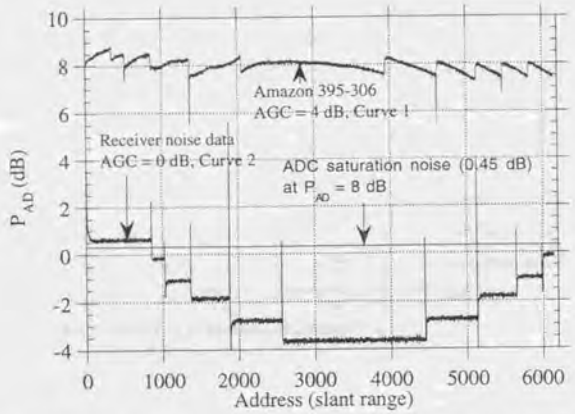

Fig. 4AN-2. Comparison of ADC noise and receiver noise. Big spikes in Curve 2 are due to the phase jumps at the attenuation changes. The phase difference between Curve 1 and Curve 2 is due to the difference in the STC start time.

Table 4AN-2. Summary of the images evaluated

No.	Path	Row	Acq.	SNR	B	$\sigma_{p,dB}$	ρ_1	ρ_2	N_{min}	N_{az}	I_a
1	395	305	5 17	4.2	0.046	3.3	0.13	0.11	403	69	1007
2	395	307	5 17	4.4	0.043	3.3	0.18	0.14	447	69	1118
3	395	308	5 17	4.4	0.048	3.3	0.11	0.08	376	69	940
4	395	309	5 17	4.8	0.046	3.6	0.05	0.04	394	69	987
5	395	311	5 17	5.3	0.049	3.6	0.15	0.11	482	69	1206
6	395	312	5 17	5.0	0.049	3.6	0.16	0.12	500	69	1249
7	395	314	5 17	5.7	0.053	3.6	0.15	0.12	489	69	1222
8	395	317	5 17	4.9	0.050	3.6	0.13	0.09	459	69	1147
9	395	318	5 17	4.9	0.057	3.6	0.13	0.12	481	69	1203
10	415	301	4 23	5.8	0.054	3.8	0.06	0.03	435	69	1089
11	415	304	4 23	5.7	0.055	3.8	0.12	0.09	518	69	1296
12	415	309	4 23	5.8	0.056	3.6	0.07	0.05	394	69	987
13	415	310	4 23	5.8	0.057	3.8	0.09	0.08	494	69	1235
14	415	311	4 23	5.8	0.059	3.8	0.13	0.09	521	69	1304
15	415	313	4 23	5.8	0.057	3.8	0.04	0.03	416	69	1042
16	415	317	4 23	5.8	0.056	3.8	0.09	0.06	481	69	1203
17	415	319	4 23	5.3	0.055	3.8	0.10	0.08	496	69	1241
				[dB]	x1016	[dB]					

where D = 5;
Acquisition year is 1992.

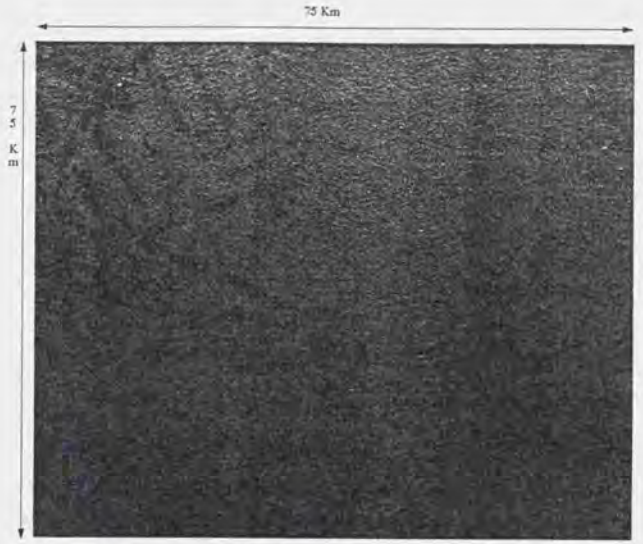

a)

b)

Fig. 4AN-3. a) Amazon SAR image acquired on May 17, 1992, GRS = 395-308, b) an example of screened Amazon SAR image with GRS = 395-308. Black area is recognized to be non similar and looks the same as the dark area in the above image.

A.4.2 Calculations

A.4.2.1 Images selection conditions

SAR data were acquired from the Amazon rain forests on April 23, '92 and May 17, '92. Each observation path collected 40 contiguous scenes during eight minutes activation. We have considered the following conditions to select the appropriate scenes.

(1) AGC should be constant over the whole scene.

JERS-1 SAR is always operated in the AGC mode, in which the appropriate receiver gain is selected every 64 pulses [5], [6]. When the receiver gain is changed (in AGC), a received power quickly changes accordingly, and the saturation rate may change depending on the balance of the target brightness. The correction of ADC saturation is not considered in the previous SAR correlation power model. Therefore, we should select the area observed with the same receiver gain.

(2) STC start time should not change in a scene.

The STC start time is controlled so that the SAR illumination area center can be at the antenna boresite direction, and the received signal can be with the best signal to noise ratio. Due to the fact that the Earth is not a sphere, the STC start time changes at least every 30 seconds and in 10 μsec steps, which corresponds to 1.5 Km in slant range. To simplify the calculation, the STC start time is required to be constant.

Seventeen of eighty Amazon scenes satisfying the above two conditions have been used for the calculation. Table 4AN-2 shows B, $\sigma_{p,dB}$, ρ_1, ρ_2 and N_{min} (minimum number of N) (See chapter 4). Generally, N_{min} is 460 for Amazon data, and α is 99% based on [4]. A sample screened result (Amazon 395-308) is shown in Fig. 4AN-3-b. Comparing it with the original image in Fig. 4AN-3-a confirms that the non-similar area (the black square) coincides with the vein like pattern at the left top of Fig. 4AN-3-a. This screening can be used to extract an similar intensity area. The calculation results are shown in Table 4AN-3.

Table 4AN-3. Summary of antenna patterns obtained from 17 Amazon images

No.	Path	Row	3dB width	Off nadir (deg)	Residual (dB)	Repeatability(dB)
1	395	305	5.5	34.75	0.08	0.15
2	395	307	5.5	34.75	0.10	0.15
3	395	308	5.6	34.69	0.09	0.20
4	395	309	5.6	34.71	0.09	0.23
5	395	311	5.4	34.78	0.13	0.16
6	395	312	5.5	34.68	0.18	0.22
7	395	314	5.4	34.97	0.11	0.18
8	395	317	5.3	34.90	0.11	0.21
9	395	318	5.4	34.85	0.13	0.17
10	415	301	5.5	35.02	0.06	0.13
11	415	304	5.9	34.98	0.06	0.42
12	415	309	5.6	34.87	0.11	0.21
13	415	310	5.3	35.02	0.11	0.17
14	415	311	5.3	35.07	0.09	0.23
15	415	313	5.2	35.07	0.08	0.27
16	415	317	5.4	35.05	0.10	0.15
17	415	319	5.2	35.22	0.12	0.33
average			5.4	34.91	0.10	0.21
standard dev			0.17	0.16	0.03	0.07

A.4.2.2 Error criteria for the averaged correlation power

The AEP error criteria, ΔG_{ele}, which is defined as the difference of the estimated AEP, $\overline{G_{ele}(\phi)}$ in dB and the measured AEP, $G_{ele}(\phi)$ in dB, are established below referring to SIR-C and SIR-B [7];

$$\left|\Delta G_{ele}\right| \le 0.3dB\,(3\ sigma) \tag{4AN-6}$$

After differentiating (4AN-2) expressed in dB, the root sum square of all the right side error sources is calculated (B·R product is not considered because they are negligibly smaller than the first term).

$$\Delta P_C = \sqrt{(\Delta A)^2 + 4(\Delta G_{ele})^2 + 4(\Delta R)^2 + (\Delta \cot\theta_{inci})^2 + (\Delta \overline{G_{STC}})^2} \tag{4AN-7}$$

In this analysis, $\Delta\overline{G_{STC}}$, ΔR, and $\Delta\cot\theta$ are much smaller than ΔA and ΔG_{ele} and are therefore neglected. While γ in A is variable, L band SAR data over Amazon exhibits constant γ in several experiments of AIRSAR [4], and SAR imaging swath has only 6 degree change in incidence angle. The above equation is then simplified and the error criteria for the ΔP_C is determined as follows:

$$\Delta P_C = 2\Delta G_{ele} \le 0.2dB(1\ sigma) \tag{4AN-8}$$

A.4.2.3 AEP estimation results and discussions

Determination of the AEP model and its comparison with onground AEP

The AEP is generated by averaging AEP coefficients over 17 scenes. These parameters and model are shown below.

$$10\log_{10} G_{ele}(\phi) = a(\phi-\phi_0)^2 + b + c(\phi-\phi_0)^4 \qquad \text{(4AN-9)}$$

a = -0.39971 Standard Deviation = 0.0372

c = -0.00133 Standard Deviation = 0.0072

ϕ_0 = 34.91 Standard Deviation = 0.16 degree

Coefficient "b" is not shown because "b" depends on γ of each scene. Determination of "b" is not the problem, here, in antenna pattern determination. Coefficient "b" should be determined using corner reflectors and active radar calibrators as a calibration problem (Chapter 5). Figs 4AN-4-a) and 4AN-4-b) show the coincidence of the best-fit correlation power model and screened correlation power for two scenes (395-309 and 415-313). In these figures, white circles plot screened data (also **mea**), and black circles plot the best-fit correlation power model (also **mod**). These figures do not plot the points where screening processing failed, so some data (white circles) are missing.

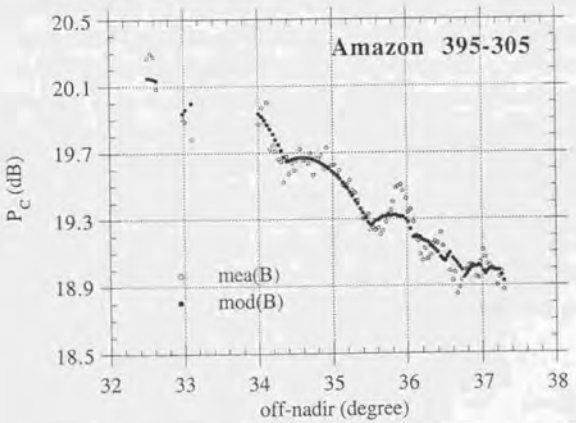

Fig. 4AN-4-a. Fitted SAR correlation power model $P_{m,i}(\boldsymbol{a})$ (black circles) and averaged correlation power $\overline{P_i}$ (white circles) for Amazon 395-305

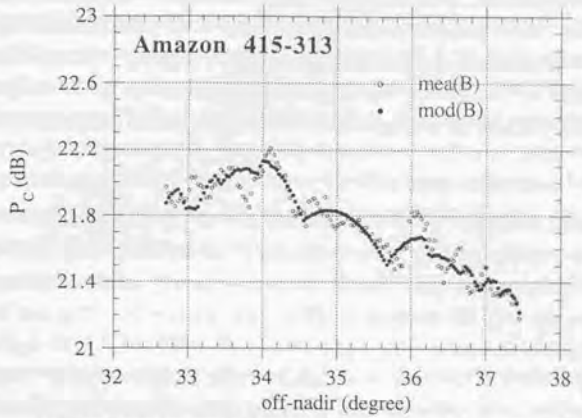

Fig. 4AN-4-b. Fitted SAR correlation power model $P_{m,i}(\boldsymbol{a})$ (black circles) and averaged correlation power $\overline{P_i}$ (white circles) for Amazon 415-313

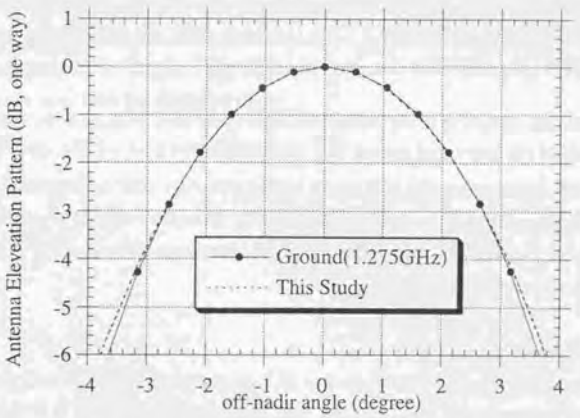

Fig. 4AN-5. Comparison of estimated antenna elevation pattern (dashed line) and ground-based measurement (solid line with black dots).

The estimated AEP and the ground-measured AEP are compared in Fig. 4AN-5. The ground measurement is made by combining the actual measurement for one 2.2 x 1.5 m antenna sub-paddle and the antenna array theory. The comparison indicates that AEPs before and after satellite launch are similar. The 3-dB down one-way beam width of the estimated AEP has been calculated to be 5.44 degrees with a standard deviation of 0.17 degrees. This is almost equal to the prelaunch value of 5.4 degrees. The fact that the half widths for all the sample images are distributed equally around the average shows the consistency of the calculation (see Table 4AN-3).

The averaged residual error, defined as the averaged difference between best-fit correlation power model in dB and averaged correlation power in dB, is 0.10 dB as shown in Fig. 4AN-6 (maximum 0.18 dB and minimum 0.06 dB). This residual error generally satisfies condition (4AN-8), but is far from the 0.01 dB obtained in SIR-B data analysis [4]. This can be explained as follows. The STC changes in 1 dB steps between 0 dB and 5 dB. A 1-dB step in the receiver may be lost in the ADC because of saturation and bit-redundancy error. This missing power is not perfectly corrected in the SAR processor as the screened image shows several stripes in azimuth [2], [3].

Repeatability

Repeatability error (E) defined below is a measure of the stability of the estimated AEP over all the images.

$$E = \sqrt{\Delta G_{ref}^2 + \Delta G_{target}^2 + \left(\overline{G_{ref}} - \overline{G_{target}}\right)^2} \quad [dB] \qquad \text{(4AN-10)}$$

where ΔG_{ref} is the standard deviation of the referenced AEP (0.10 dB); ΔG_{target} is the standard deviation of AEP obtained for each target image; $\overline{G_{ref}}$ is the reference gain (-3dB); and $\overline{G_{target}}$ is the AEP gain in the target where the half width of the reference AEP is measured. The repeatabilities of all target images are shown in Table 4AN-3. Except for scenes 11 and 17, all repeatability errors are within 0.3 dB. The value 0.21 dB is also reasonable since the included reference gain error is already 0.1 dB.

Stability of the off-nadir angle

The antenna off-nadir angles are distributed between 34.7 degrees and 35.2 degrees (centered around 35.0 degrees). An average is 34.91 degrees with a standard deviation of 0.17 degrees. This means that the antenna was deployed at a smaller off-nadir angle than designed, and illuminates a region about 4 km closer to the nadir. Originally, the SAR antenna was expected to be deployed at 35.2 degrees. However, confirmation telemetry data has not yet been obtained from the satellite. After the SAR antenna deployment, the antenna off-nadir angle was

estimated several times using satellite dynamic analysis. Results in this study qualitatively agrees with previous results.

Comparing the results of path 395 (Scene_IDs 1 to 10) with those of path 415 (Scene_IDs 11 to 17), we see that 1) these results are grouped and 2) the error increases as the scene shifts south as shown in Fig. 4AN-7. The former result is somewhat related to SAR transmission characteristics. The SAR has three transmitters, two of which were supposed to activate in the normal transmission mode. One of the three, however, is used in the normal operation in order to prevent arcing and compensate for the resultant image degradation when two transmitters are turned on. Paths 415 and 395 correspond to two transmitters. The arcing may affect the antenna boresite direction.

A.4.3 Conclusions

The antenna elevation pattern of the JERS-1 SAR has been measured by image data analysis using the Amazon rain forest SAR data whose backscattering coefficient is expected to be constant over small off-nadir angles. First, the correlated power images over these areas have been screened to remove non-similar areas from the total image. These non-similar areas are slightly darker areas, such as rivers and deforested areas, and brighter areas, such as mountain ridges. Second, a correlated power model has been developed as a function of antenna elevation pattern, receiver and ADC noises, and applied to obtain the antenna elevation pattern using the maximum likelihood estimation method. Using these procedures, the 3-dB-down, one-way beam width has been estimated to be 5.44 degrees, which is very close to the pre-launch pattern of 5.4 degree. The off-nadir angle has been estimated to be 34.91 degrees, 0.3 degrees smaller than the designed value.

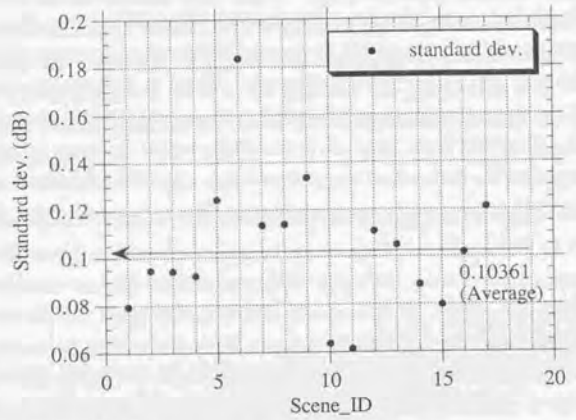

Fig. 4AN-6. Distribution of the mean residual errors for all the evaluated images.

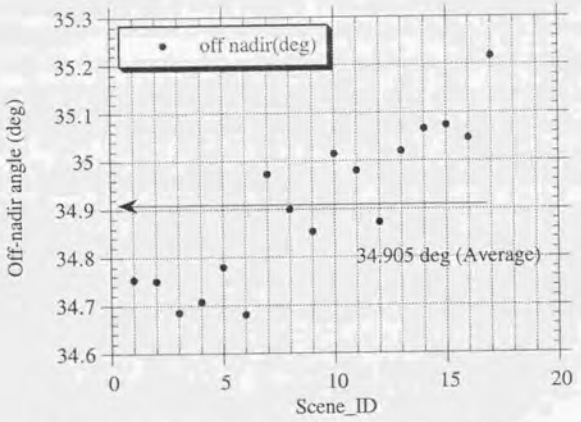

Fig. 4AN-7. Distribution of off-nadir angles of evaluated images.

References

[1] A. Freeman and J. C. Curlander, 1990, "Radiometric Correction and Calibration of SAR images," Photogrammetric Engineering and Remote Sensing, vol. 55, no. 9, pp. 1295-1301,1989.

[2] M. Shimada, "First result of the SAR characterization (in Japanese)," Technical Report of IECE SANE92-58, Nov. 1992.

[3] M. Shimada and M. Nakai, "In-flight Evaluation of L band SAR of Japanese Earth Resources Satellite-1," Adv. Space Res. vol. 14, no. 3, pp. 231-240, 1994.

[4] M. Shimada, and A. Freeman, "A Technique for Measurement of Spaceborne SAR Antenna Patterns Using Distributed Targets," IEEE Trans. Geosci. Remote Sensing, vol. 33, no. 1, pp. 100-114, Jan. 1995.

[5] Y. Nemoto, H. Nishino, M. Ono, H. Mizutamari, K. Nishikawa, and K. Tanaka, "Japanese Earth Resources Satellite-1 Synthetic Aperture Radar," Proc. of the IEEE, vol. 79, no. 6, pp. 800-809, June 1991.

[6] K. Yoneyama, T. Koizumi, T. Suzuki, R. Kuramasu, T. Araki, C. Ishida, M. Kobayashi, and O. Kakuichi, "JERS-1 Development Status," 40th Congress of the International Astronautical Federation, 1989, Beijing, China, IAF-89-118.

[7] J. D. Klein, "Spaceborne Imaging RADAR-C/SIR-C Engineering Calibration Plan," Feb. 1990, JPL Report JPL-D-6998.

[8] M. Shimada, M. Nakai, and S. Kawase, "Inflight Evaluation of L band SAR of JERS-1," Canadian Journal of Remote Sensing, vol. 19, no. 3, pp. 247-257, 1993.

[9] M. Shimada, T. Nagai, and S. Yamamoto, "JERS-1 Operation Interface Specification," NASDA document, HE-89033, Nov. 07 1991 revision-3.

CHAPTER 5 CALIBRATION USING FREQUENCY TUNABLE ACTIVE RADAR CALIBRATOR

5.1 Introduction

In this chapter, the impulse response function (IRF) of a synthetic aperture radar (SAR) image for frequency tunable reference point targets (e.g., active radar calibrator (ARC)) is analyzed. The frequency tunable active radar calibrator is an effective SAR calibration device that yields a radar cross section (RCS or σ) larger than that of a corner reflector, and displaces the response in a desirable background area for isolating from brighter man-made targets (e.g., buildings). The larger frequency shift, however, degrades the calibration accuracy because of less correlation gain and broadening resolution. We have compared a theoretically derived impulse response function with the measurement data, taking the care of the JERS-1 SAR, and have drawn the following conclusions. First, the location shift and the peak gain loss can be theoretically estimated with an accuracy of 4.2 m and 1.6 dB (a standard deviation), respectively. Second, the peak calibration method is not effective for the frequency-tunable ARC because of broadening of resolution and decrease of peak. Third, the integration method should be used for the frequency-tunable ARC. Fourth, the allowable frequency shift has an upper limit, which is about 40 Hz in the case of the L-band SAR.

5.2 Theory

5.2.1 Coordinate system

A spaceborne SAR flies on a circular orbit and transmits cascaded pulses at the pulse repetition frequency of (PRF; pulses per second) to the targets fixed to the earth, targets of which are the ARC and the background area (dashed area) in this study and move with the earth in the inertial coordinate system (see Fig. 5-1, [6]). The essence of the SAR is the possibility of carrying out compression processing of the signal's phase history in azimuth coordinate, so, the distance between the SAR and target is required to be expressed as accurate as possible. Let us express the satellite position and target position by $\mathbf{r}_s$ and $\mathbf{r}_p$, respectively, then, their distance, R, is given by

$$R \equiv \left| \mathbf{r}_s - \mathbf{r}_p \right|. \tag{5.1}$$

The round-trip time from the ARC and nearby scatterers change non-linearly as the satellite moves, as is called as the range curvature migration, for which the first-order time dependency is the range walk and the second or higher order dependency is the range curvature [5]. Range walk correction is one of the key points for forming well-focused SAR

images [3], [4], [8], although the attitude control in yaw reduces the range walk. Thus, we consider both the range curvature and range walk for model derivation and use non yaw-steered SAR data that employs a relatively large range walk for the evaluation.

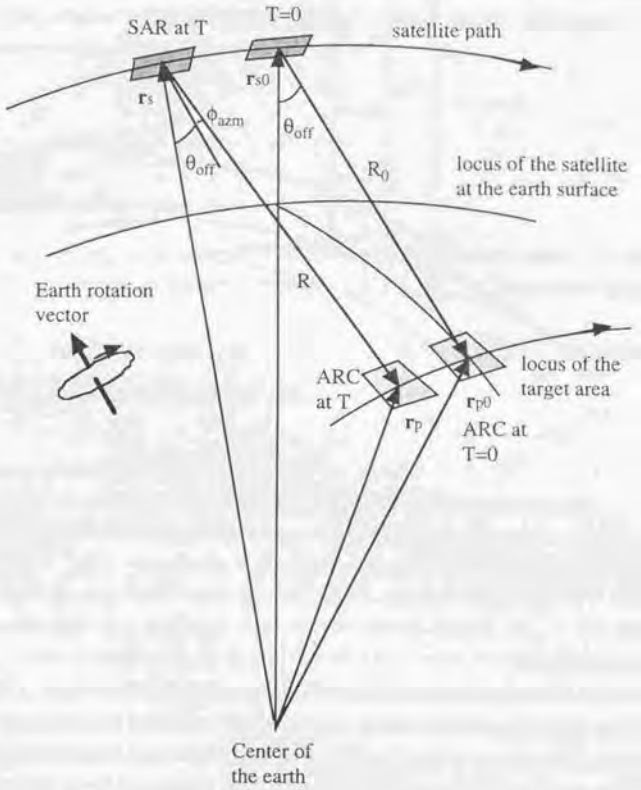

Fig. 5-1. SAR and target positions in the inertial system fixed at earth center. The ARC and the background are fixed to the earth and move with the earth. $\mathbf{r}_{p0}$ and $\mathbf{r}_{s0}$ are the satellite position and ARC positions at T = 0.

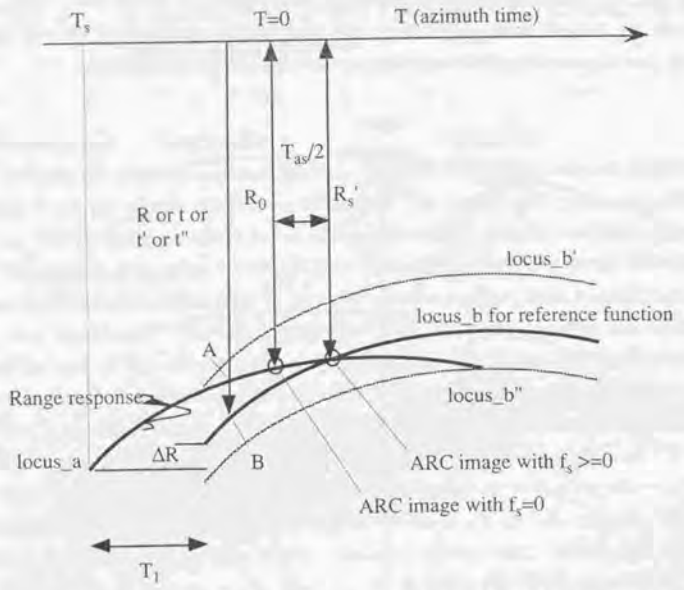

Fig. 5-2. Geometry of the azimuth correlation. The range response for ARC is on the locus_a. Phase on A is propagated to point B and correlated with the reference function along locus_b. Correlation on locus_b, therefore, maximizes the output, and those on locsu_b' and locsu_b" minimize it.

5.2.2 Received signal

Fig. 5-2 shows the range-azimuth coordinate system for SAR observation. The (slow) azimuth time coordinate, T, corresponds to motion in the azimuth direction, and the (fast) range time coordinate, t, corresponds to the pulse propagation in a perpendicular direction. Azimuth time origin, T = 0, is defined as when the ARC is observed in the antenna azimuth peak gain direction and the distance between ARC and SAR is R_0. A pulse, $\mathbf{S}_t$, transmitted to the ground at T is expressed by:

$$\mathbf{S}_t(t,T) = rect\left(\frac{t}{\tau}\right)\cdot e^{2\pi\left(f_0 t+\frac{k}{2}t^2\right)} \tag{5.2a}$$

$$rect\left(\frac{t}{\tau}\right) = \begin{cases} 1 & |t| \le \tau/2 \\ 0 & else \end{cases} \tag{5.2b}$$

where t is the time delay from T; f_0 is the transmission frequency; τ is the pulse width; and k is the chirp rate (Hz/s). Since a pulse is detected by the ARC, ARC changes the received

signal phase by the frequency of f_s (positive or negative); amplifies it; and retransmits it to the SAR until the SAR main beam is outbound from the ARC. Here, two phase modulations are initiated: one is the nonlinear phase modulation due to the time compression by the satellite - ARC relative movement; and the other is the active linear modulation by the ARC. The SAR - ARC relative motion compresses the pulse width and the time delay from the ARC at the center of the pulse as follows:

$$\tau \to \frac{c+\dot{R}}{c-\dot{R}}\tau \tag{5.3a}$$

$$t = \frac{2R}{c} \to \frac{2R}{c-\dot{R}} \tag{5.3b}$$

where $\dot{R}$ is the time derivative of distance at T and c is the speed of light. The received signal, $\mathbf{S}_r(t,T)$, is, therefore, expressed as follows:

$$\mathbf{S}_r(t,T) \propto rect\left(\frac{t-\frac{2R}{c-\dot{R}}}{\frac{c+\dot{R}}{c-\dot{R}}\frac{\tau}{2}}\right)\cdot G_{ant}\left(t-\frac{2R}{c-\dot{R}},T\right) \tag{5.4a}$$

$$\cdot e^{2\pi\left\{f_s\left(t+T+T_s\right)+f_0\left(\frac{c-\dot{R}}{c+\dot{R}}t-\frac{2R}{c-\dot{R}}\right)+\frac{k}{2}\left(\frac{c-\dot{R}}{c+\dot{R}}t-\frac{2R}{c-\dot{R}}\right)^2-f_0 t\right\}}$$

$$G_{ant}(t,T_i) \equiv G_{ele}\left(\theta_{off}\right)\cdot G_{azm}\left(\phi_{azm}\right) \tag{5.4b}$$

where f_s is the frequency shift added by ARC; T_s is the time when the ARC starts the frequency modulation; G_{ant} is the one-way relative antenna pattern; G_{ele} is the elevation pattern; G_{azm} is the azimuth pattern; θ_{off} is the off nadir angle to ARC; and ϕ_{azm} is the azimuth angle to ARC (see Fig. 5-1). Here, we do not discuss the amplitude decrease in the free space propagation. Under the maximum error of 2% within the azimuth correlation duration for spaceborne SARs, (5.4a) is approximated by

$$\mathbf{S}_r(t,T) \equiv rect\left(\frac{t-2R/c}{\tau}\right)\cdot G_{ant}\left(t-\frac{2R}{c},T\right)\cdot e^{2\pi\left\{f_s\left(t+T+T_s\right)-\frac{2\dot{R}f_0}{c}t-\frac{2Rf_0}{c}+\frac{k}{2}\left(t-\frac{2R}{c}\right)^2\right\}}. \tag{5.5}$$

In the exponent of (5.5), $f_s\cdot\left(t+T+T_s\right)$ is the phase shift introduced by ARC, $-2\dot{R}f_0 t/c$ the phase change (Doppler) within a pulse due to time compression, $-2Rf_0/c$ the phase delay between ARC and SAR, and $k/2\cdot(t-2R/c)^2$ the delayed pulse modulation. In the SAR antenna main beam, the following approximations are valid:

$$R \equiv R_0 + \frac{1}{2}\ddot{R}_0\cdot\left(T+\beta\right)^2 \tag{5.6a}$$

$$\beta \equiv \frac{\dot{R}_0}{\ddot{R}_0} \tag{5.6b}$$

$$t = \frac{2}{c}\left\{R_0 + \frac{1}{2}\ddot{R}_0(T+\beta)^2\right\} \tag{5.6c}$$

where $\dot{R}_0$ and $\ddot{R}_0$ are the first and second derivatives of slant range at T = 0.

5.2.3 Range Correlation

A range correlation output, $\mathbf{S}_{c,r}$, is given by

$$\mathbf{S}_{c,r}(t',T) = \int_{-\infty}^{\infty} \mathbf{S}_r(t,T)\cdot \mathbf{S}^*_{r,ref}(t-t')dt\ , \tag{5.7a}$$

where

$$\mathbf{S}_{r,ref}(t-t') = rect\left(\frac{t-t'-2R/c}{\tau}\right)e^{-2\pi j\frac{k}{2}\left(t-t'-\frac{2R}{c}\right)^2} \tag{5.7b}$$

is the transmission pulse with unit amplitude, "*" the complex conjugate, and t' the new variable replacing t. Integration is performed over a pulse width (-τ/2 to τ/2) centered at 2R/c. If the antenna elevation pattern does not change radically within a pulse width (within the main lobe), (5.7a) can be well approximated by

$$\mathbf{S}_{c,r}(t',T) \equiv e^{2\pi jF(t',T)}\tau\cdot\overline{G_{ele}}\left(t'-\frac{2R}{c},T\right)\cdot G_{azm}\left(t'-\frac{2R}{c},T\right)\cdot\frac{\sin\{E(t',T)\tau\pi\}}{E(t',T)\tau\pi}\ , \tag{5.8}$$

where

$$F(t',T) = f_s T + f_s T_s - \frac{2Rf_0}{c} - \frac{k}{2}\left(t'^2 - \frac{4R^2}{c^2}\right) + E(t',T)\frac{2R}{c}, \tag{5.9a}$$

$$E(t',T) = f_s - \frac{2\dot{R}f_0}{c} + k\left(t'-\frac{2R}{c}\right), \tag{5.9b}$$

and $\overline{G_{ant}}$ is the averaged antenna pattern over a pulse width. The third term on the right side of (5.9b) dominates the other two terms because k is huge. If we use δ as a deviation from R, the sinc function in (5.8) becomes $\sin(2k\tau\pi\delta/c)/(2k\tau\pi\delta/c)$ and suppresses range resolution in several meters (for standard SAR with $k \sim 1.0e^{11}$ Hz/s and $\tau \sim 35$ μs). Terms involving T in F cannot be ignored because they exist for a relatively longer duration and correlate with the

azimuth reference function. Note that different existence areas of the two integrands in (5.7a) does not produce a significant error (see Appendix).

5.2.4 Azimuth Correlation

The azimuth correlation is the same as the range correlation except that the integration is conducted on the range curvature. The range curvature is the locus of any target location on the azimuth time (T) - slant range (or t') coordinate system, and is bounded by the antenna azimuth pattern and the processing frequency width. Let the locus_a in Fig. 5-2 be the range curvature for the ARC response. Since the azimuth reference function is defined on the locus_b which is almost the same as locus_a shifted by the azimuth time delay T_1 in T (i.e., $T \to T - T_1$) and by the range shift ΔR in R (i.e., $R_0 \to R_0 + \Delta R$), the expressions for the locus_b in terms of R" and t" become:

$$R'' \equiv R_0 + \Delta R + \frac{1}{2}\ddot{R}_0\left(T - T_1 + \beta'\right)^2 \tag{5.10a}$$

$$t'' \equiv \frac{2}{c}\left\{R_0 + \Delta R + \frac{1}{2}\ddot{R}_0\left(T - T_1 + \beta'\right)^2\right\} \tag{5.10b}$$

where β' is an estimation from knowledge on the orbit, attitude, and Doppler azimuth spectrum. Although erroneous information makes β' slightly different from β, we assume β = β' for simplicity. On the locus_b, we do not consider the frequency shift at the ARC, so the azimuth reference function, $\mathbf{S}_{a,ref}$, should be

$$\mathbf{S}_{a,ref}(T - T_1) = rect\left(\frac{T-T_1}{T_a}\right)e^{-\frac{2f_0}{c}R''}. \tag{5.11}$$

Then, the azimuth correlation output, $\mathbf{S}_{c,r,a}$, is given by

$$\mathbf{S}_{c,r,a}(t'',T_1) = \int_{-\infty}^{\infty}\mathbf{S}_{c,r}(t'',T)_{locus\_b}\mathbf{S}^*_{a,ref}(T-T_1)_{locus\_b}dT, \tag{5.12}$$

where T_a is the azimuth correlation duration. Since the azimuth antenna pattern in (5.8) changes steeply within the azimuth correlation duration, it cannot be moved out from the integration of (5.12). Integrand $\mathbf{S}_{c,r}$ on the locus_b can be interpolated by replacing t' of (5.8) by t" of (5.10b). The Taylor expansion of the exponential terms in the two integrands and rearrangement of the dominant terms simplify (5.12) to:

$$S_{c,r,a}(t'',T_i) \equiv \overline{G}_{ele}\left(t''-\frac{2R}{c}\right) \cdot \int_{-\infty}^{\infty} rect\left(\frac{T-T_i}{T_a}\right) \cdot G_{azm}\left(t''-\frac{2R}{c},T\right)\frac{\sin\left(E(t'',T)\pi\tau\right)}{E(t'',T)\pi\tau} e^{2\pi j(f_s+f_{DD}\cdot T_i)T} dT \quad , \tag{5.13}$$

where

$$E(t'',T) \equiv f_s + f_{DD}\beta + \frac{2k}{c}\left\{\Delta R - \frac{1}{2}\ddot{R}_0 T_i\left(-T_i+2\beta\right)\right\} - \left(-f_{DD}+\frac{2k}{c}\ddot{R}_0 T_i\right)T, \tag{5.14}$$

and f_{DD} is the Doppler chirp rate given by $-2f_0\ddot{R}_0/c$. The $\exp\left\{2\pi jT_i\left(f_s+f_{DD}T_i\right)\right\}$ in (5.13) provides a sinc-function-like output after the integration. The $\sin(\tau\pi E)/(\tau\pi E)$ maximizes the integration if we select such ΔR that crosses locus_b and locus_a at their centers (see Fig. 5-2). The integration is then maximized at:

$$T_i \equiv T_{as} = -\frac{f_s}{f_{DD}} \tag{5.15a}$$

$$\Delta R = \frac{1}{4}\ddot{R}_0 T_{as}\left(\frac{T_{as}}{2}+2\beta\right) \tag{5.15b}$$

where T_{as} is the azimuth time shift. The azimuth location shift (x_a) and range location shift (x_r), then, are given by:

$$x_a = T_{as}V_g \tag{5.16a}$$

$$x_r = \dot{R}_s - R_0 = \ddot{R}_0\beta T_{as} = \dot{R}_0 T_{as} \tag{5.16b}$$

where V_g is ground speed of the beam center along the sub-satellite track. Thus, IRF moves in the azimuth direction and its shift amount depends on the frequency shift (f_s) and Doppler chirp rate (f_{DD}); IRF also moves in the range direction if the product of slant range velocity at the center of the beam and time shift (T_{as}) is bigger than a range resolution; if the antenna beam is controlled to track $\dot{R}_0 = 0$ (i.e., yaw steering), range shift is eliminated; and the decreased overlapped area of two loci may looses the correlation gain (see Fig. 5-2). A computation with parameters based on JERS-1 SAR (Table 5-1) evaluated the dependence of the impulse response peaks on the frequency shift, and showed that the correlation gains decrease as f_s increases (Fig. 5-3); and the correlation gain loss is predicted to be -10.1 dB at f_s = 180 Hz.

Table 5-1. Parameters of the SAR simulation

Parameter	Value
f_0	1.275 GHz
f_s	0-200 Hz
k	-4.2857e11 Hz/s
c	300,000 km/s
τ	35μs
Height	568 km
R_0	730 km
T_a(s)	1.8

Note that JERS-1's orbit data and ARC's actual locations were used for the simulation parameters.

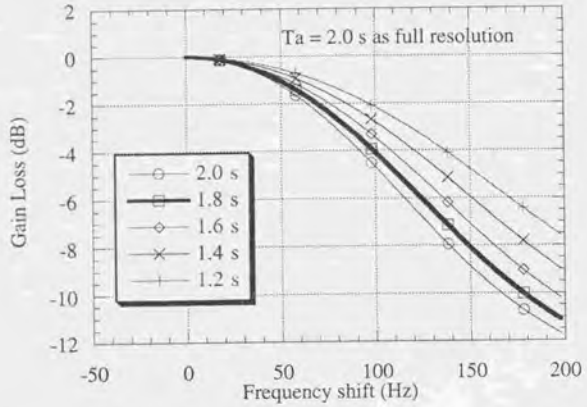

Fig. 5-3. Frequency-shift dependency of the correlation gain loss. Number shows the azimuth integration time.

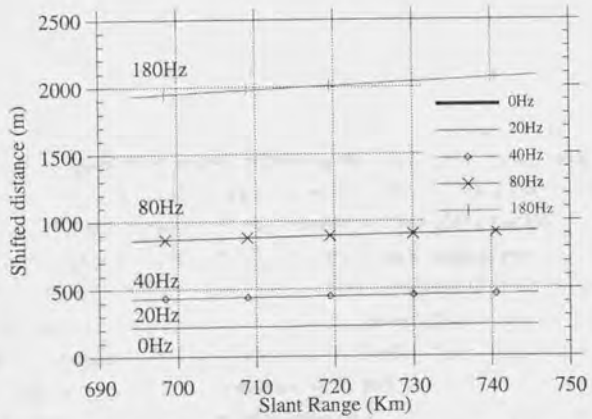

Fig. 5-4. Slant range dependency of the ARC location shift for five different frequency shifts (0, 20, 40, 80, and 180 Hz).

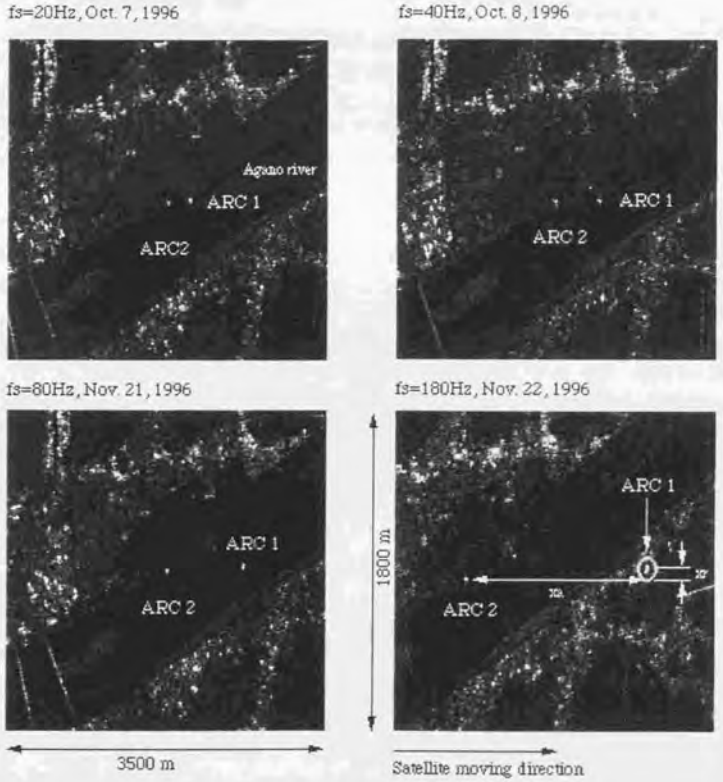

Fig. 5-5. Sample images of the shifted ARC point targets, fs = 20, 40, 80, and 180 Hz (top left, top right, bottom left, and bottom right). In order to distinguish the ARC 1 image at f_s = 180 Hz from the bright targets on the land, it is surrounded by a white circle.

5.3 Experiments

Calibration experiments for JERS-1 SAR were conducted using two L-band, frequency-tunable ARCs varying f_s from 0 to 180 Hz at Japanese test sites. The experiments sought to acquire data relating the frequency shift and the location shift, correlation gain loss, and the resolution broadening. The models developed in the previous section were verified and the applicability of such ARC to the calibration was evaluated.

5.3.1 Frequency-tunable ARC

The L-band frequency-tunable ARC has been introduced in Chapter 2. While the SAR pulse is being detected, the phase controller continues mixing the signal (S_{ARC}) whose phase changes linearly with time since the pulse is first detected.

$$S_{ARC} = e^{2\pi j (f_c T + f_s T_s)} \tag{5.17}$$

5.3.2 SAR products

We use full-resolution (single-look) slant-range complex data processed by the range-Doppler type SAR processor [19]. Eight times interpolation using the FFT [11] was applied to analyze the IRF. This SAR data is corrected for sensitivity variations by the antenna pattern, sensitivity time control (STC), and automatic gain control (AGC) [9]. A rectangular window function was selected in generating the SAR data in order to compare the data with the theory. We selected 42 dBm^2 as ARC's σ, so as not saturate the SAR raw data but achieve a signal-to-clutter ratio of 30 dB for the background σ^0 of -10 dB.

5.3.3 Experimental description

The JERS-1 recurrence cycle is 44 days, and the path moves 49 km west every day at a latitude of around 35 deg. A 26 km (75 km minus 49 km) area can be doubly observed over two consecutive days, i.e., the first day for the far range and the second day for the near range. We established the following experiment strategy: first, we selected test sites that can be observed by SAR over two consecutive days; second, we located two ARCs at the same slant ranges in order to exclude the SAR intensity dependency on the slant range; third, we always frequency-shifted ARC 1 but not ARC 2.

Because the Doppler chirp rate depends on the slant range, the IRF azimuth location shift slightly depends on the ARC's physical location. From an example for the JERS-1 restituted orbit of path 66 on Aug. 19, 1993, we estimated the differential location shift to be

approximately 10m/Hz (e.g., 200m for 20 Hz, 400 m for 40 Hz, 900 m for 80 Hz, and 2000 m for 180 Hz, Fig. 5-4).

Table 5-2 shows the history of the experiments and the parameter configuration for the two ARCs. Test sites were selected from the NASDA calibration sites, Hatoyama site (N 35 deg 58'50.4", E 139 deg 23'14.4"), Kumagaya site (N 36 deg 08'00.5", E 139 deg 16'52.9"), and Niigata site (N 37 deg 54'26.3", E 139 deg 09'11.5"). Combinations of frequency shifts and the ARC locations should be carefully selected so that the responses can be seen on the dark background and recognized as clearly as possible. Ideal backgrounds are rivers running near all the above test sites. However, those rivers are less than 500 m wide, and the effective river width along the satellite track is less than 1,000m. For a location shift of 2000m, the IRF moves across the river. The ARC physical location is adjusted across the track so that the IRF can fall in rice fields and not in the nearby urban area.

Figs 5-5-a, b, c, and d show the typical ARC image samples at Niigata test site in response to the four different frequency shifts. Each image size is 3520 m (azimuth) x 1800 m (slant range). We confirm that more frequency shift defocus the IRF, and moves it in azimuth and range directions. For these figures, ARC 1 and ARC 2 were deployed at almost same location; and their locations differ only a few meter.

Table 5-2. Experiments using the ARC with frequency shift

	ARC 1		ARC 2			
No.	f_s (Hz)	x_m (m)	f_s (Hz)	x_m(m)	Date	Site
1.	40	462.5	0	0	11/16/'93	Niigata
2.	0	0	0	0	11/17/'93	Niigata
3.	0	0	0	0	2/11/'94	Oppe
4.	180	2026	0	0	5/10/'94	Oppe
5.	80	862.5	0	0	5/11/'94	Kumagaya
6.	180	0	0	0	6/25/'94	Niigata
7.	0	0	0	0	8/6/'94	Oppe
8.	80	862.5	0	0	8/7/'94	Kumagaya
9.	80		0	0	9/20/'94	Niigata
10.	40	0	0	0	9/21/'94	Niigata
11	0	0	0	0	10/21/95	Niigata
12	0	0	0	0	10/22/95	Niigata
13	20	223	0	0	7/25/95	Oppe

Remarks RCSs are selected as 42 dBm^2 for both ARCs. JERS-1 SAR is incorporated in this experiment. x_m is the measured location shift (m)

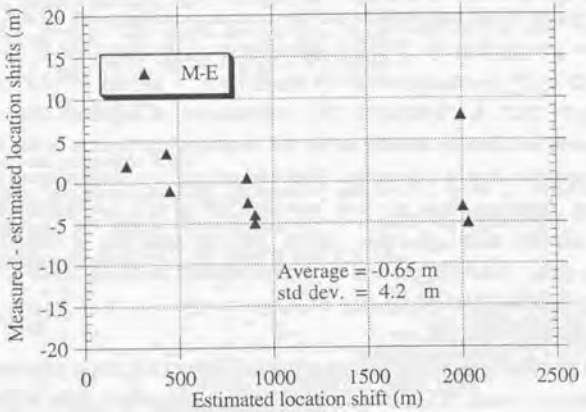

Fig. 5-6. IRF location difference (M measured; E estimated) VS. Estimated location.

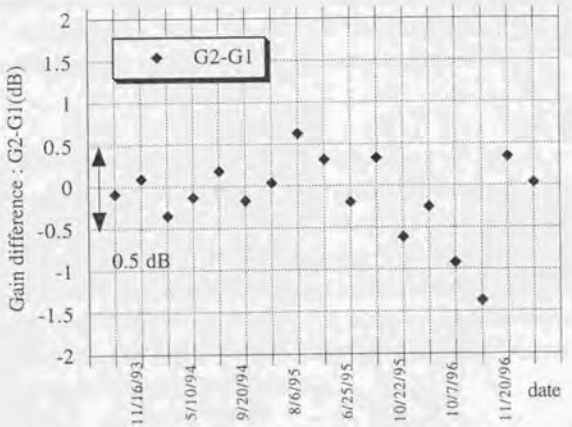

Fig. 5-7. History of the gain difference between ARC 2 and ARC 1.

5.4 Analysis and Discussion

Analyses were conducted for location shift, correlation gain loss, resolution broadening, adaptability of the frequency tunable ARC to the calibration, and the frequency shift allowance.

5.4.1 Image shifts in azimuth and range

Fig. 5-6 shows the location difference between the measured azimuth shift (x_m) and the theoretical azimuth shift (x_e) at five frequency shifts. The mean difference is -0.65 m, and the standard deviation, 4.2 m. These errors might arise from manual recognition of the IRF and satellite velocity determination error. The velocity error is around 15 cm/s for each component [16], it deviates the Doppler chirp rate error of around only 0.007%. We then conclude that orbital may not be the main error. A good estimation of the location shift requires the accurate calculation of the Doppler chirp rate f_{DD} [6]. Range image shift has been confirmed from Fig. 5-5-d, for which the theoretical shift x_r at fs = 180 Hz is 59 m ($\bar{R}_0$ = 0.22 km/s, and T_{as} = 0.28 s); and the measured shift in slant range is 63 m; therefore, both agree very well.

5.4.2 Correlation Gain Loss

To evaluate the correlation gain loss, the ARCs' receiver gain must be known for each experiment. If an ARC can transmit two equal-amplitude signals simultaneously, one frequency-shifted and the other not frequency-shifted as same as the time delay ARC [12], the measurement loads for these ARC differences may be reduced. The ARCs used in these experiments were manufactured to stabilize within ± 0.5 dB over two years. To ensure measurement credibility, however, those gains were monitored all through the experiments using the calibrated signal generators and spectrum analyzers before and after the satellite passages. Results confirmed that the two receiver gains differ within 0.5 - 1.0 dB except at several points (Fig. 5-7).

The clutter and the less-focused SAR data may prevent accurate detection of the impulse response peak as well. In turn, the integration of the impulse response is known to be well stabilized [2]. We introduced the following two parameters (R_P and R_I) for the gain loss evaluation:

$$R_p = \frac{P_1(0,0) - P_{back,1}}{P_2(0,0) - P_{back,2}} \cdot \frac{G_2}{G_1} \qquad (5.18a)$$

$$R_I = \frac{\iint_{A_1}\{P_1(x,y) - P_{back,1}\}dxdy}{\iint_{A_2}\{P_2(x,y) - P_{back,2}\}dxdy} \cdot \frac{G_2}{G_1} \qquad (5.18b)$$

where R_P is the gain loss ratio measured by the peak value; R_I is the gain loss ratio using the integral method; $P_1(x, y)$ and P_2 are the impulse response function of ARC 1 and ARC 2; G_1 and G_2 are the gain of ARC 1 and ARC 2; and $P_{back,1}$ and $P_{back,2}$ are the averaged background intensity for ARC 1 and ARC 2. We selected the integral area "A_1" (A_2) that surrounds the impulse response to be as large as possible but not to contain other brighter targets. Background intensity is estimated from the far sides of the above integral areas.

The evaluation results are given in Fig. 5-8. Measured peak gain losses (R_P) are shown by black diamonds (◆), measured integral gain losses (R_I) by (◇), theoretical correlation (peak) gain loss by the solid thin line, and theoretical integral correlation gain loss by the solid thick line. The azimuth integration time is set to 1.8 seconds. Integral gain loss shows good agreement between the theory and the measurements with a standard deviation of 0.7 dB and a mean residue of -0.3 dB. However, the peak gain loss exhibits slightly worse agreement with a standard deviation of 1.6 dB and a mean residual of 0.1 dB. This means that the correlation gain loss due to the frequency shift can be estimated from the theoretical model (integral method has much better agreement than peak method), and the resultant calibration factor variation could be corrected. We summarize the differences at the peak and integral methods in Tables 5-3 and 5-4.

Table 5-3 Comparison of the theoretical gain loss (peak and integral)

no.	f_s(Hz)	R_P(peak)(dB)	P_I(integral)(dB)
1	0	0	0
2	20	-0.15	-0.00
2	40	-0.65	-0.01
3	80	-2.67	-0.05
4	180	-10.14	-0.24

Table 5-4 Comparison of the peak and integral method

	Peak method	Integral method
Mean residual	0.1 dB	-0.3 dB
Standard deviation	1.6 dB	0.7 dB

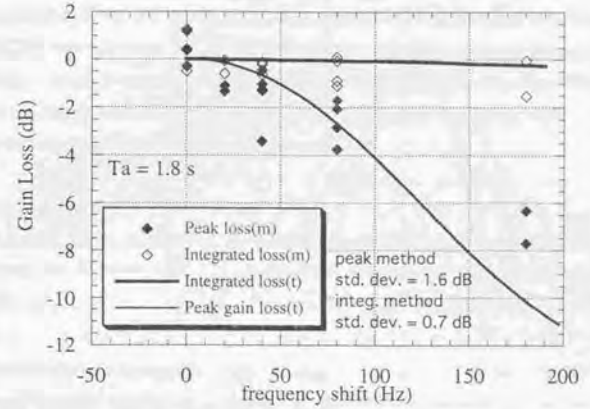

Fig. 5-8. Peak power loss and integral power are plotted for the frequency-shifted ARC.

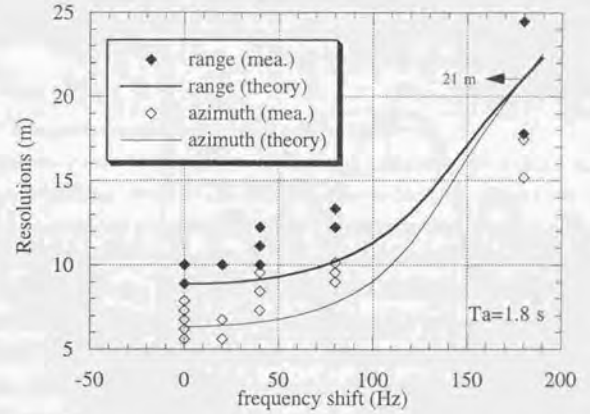

Fig. 5-9. Frequency dependence of the range and azimuth resolutions for the measured data and the model.

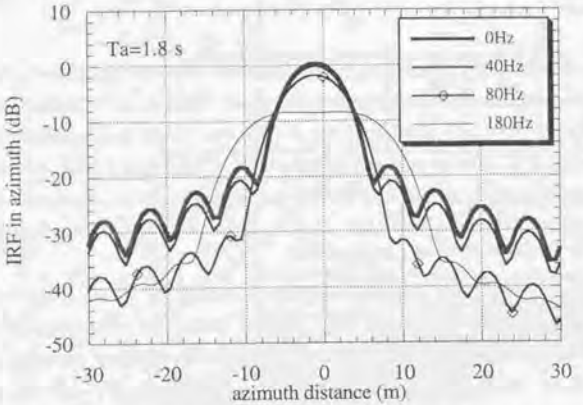

Fig. 5-10. Azimuth cross section of the impulse response function centered at each location shift. The vertical axis is normalized by the peak at $f_s = 0$ Hz.

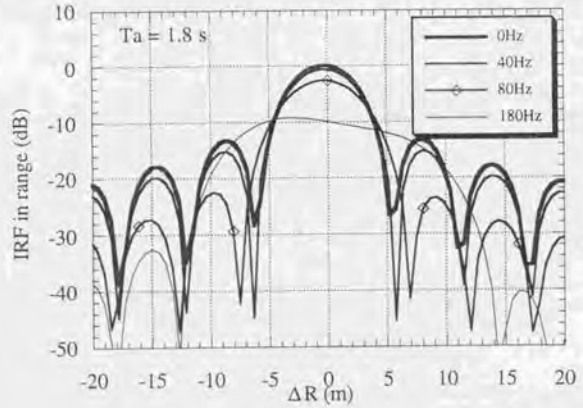

Fig. 5-11. Range cross section of the IRF. The vertical axis is normalized by the peak of the referenced IRF with $\Delta R = f_s = 0$.

5.4.3 Resolutions

Fig. 5-9 compares the measured and simulated azimuth and range resolutions (3dB down width). This shows that both azimuth and range resolutions agree well with the theoretical values until f_s = 20 Hz; the theoretical values are lower than the measurements for f_s of 40 and 80 Hz; and after that the theoretical values exceed the measurements. Disagreement at $f_s \geq 80$ Hz is probably because the range-Doppler SAR processing algorithm used in this study is not perfectly matched to the data and needs some improvements. Simulations of the azimuth and range resolutions are as follows.

Azimuth resolution

The azimuth cross sections of the impulse response function are calculated from (5.13) by deviating the azimuth time (T_1) around the shifted time (T_{as}) and fixing ΔR as given by (5.15b). Fig. 5-10 shows the results for four frequency shifts (f_ss; 0, 40, 80, and 180 Hz) with the azimuth distance ($V_g(T_1 - T_{as})$) instead of azimuth time. We confirmed that the azimuth resolution of the single-look image is almost 6 m until f_s is less than 80 Hz; after that, it becomes broader quickly as f_s increases; the IRF for f_s = 180 Hz has the wider Plato peaks than the lower frequency cases.

Range resolution

A similar calculation is performed for the range resolution by changing ΔR in (5.13) from -20 m to 20 m at $T_1 = T_{as}$. Fig. 5-11 shows that the best resolution is confirmed to be 9 m for f_s of 40 Hz; but for f_s = 180 Hz resolution quickly increases to 22 m and asymmetry appears.

5.4.4 Discussion on the calibration applicability

The frequency-tunable ARC has several advantages compared with the standard ARC (non - frequency tunable). Shifting the impulse response location to a low back ground area or an area which does not receive radiometric interference from brighter man-made target is the major advantage. Although the ARC can generate a larger radar cross section, the interference from other targets or medium bright clutter decreases the quality of the impulse response. This shifting capability is thus welcomed when searching for a test area that is easily accessible from the data processing/calibration center located in an industrialized area. In turn, the correlation gain loss, the resolution broadening, and some complexity of manufacturing the phase shifting function are the disadvantages. The applicability of such ARC to calibration is discussed below in terms of the improvement of the calibration coefficient.

Two representative SAR calibration methods using the point target responses are the peak method and the integral method. Ulander [17] theoretically compared the accuracy of those

two methods, and summarized that the peak method achieves smaller error than the integral method if the image is well focused, but that the integral method is a robust method regardless of the SAR focus.

The calibration coefficient by the peak method depends on the peak value of the response, and the azimuth / range resolutions. As shown in Figs. 3 and 11, those terms are significantly reduced in higher frequency (e.g., the peak value by 10.1 dB at f_s = 180 Hz, the azimuth resolution to 22 m from 6 m, and the range resolution to 22 m from 9 m), and drop the calibration coefficient dramatically. The SAR image may be calibrated with an accuracy of 1.6 dB if no error is assumed for resolution estimation. We, however, can not recommend this method because integral method gives better results.

The calibration coefficient by the integral method depends only on the integration of the impulse response function, not on the resolutions. As shown in Fig. 5-8, the theoretical integral gain loss agrees well with the measurement with an accuracy of 0.7 dB. This means that the integral method corrects the calibration coefficients with good accuracy. Although the hardware limitations do not allow evaluating the integral gain loss at higher f_s than 180 Hz, we expect that the integral method can be applied to higher frequency cases.

Defocusing affects the resolution measurement, which is one item of the SAR image quality. From Fig. 5-9, azimuth and range resolutions become broader as f_s increases. The range cross section becomes asymmetric at f_s = 180 Hz (Fig. 5-11), and the range and azimuth responses differ from the case of $f_s = 0$ if f_s exceeds 80 Hz (Figs. 12 and 13). The frequency shift should therefore be preferable less than 40 Hz from the image quality evaluation point of view.

5.5 Conclusions

In this chapter, we have shown that the frequency tunable active radar calibrator suffers from correlation gain loss and the resolution broadening as disadvantages; but it has a location shifting advantage. We have verified that the correlation gain loss can be estimated theoretically with an accuracy of 1.6 dB and the location shift in 4.2 m. We have proposed that the integral method is a robust calibration method for using frequency-tunable ARC; and the frequency shift should be less than 40 Hz for image quality evaluation for L band spaceborne SAR.

Appendix 5-1 Range correlation

We consider coefficient "a" in the range reference function sin(ax)/ax. Range correlation output is given by:

$$P(t') = \int_{-\infty}^{\infty} S_{rec}(t) \cdot S_{REF}(t+t')^{*} dt = \int_{-\infty}^{\infty} rect(\frac{t}{\tau}) rect(\frac{t+t'}{\tau}) e^{-j2\pi(\frac{k}{2}2tt' + \frac{k}{2}t'^2)} dt \,, \tag{5A.1}$$

where

$$S_{rec}(t) = rect(\frac{t}{\tau}) \cdot e^{j2\pi\frac{k}{2}t^2} \,, \tag{5A.2}$$

$$S_{REF}(t+t') = rect(\frac{t+t'}{\tau}) \cdot e^{j2\pi\frac{k}{2}(t+t')^2} \,. \tag{5A.3}$$

For, $t' > 0$ (on, $t' < t/2$),

$$P(t') = e^{-j\pi kt'^2} \int_{-\tau/2}^{\tau/2-t'} e^{-j2\pi kt't} dt \tag{5A.4}$$

$$= e^{-j\pi kt'^2} \left[\frac{e^{j2\pi kt't}}{j2\pi kt'} \right]_{-\tau/2}^{-\tau/2+t'} + e^{-j\pi kt'^2} \left[\frac{e^{j2\pi kt't}}{j2\pi kt'} \right]_{-\tau/2+t'}^{\tau/2-t'}$$

$$\equiv e^{-j\pi kt'^2} \frac{\sin\{\pi B_c t'(1-2t'/\tau)\}}{\pi B_c t'(1-2t'/\tau)} (\tau - 2t') \tag{5A.5}$$

where k is the chirp rate, τ is the pulse width, and B_c the transmission band width. Since

$$t' = \frac{2r}{c}, \tag{5A.6}$$

$$|P(t')| \equiv \frac{\sin\{\frac{2\pi B_c r}{c}(1-\frac{4r}{\tau c})\}}{\frac{2\pi B_c r}{c}(1-\frac{4r}{\tau c})} (\tau - \frac{4r}{c}) \tag{5A.7}$$

where r is the slant range. (5A.7) is not strictly in the form sin(ax)/(ax). However, if

$$r << \frac{c\tau}{4}, \tag{5A.8}$$

then,

$$|P(t')| \equiv \frac{\sin(\frac{2\pi B_c r}{c})}{\frac{2\pi B_c r}{c}} \,. \tag{5A.9}$$

Here, the coefficient "a" becomes

$$a = \frac{2\pi B_c}{c} = \frac{2\pi \cdot 15\times 10^6 / \sec}{300000\, km/\sec} = 10\pi \,. \tag{5A.10}$$

References

[1] M. Fujita, "An Active Reflector for SAR Calibration Having a Frequency Shift Capability," IEICE Trans. Commun., vol. E75-B, no. 8, pp. 791-793, Aug. 1992.

[2] A. Laurence Gray, P. W. Vachon, C. E. Livingstone, and T. I. Lukowski, "Synthetic Aperture Radar Calibration Using Reference Reflectors," IEEE Trans. Geosci. Rem. Sens., vol. 28, no. 3, pp. 374-383, May 1990.

[3] W. J. van de Lindt, "Digital Technique for Generating Synthetic Aperture Radar Images," IBM J. Res. Develop., vol. 21, no. 5, pp. 415- 432, Sept. 1977.

[4] C. Wu, "A Digital Approach To Produce Imagery From SAR Data," presented at the AIAA Syst. Design Driven by Sensors Conf., paper no. 76-968, Pasadena, CA, OCT. 18-20, 1976.

[5] R. K. Raney, "Synthetic-aperture imaging radar and moving targets," IEEE Trans. Aerosp. Electron. Syst., vol. AES-7, no. 3, pp. 499-505, May 1971.

[6] Curlander and McDonough, "Synthetic Aperture Radar, Systems, and Signal Processing," Wiley, 1991.

[7] N. Kodaira, "Possibility of the use of a Transponder as an Active SAR Calibration target," in Proc. IGARSS '89, Vancouver, Canada, July 10-14, 1989, pp. 258 - 260.

[8] M. Y. Jin and C. Wu, "A SAR Correlation Algorithm which Accommodates Large-Range Migration," IEEE Trans. Geosci. Rem. Sens., vol. GE-22, no. 6, pp. 592-597, Nov. 1984.

[9] M. Shimada and M. Nakai, "In-flight Evaluation of L band SAR of Japanese Earth Resources Satellite-1," Adv. Space Res., vol. 14, no. 3, pp. 231-240, 1994.

[10] NASDA contract report CDA-3-727, "Development of the active radar calibrator for JERS-1/ERS-1 SAR," Mitsubishi Electric Corporation, 1989.

[11] A. Freeman, J. C. Curlander, P. D. Dubois, and J. Klein, "SIR-C Calibration Workshop Report," JPL Center for Radar Studies Publication, no. 88-003, Nov. 1988.

[12] P. S. Daleman, R. K. Hawkins, and T. I. Lukowski, "Experience with Active Radar Calibrators for Airborne SAR," in Proc. IGARSS '90, Rem. sens., pp. 795-798, College park, Maryland.

[13] T. I. Lukowski, R. K. Hawkins, B. Brisco, R. Brown, R. Ford, and P.S. Daleman, "The Saskatoon SAR Calibration Experiment," in Proc. IGARSS'89, Rem. Sens., pp. 254-257, Vancouver, Canada.

[14] D. R. Brunfeldt, "SAR response to Modulated Target," in Proc. IGARSS'89, Rem. Sens., pp. 2901-2905, College Park, Maryland.

[15] S. Dill, D. Hounam, and K. H Wagel, "Generation of invisible SAR Targets Using Coded Transponder," In Proc. SAR cal. workshop of CEOS CAL/VAL, 20-24 Sept. 1993, ESTEC, pp 65-76.

[16] Communication with the tracking network technology department of Tsukuba Space Center/NASDA.

[17] L. M. H. Ulander, "Accuracy of Using Point Targets for SAR Calibration," IEEE Trans. Aerosp. Electronic Systems, vol. 27, no. 1, pp. 139-148, Jan. 1991.

[18] D. R. Brunfeldt and F. T. Ulaby, "Active Reflector for Radar Calibration," IEEE Trans. Geosci. Remote Sensing, vol. GE-22, no. 2, pp. 165-169, March 1984.

[19] M. Shimada, "A multi-platform verification processor for the SAR calibration and the interferometry," submitted to Cosper'98.

CHAPTER 6 SAR CALIBRATION EXPERIMENT USING FLAT-RAIN-FOREST IMAGE AND EXTERNAL CALIBRATORS

6.1 Introduction

In this chapter, we will verify the calibration method developed in Chapters 3, 4, and 5 by using the JERS-1 SAR data, as an example of low-dynamic range SAR data. Difficulty in calibrating JERS-1 SAR are that 1) the sensitivity time control (STC) and the automatic gain control (AGC) change the receiver gain quickly, 2) 3-bit A/D converter has limited dynamic range, and 3) the data is always saturated in the near range region and coastal region. SAR images at the rainforest and point-targets were used. We evaluate the across track radiometric variations and calibration accuracy using the peak method and the integral method. We also propose a method to eliminate interference from ground radars.

It was reported that the JERS-1 SAR performance almost meets the specification except for several points: a smaller SNR (5 to 6 dB) over land, slight saturation of the raw data, serious saturation in coastal areas, and the frequency interference from the ground radar signals [1], [2]. These deviations are caused by a lower transmission power (325 W instead of 1300 W) and a time-variant receiver gain that is automatically selected slightly beyond the adequate level for the incoming signal. Initially the JERS-1 SAR was evaluated using the SAR images that were not corrected for saturation [1]. Here, the SAR images that were corrected following Chapter 3, 4, and 5 were evaluated and the SAR calibration was conducted.

Section 6.2 summarizes the preprocessings to compensate for the saturation, to determine the SAR sensitivity, and the calibration methods. Next, we evaluate the SAR data using the Amazon rain forest and check discontinuities over two-path SAR images. We also evaluate the stability at the peak and integral calibration methods. In section 6.3, we summarize the image quality of the saturation-corrected SAR data. Finally, we describe a method to eliminate the ground radar interference.

6.2 Theory

6.2.1 Radar Equation

The radar equation for slightly saturated SAR correlation data (image data) is modeled [10]. These SAR image data can be radiometrically corrected by scaling the input signal so as to compensate the saturation-reduced-correlation gain. Let us consider SARs which employ a sensitivity time control (STC) and an automatic gain control (AGC), as low-dynamic range SARs. The raw data is scaled by

$$\begin{pmatrix} V_I \\ V_Q \end{pmatrix} = \frac{1}{\sqrt{G_{AGC}(T)\cdot G_{STC}(t)\{1-S_a(t,T)\}}} \cdot \begin{pmatrix} I-\bar{I} \\ Q-\bar{Q} \end{pmatrix}, \tag{6.1}$$

where V_I and V_Q are the scaled in-phase and quad-phase signals; I and Q are the in-phase and quad-phase signals; $\bar{I}$ *and* $\bar{Q}$ are the averaged I and Q values; G_{AGC} is the receiver gain at the azimuth time (T); G_{STC} is the sensitivity time control's gain at range time (t); and S_a is the saturation rate defined in [10]. From Chapter 3, the SAR correlation power P_C' can be approximated by the signal component and the noise component as:

$$P_C \equiv \alpha\left(\frac{G_{ele}^2}{R^3\sin\theta} + \frac{\beta}{\alpha}\cdot R\right), \tag{6.2}$$

$$\alpha = \left(\tau f_{sample}\frac{PRF}{2V_g\rho_a}\lambda\right)^2 \frac{P_t G_0^2 \lambda^2}{(4\pi)^3}\left(\sigma^0\delta_a\delta_r L\cdot D\cdot N_L\right), \tag{6.3a}$$

$$\beta = \tau f_{sample}\frac{PRF}{2V_g\rho_a}\lambda N_L 2\sigma_{n0}^2, \tag{6.3b}$$

where P_t is the transmission power; G_0 is the antenna peak gain; λ is the wave length; τ is the pulse duration; f_{sample} is the sampling frequency; PRF is the pulse repetition frequency; V_g is the satellite ground speed; σ^0 is the normalized radar cross section; δ_a is the azimuth pixel spacing; δ_r is the range pixel spacing; ρ_a is the azimuth resolution; L is a system loss; σ_{n0} is the thermal noise power; θ is the local incidence angle; G_{ele} is the antenna elevation pattern; and R is the slant range.

A constant α can be determined by using the external calibration signals, and β/α from the raw data analysis (Chapter 4). Ignoring noise component, we obtain the calibration factor (CF) to convert P_c' or its linearly scaled digital number to the normalized radar cross section, σ^0. The general form is

$$\sigma^0 = CF\cdot\frac{\langle P_C\rangle}{\delta_a\delta_r}, \tag{6.4}$$

where $\langle\ \rangle$ means averaging.

6.2.2 Radar parameters

Among several parameters in (6.2), the antenna elevation pattern should be carefully determined because it causes a weak intensity difference at the two-path image's boarder.

Sensitivity Time Control

G_{STC} can be modeled by evaluating the receiver responses to the following inputs: 1) thermal noise generated from the noise generator, 2) SAR observation data for dark targets (like the ocean), and 3) that for uniform targets (like the Amazon rain forest). If the STC circuit is made of a set of discrete attenuators (i.e., JERS-1 SAR employs 0, 1, 2, 4 dB unit attenuators to generate a specific attenuation of 5 dB), statistical evaluation of the output at different attenuators can express the attenuation model. Fig. 6-1 shows the two relationships between the raw power and the attenuation level (integer). The upper curve is for ocean data, and the lower curve is for preflight measurement. The higher the raw power is, the lower the gradient is. This predicts that G_{STC} can not be modeled from the Amazon data. We therefore used the preflight noise for determining the attenuator model. Fig. 6-1 shows that the gradient is not 1.0 (but slightly less than 1.0) and all the unit attenuators have the same gradient. Thus, G_{STC} can be modeled by using the gain number (K) in the satellite telemetry, such as

$$G_{STC}(t) = 10^{-K(t)/10}. \tag{6.5}$$

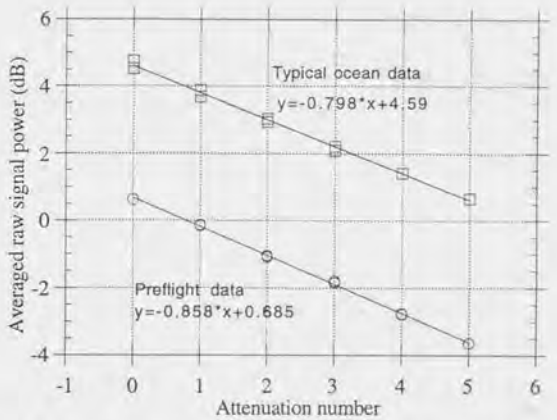

Fig. 6-1. Relationships between ADC output power (dB) and the attenuation level (dB) for preflight data (lower curve) and ocean observation data (upper curve). Both axes are relative values.

Automatic Gain Control

AGC is composed of a constant-gain receiver and a set of attenuators (i.e., JERS-1 SAR employs 0, 1, 2, 4, 8, and 16 dB attenuators to provide attenuation from 0 dB to 31 dB in 1 dB steps). In the in-flight configuration, those attenuators can not be measured under saturation-free conditions because SAR always operates in the AGC mode and the resultant data are slightly saturated. We assume that the AGC gain gradient is the same as the STC gain gradient. The AGC can be modeled by

$$G_{AGC}(T) = 10^{-K(T)/10} \cdot G_{LNA0}, \tag{6.6}$$

where G_{LNA0} is the receiver's gain.

Saturation

The saturation rate, $\overline{S_a}$, can be measured from the raw data as follows [10]: First, an image is segmented into small pieces, each of which is 512 pixels in range and 64 pixels in azimuth. Second, a normalized histogram, $h_m[i]$ with i = 0 to 7, is measured for each segment. Since the histogram $h_m[i]$ for i = 1 to 6 is Gaussian distributed, we have a following relationship:

$$\int_{0.5}^{6.5} \frac{1}{\sqrt{2\pi}\sigma} e^{-\frac{(x-\mu)^2}{2\sigma^2}} dx = \sum_{i=1}^{6} h_m[i]. \tag{6.7}$$

Because μ is a measurement, a standard deviation σ can be determined by the iterative way. Finally the saturation rate can be obtained by

$$\overline{S_a} = 1 - \int_{-0.5}^{7.5} \frac{1}{\sqrt{2\pi}\sigma} e^{-\frac{(x-\mu)^2}{2\sigma^2}} dx. \tag{6.8}$$

Antenna elevation pattern

The antenna elevation pattern (AEP) has been determined in the annex of Chapter 4 using Amazon rain forest images (see also [6] , [7] and Eq. (4AN-9)).

$$10\log_{10} G_{ele}(\phi) = a(\phi - \phi_0)^2 + b + c(\phi - \phi_0)^4 \tag{6.9}$$

a = -0.39971	Standard Deviation = 0.0372
c = -0.00133	Standard Deviation = 0.0072
ϕ_0 = 34.91	Standard Deviation = 0.16 degrees

6.3 Validation

6.3.1 Uniformity test by mosaicing

We used the Amazon images to evaluate the cross track uniformity of σ^0 (or γ). Most of the flat Amazon areas are covered by rain forests, and the scattering from the dense forest is supposed to be volume scattering. Thus, σ^0 for the fully grown rain forests varies as $\cos\theta$, and γ should not change across the track. A two-path mosaic image is shown in Fig. 6-2. The images used for this mosaic are Paths from 415 to 416 and Rows from 300 to 301 (refer [12] for Path and Row). We can say that the calibration was performed so well that intensity difference can not be identified at the boarders of the four individual images.

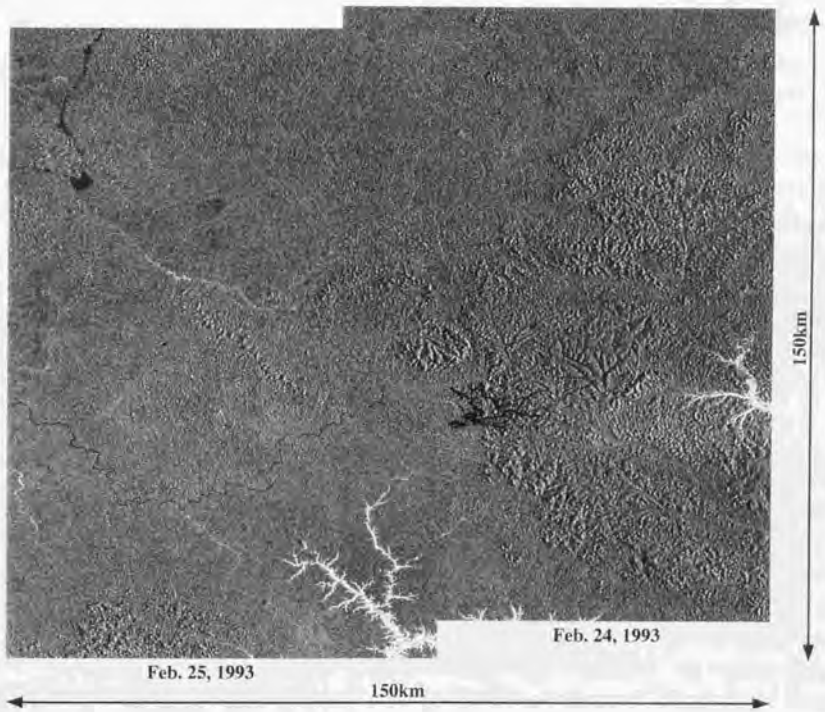

Fig. 6-2 Two-path SAR mosaic

6.3.2 Calibration factors

Next, we calculated the calibration factors for these SAR images by using two calibration methods, the peak method and the integral method [3], [8]. The calibration factors, CF_{peak} and CF_{int} are defined as follows:

$$CF_{peak} \equiv \frac{\sigma_{ARC} \sin\theta}{\rho_a \cdot \rho_r \cdot \{P(0,0) - P_{back} - P_{noise}\}} \quad (6.10)$$

$$CF_{int} \equiv \frac{\mathbf{c} \quad \sigma_{ARC} \sin\theta}{\iint_A \{P(x,y) - P_{back} - P_{noise}\} dxdy} \quad (6.11)$$

where σ_{ARC} is the radar cross section of the ARC, P(x, y) is the two-dimensional impulse response function, x (y) is the two-dimensional coordinates, P_{back} is the background power, P_{noise} is the receiver noise, A is the integration area, ρ_a and ρ_r are the resolutions in azimuth and range, and θ is the incidence angle. Note that we calibrated the input-output relationship of the ARC using a signal generator and a spectrum analyzer.

We used the fifteen impulse responses of the non-frequency shifted ARCs to calculate the calibration factor. Each impulse response is eight-times FFT-interpolated, then the azimuth resolution, range resolution, and the CF were calculated. To eliminate the long-term change of the SAR sensitivity, CFs were sorted in the time order and the change rate of -1 dB/3 years was corrected. Fig. 6-3 shows that 1) the two methods yield similar errors in CF, though the integral method is slightly better than the peak method (i.e., error of the peak method is 0.7 dB and that of the integral method is 0.6 dB), 2) CFs do not depend on the slant range although the ARCs were deployed in near and far ranges, and 3) the range dependency of the SAR image is well calibrated. We also present the distribution of the azimuth and range resolutions in Fig. 6-4. This shows that resolutions are almost equal to the theoretical limits.

6.3.3 Evaluation of measured σ^0

SAR image responses from the ARCs and corner reflectors were converted to σ^0 by using (6.4) and the calibration factors. They were then compared with the true values, which are the radar cross section normalized by a pixel area. We used seventeen responses from ARC and the nine from the 2.4 m trihedral CRs. The integral method and the peak method were used to calculate each pixel's energy. The ARC had 42 dBm^2 of radar cross section and the CR had 34 dBm^2 of radar cross section. We searched for a darker target with a known radar cross section, but, we could not find any. We evaluated the measured σ^0 by using two factors, the radiometric accuracy (R_error) and the slope. R_error is defined by

$$R\_error = \sqrt{\left\langle \left(\sigma_i^0 - \sigma_{truth}^0\right)^2 \right\rangle}, \quad (6.12)$$

where σ^0_i is the estimated normalized radar cross section of the i^{th} ARC or CR, and σ^0_{truth} is the theoretical value for the ARC (25.9 dB) and CR (17.9 dB).

The slope is a multiplicative factor to σ^0_{truth} so the summation of the squared difference between σ^0 and σ^0_{truth} is minimized. The measured radiometric accuracies and the slopes are summarized in Table 6-2. This shows that the radiometric accuracy satisfies the requirement given in Table 6-1 and the integral method showed better accuracy and linearity than the peak method.

6.3.4 Error Budget

We estimated the error budget for the calibration factors and the measured σ^0. The antenna elevation pattern required an accuracy of 0.1 dB to eliminate the stripes at the border of two path images. The calibration factor is affected by the instabilities at the ARC and SAR receiver, as well as by the speckle and receiver noise. The variance is

$$Var(CF) \equiv Var\left(\iint P_C - P_{rec} - P_{clutter} dA\right) + Var\left(G_{ant}^2\right) + Var\left(\sigma_{ARC}\right) + Var\left(G_{REC}\right). \quad (6.13)$$

where the first term on the right side depends on the ARC's signal-to-clutter ratio (SCR), and the representative value at SCR of 20 dB is 0.5 dB [8]. The CF is not calculated in saturation because the saturation degrades the accuracy. Based on the estimation shown in Table 6-1, CF could be determined with an accuracy of 0.9 dB. The variance of σ^0 is given by

$$Var\left(\sigma^0\right) \equiv Var\left(P_C - P_{rec} - P_{sat}\right) + Var\left(G_{ant}^2\right) + Var(CF) + Var(A) + Var(G_{REC}). \quad (6.14)$$

We show the expected variance of σ^0 for four cases in Table 6-1: 1) saturation-free case for clutter (SCR = 1), 2) saturation case for clutter (SCR = 1) corrected by this study, 3) saturation case for clutter (SCR = 1) corrected by the previous method, 4) saturation case for brighter target (SCR = 10) corrected by this study, 5) saturation case for brighter target (SCR = 10) corrected by the previous method. The terrain slope correction is only required for the high and moderate leaf area, and no correction is required for the ocean and flat areas.

Table 6-1 Error budgets

Case		This study	This study	Previous	This study	Previous
Contents	Var (CF)	Var (σ^0)	Var (σ^0)	Var (σ^0)	Var (σ^0)	Var (σ^0)
Condition(Sa)	0%	0%	20%	20%	20%	20%
SCR		1	1	1	10	10
P_C-P_{rec}-$P_{clutter}$	0.5	-	-	-	-	-
P_C-P_{rec}-P_{sat}		0.6	1.7+(+0.6)	1.7+(-1.5)	0.7 + (0)	1.7+(-2.0)
G_{ant}^2	0.2	0.2	0.2	0.2	0.2	0.2
σ_{ARC} 2)	0.5	-	-	-	-	-
G_{REC} 3)	0.5	0.5	0.5	0.5	0.5	0.5
A 1)	-	0.2	0.2	0.2	0.2	0.2
CF	-	0.9	0.9	0.9	0.9	0.9
	-					
Total (dB)	0.9 (0.0)	1.2 (0.0)	2.0 (+0.6)	2.0 (-1.5)	1.3 (0)	1.3+(-2.0)

0) Total error consists of the random error (dB) and (the bias error (dB)).

1) Not applicable for the flat land and the ocean. High-and moderate-leaf areas should be applied.

2) Stability of ARC.

3) Stability of SAR.

Sa Stands for the saturation rate and 20% is one of the serious saturation conditions. Saturation generates bias noise.

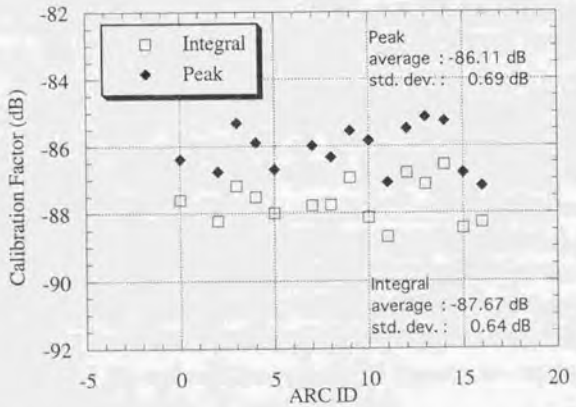

Fig. 6-3 Satiability of the two calibration factors derived from the peak method and the integral method.

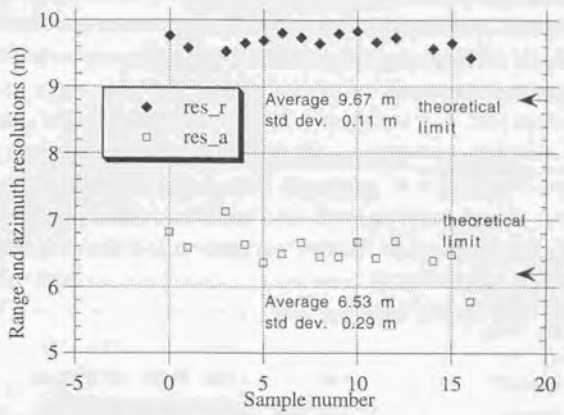

Fig. 6-4 Range and azimuth resolutions for the full-resolution images.

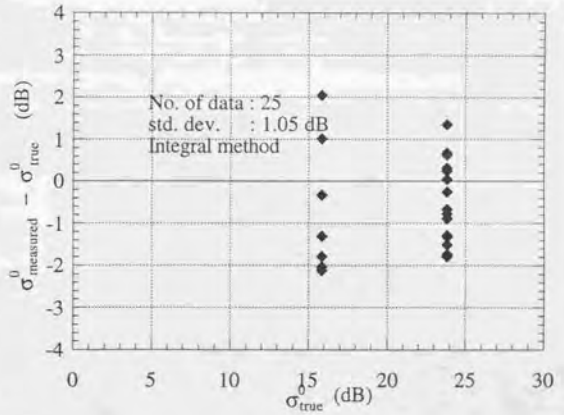

Fig. 6-5 Validation of the σ^0 using ARCs and corner reflectors. Integral method was used to calculate the energy contained in a pixel.

6.4 Image Quality

The SAR image quality using point targets and distributed targets has been measured following the CEOS recommendation [4], [5] and is summarized in Table 6-2. The impulse response function for the active radar calibrator is shown in Fig. 6-6. These results show that the JERS-1 SAR image processed by the range Doppler processor designed and manufactured by the author produces well-qualified image data.

Table 6-2 Image quality of JERS-1 SAR data

Item	Azimuth	(Std Dev)	Specification	Range (σ)	Specification
Resolution	6.5m	(0.3)	6.1	9.6 (0.1)	8.9
PSLR	-15.56 dB	(5.9)		-15.53 (5.2)	
ISLR	-8.70 dB	(4.9)			
Ambiguity	22 dB	-	20.0 dB		
G-Error	-40.0m			-104.0m	111m(RSS)
Error of CF	0.6 dB (Integral)		<0.9 dB	0.7 dB (Peak)	< 0.9 dB
R-Error	1.1 dB (Integral)		<1.2 dB	1.4 dB (Peak)	< 1.2 dB
Slope	1.0025			1.2436	
Uniformity	0.2 dB (1 sigma)			0.10 dB	< 0.1 dB
Saturation	0%				
Interference	27%				

Remarks SAR images were acquired in the single transmitter mode (325 W). Resolution, PSLR, and ISLR were calculated by evaluating the impulse responses from ARCs.

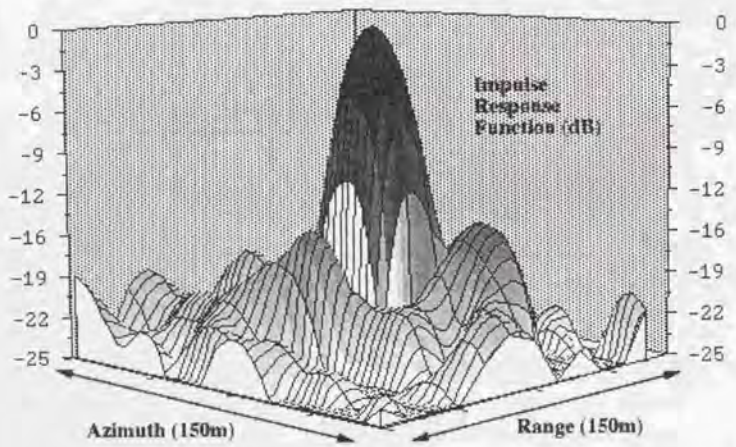

Fig. 6-6. Three-dimensional view of the impulse response function of the corner reflector deployed at Niigata Test Site on May 24, 1993.

6.5 Interference Analysis and Correction

Interfering signals from ground radars sometimes seriously degrade the SAR image quality. L-band is widely used for ground communications, Global Positioning System (GPS), airline traffic controlling systems, and spaceborne remote sensing. According to the statistical evaluation of images processed in Japan and other countries [9], [11], 27% of the processed images are degraded by these interference signals. The degradation occurs in several forms. Very strong bright lines appear over several contiguous range lines and look like a white area. We call these white areas "bright bands." The target is masked by these bright lines (see Fig. 6-7-c)). The appearance has a regional dependency. It is statistically recognized that eastern Hokkaido, Tokyo and Kanto, Chiba, Osaka, Kobe, and Hiroshima are most seriously affected. The interference could be eliminated experimentally, but not operationally because of the lack of knowledge about the complex power spectrum of the interference signals. We next consider the conditions under which these bright bands appear and propose a method to eliminate them.

6.5.1 Condition for bright band appearance

The bright bands are visible at the raw data and the correlated data. We then estimate the transmission power of the interference signal in two power levels, 1) raw data power and 2) correlated signal power.

Comparison of the correlated signal power

The interference signal is not correlated with the SAR reference signal. The correlative signal power is increased by "n^2," and the non-correlating signal power is increased by "n." Therefore, a comparison of the correlated signal power for the natural target and that for the interference signal gives the following inequality:

$$\frac{P_t G_t}{4\pi R^2}\frac{G_s \lambda^2}{4\pi} Ln \geq \frac{P_S G_S}{4\pi R^2}\sigma^0 A \frac{1}{4\pi R^2}\frac{G_s \lambda^2}{4\pi} L^2 n^2, \qquad (6.15)$$

where P_S is the SAR transmission power; G_S is the SAR antenna gain; P_t is the radar transmission power; G_t is the radar antenna gain; R is the slant range; λ is the wavelength; L is the atmospheric propagation loss; σ^0 is the NRCS of the target; and A is the pixel area (12.5 m x 12.5m). Equation (5.16) can be rewritten by

$$P_t G_t \geq \frac{P_S G_S}{4\pi R^2}\sigma^0 ALn. \qquad (6.16)$$

If the ground radar's antenna pattern is uniform ($1/4\pi$), its transmission power can be calculated. It depends on the target's σ^0. If σ^0 is -10 dB as for a natural target, forest and

grass land, P_t should exceed 19W. If σ^0 is larger than 10 dB as for the brightest target, such as a building or trihedral corner reflector target, P_t should exceed 1900W. The urban SAR correlated images for Tokyo, Hiroshima, and so on, are seriously affected by the bright bands and covered images can not be recognized at all. Therefore, we should pick σ^0 as 10 dB.

Comparison of the raw signal power

$$\frac{P_t G_t}{4\pi R^2}\frac{G_s \lambda^2}{4\pi} G_{rec} \geq \frac{(0.51)^2 \cdot 2}{50} \qquad (6.17)$$

where G_{rec} is the receiver gain (it was 78 dB when the bright bands appeared); 50 is the impedance of the SAR (ohms); and 0.51 is the maximum voltage of the saturated SAR raw data. The left side is the received raw data power at the input port of the ADC, and the right side is the saturated power level. This inequality implies that the transmission power should exceed 1440 W. From these two estimations, it is concluded that the peak transmission power may exceed 1440 W or 1900 W. This calculation can be applied for both pulsed radars and CW radars.

6.5.2 Correcting the contaminated signal

We next consider how to eliminate the interfering signal from the correlation. The raw signal power spectrum is not unique; i.e., it has different forms in time. One correction method is to 1) divide the whole image into several segments (i.e., 1024 pulses), 2) convert the data in the frequency domain, 3) identify the frequency bin which may be affected by the interference by comparing the power spectrum with theoretical values, and 4) entering zero values for the interference points. Sample images are shown in Fig. 5-17-c and d for the uncorrected and corrected images. Perfect correction is not possible. However, most of the bright bands may be eliminated and the image made useful.

6.6 Conclusions

This chapter has discussed the calibration of the JERS-1 SAR. We 1) have shown a method to determine the STC and AGC gain models, 2) have performed the mosaicing of four SAR images to evaluate the cross track variation, 3) have calculated the calibration factors in two ways, peak method and integral method, and verified that the measured σ^0 is obtained with an accuracy of 1.1 dB, 4) have obtained the error budgets for σ^0 measurement at several saturation conditions, 5) have calculated the image quality of the SAR data, and finally 6) have shown a method to eliminate the interfered signals.

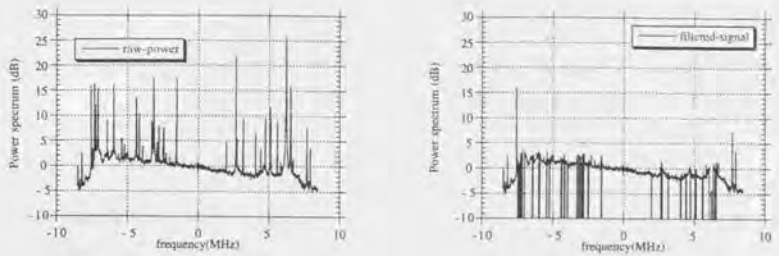

a) Power spectrum of raw data

b) Corrected power spectrum

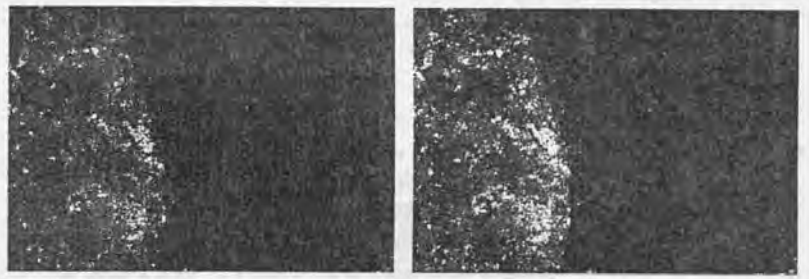

c) noise is not removed

d) noise removed

Fig. 6-7. Noise was reduced in the interference signal; a) shows the power spectrum of the raw data; b), the power spectrum of the filtered data for which zero value is added for the spike points; c), the SAR correlated image without any correction; and d), the SAR correlated image after noise has been filtered.

References

[1] M. Shimada, M. Nakai, and S. Kawase, "Inflight Evaluation of L band SAR of Japanese Earth Resources Satellite-1," Adv. Space Res. vol. 14, no. 3, pp. 231-240, 1994.

[2] M. Shimada, M. Nakai, and S. Kawase, "Inflight Evaluation of L band SAR of JERS-1," Canadian Journal of Remote Sensing, vol. 19, no. 3, pp. 247-257, 1993.

[3] A. L. Gray, P. W. Vachon, C. E. Livingstone, and T. I. Lukowski, "Synthetic Aperture Radar Calibration Using Reference Reflectors," IEEE Trans. Geosci. Remote Sensing, vol. 28, no. 3, pp. 374-383, May 1990.

[4] D. Massonnet, Radar image quality white paper CEOS SAR/CAL/VAL working group (draft), (1992).

[5] GEC-Marconi Remote Sensing Group (Under ESA contract), SAR data quality assessment and rectification, Final report Vol. 2, (1988)

[6] M. Shimada and A. Freeman, "A Technique for Measurement of Spaceborne SAR Antenna Patterns Using Distributed Targets," IEEE Trans. Geosci. Remote Sensing, vol. 33, no. 1, pp. 100-114, Jan. 1995.

[7] M. Shimada, "Determination of the antenna pattern of JSAR of JERS-1," CEOS CAL/VAL SAR workshop in ESTEC, ESA WPP-048, pp. 185-207, 1993.

[8] L. M. H. Ulander, "Accuracy of Using Point Targets for SAR Calibration," IEEE Trans. on Aerospace and Electronic Systems, vol. 27, no. 1, pp. 139-148, Jan. 1991.

[9] M. Shimada, "A report on the JERS-1 SAR images interferenced by the ground radar (Japanese)," NASDA internal report, HE-93048, July 12, 1993.

[10] M. Shimada, "Radiometric Correction of Saturated SAR Data," IEEE Trans. Geosci Remote Sensing, 1998, in press.

[11] M. Shimada, et. al., "Removal of the interferences appeared within the SAR images," submitted to COSPAR '98.

[12] M. Shimada, T. Nagai, and S. Yamamoto, "JERS-1 Operation Interface Specification," NASDA document, HE-89033, Nov. 7 1991 revision-3.

CHAPTER 7 CORRECTION OF ERROR IN σ^0 DUE TO TOPOGRAPHIC SLOPE UTILIZING SAR INTERFEROMETRY

7.1 Introduction

While σ^0 is defined as a unit-area quantity, the flat-earth-corrected σ^0 deviates from the true σ^0 that is corrected for the local gradients in two ways. First, the antenna elevation pattern is incorrectly estimated for the target position. Second, the tangential plane at the target area differs from that on the flat earth. The first way affects low-altitude SARs (i.e., airborne SARs) more. The second affects both airborne and spaceborne SARs [1], [2].

Zyl et. al. [1] first published error analyses for the airborne SAR (AIRSAR) and the spaceborne SAR (ERS-1 AMI) using a digital elevation model (DEM) prepared on the ground. Ulander [2] first proposed the use of the SAR interferometry for this correction. He described how the slope correction can be performed for a non-singular area, which excludes the layovers. His method uses the zero-padded FFT to estimate the two-dimensional local gradients, and the related error estimates. He also pointed out the importance of using the two-dimensional surface gradients for calculating the local surface normal vector.

In this chapter, we develop an improved method using the SAR interferometry technique to derive the slope correction factor. Two factors are known to influence the slope correction factor: the estimation of the local instantaneous frequencies which takes very much computation time for the FFT and the accuracy of the restituted orbit vectors. We have improved these two points by employing fast processing for the frequency calculations (not using the FFT estimation) and by constructing an error model including phase measurement error and the satellite position errors. We have applied this method to correct JERS-1 SAR images and achieved slope correction with an accuracy of around 0.3 dB.

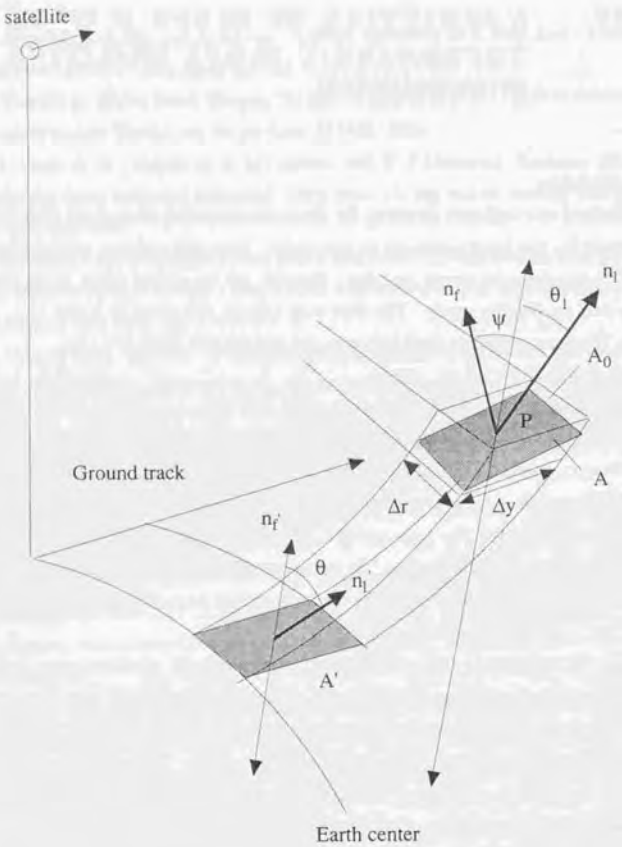

Fig. 7-1. Slope effect (A_0 is the pixel area made by a slant range distance (Δr) and azimuth distance (Δy); A', the surface area projected on the ellipsoid; and A, the pixel area tangential to the topography.)

7.2 Theory

7.2.1 Slope Correction Factor

Because the disturbance from the atmosphere is less, it can be assumed that a SAR pixel is composed of the scatterers existing on a tangential surface intercepted by two adjacent slant range planes and two azimuth planes (Fig. 7-1). We define the area of this tangential pixel as A, and the radar cross section of this area as σ. The true normalized radar cross section σ_t^0 is then given by

$$\sigma_t^0 = \frac{\sigma}{A} . \tag{7.1}$$

Next, we assume the slant range pixel area, which is enclosed by slant range scale of Δr and azimuth scale of Δy (i.e., $A_0 = \Delta y * \Delta r$) to be A_0, $\mathbf{n}_f$ to be the local normal vector at the point P, and $\mathbf{n}_l$ to be the tangential vector, then (7.1) can be expressed by

$$\sigma_t^0 = \frac{\sigma}{A_0}\cos\psi , \tag{7.2}$$

where

$$\cos\psi = \mathbf{n}_f \cdot \mathbf{n}_l = \frac{\sin\theta_l - \cos\theta_l \cdot \dfrac{\partial z}{\partial x}}{\sqrt{\left(\dfrac{\partial z}{\partial x}\right)^2 + \left(\dfrac{\partial z}{\partial y}\right)^2 + 1}}, \tag{7.3}$$

$$\mathbf{n}_f = \frac{\left(-\dfrac{\partial z}{\partial x} \quad -\dfrac{\partial z}{\partial y} \quad 1\right)^t}{\sqrt{\left(\dfrac{\partial z}{\partial x}\right)^2 + \left(\dfrac{\partial z}{\partial y}\right)^2 + 1}}, \tag{7.4}$$

$$\mathbf{n}_l = \left(\cos\theta_l \quad 0 \quad \sin\theta_l\right)^t. \tag{7.5}$$

Here θ_l is the local incidence angle at P; x is the ground range perpendicular to the satellite path; y is the ground range along the satellite path; z is the height perpendicular to the Earth ellipsoid's surface; ψ is the angle between the local surface normal vector and the slant range pixel's normal vector; and ^{t} denotes the transverse vector. If we do not know the local gradient vectors ($\mathbf{n}_f$) at P, we must assume that z = 0, and we obtain the wrong normalized radar cross section (σ_e^0) as

$$\sigma_e^0 = \frac{\sigma}{A_0}\sin\theta . \tag{7.6}$$

The ratio of σ_t^0 to σ_e^0 is defined as the slope correction factor (SCF)

$$SCF \equiv \frac{\cos\psi}{\sin\theta} . \qquad (7.7)$$

We have made a simulation to estimate how the two-dimensional local slope affects the SCF. In this simulation, we have assumed that the target is composed of a single sinusoidal mountain with a peak height of 8 km over a base of 40 km and that the satellite flies at a height of 700 Km and observes with incidence angles of 20, 30, 40, and 50 degrees at the image center. Fig. 7-2 shows the result of the simulation. We see in the figure that the SCF is smaller on the far mountain side, and larger on the near mountain side; that SCF corrects more for the far mountain side and suppresses the near mountain side; and that it varies more in an image for smaller incidence angle SAR. For the incidence angle of 40 degrees, SCF takes the maximum value of 1.7 dB ($10*\log_{10}1.5$) at x = 10 Km, and takes that of 3.5 dB ($10*\log_{10}2.25$) for 20 degrees. The larger incidence angle SAR is less affected by the terrain gradient than smaller incidence SARs. Note that the negative SCF means that the area is laid over, and the SCF between 0.0 and 1.0 is for foreshortened areas.

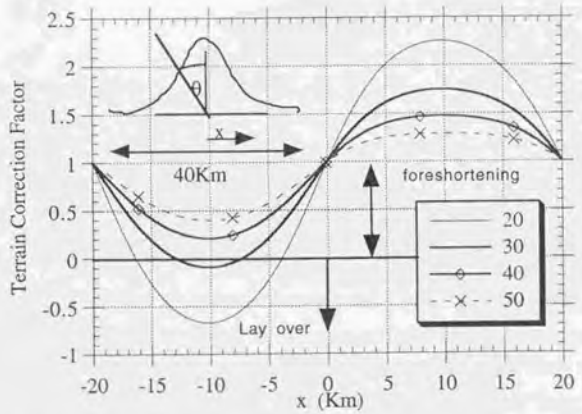

Fig. 7-2 SCF for a sinusoidal mountain with a peak height of 8 Km and base of 40 Km. Four different incidence angle cases are examined. Negative SCF indicates the area is overlaid. SCF between 0 and 1 is the foreshortened area.

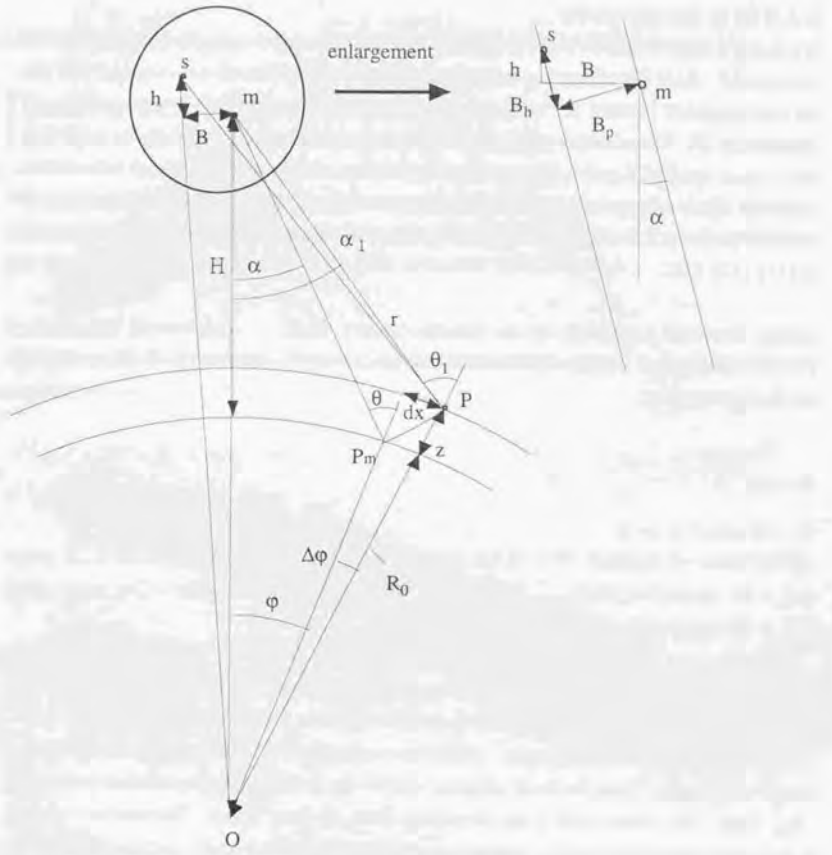

Fig. 7-3. Coordinate system of interferometric SAR.

7.2.2 SAR interferometry

We derive a slope correction factor using the SAR interferometry technique, and also derive its error model. SAR interferometry utilizing the phase information of two complex data has become a robust method for measuring the Earth (planetary) surface topography and deformation [3]. The accuracy of the measurement depends on the target's temporal properties, SAR signal quality, baseline distance, co-registration of two images, orbital information accuracy, signal propagation delay, unwrapping, etc. Errors related to the first three (target's temporal property, SAR signal quality, and baseline distance) have been precisely investigated in [11], [12], [13].

Height gradient estimated by the interferometry SAR

The flat-earth-surface corrected phase difference (ϕ) of the two interfering SAR data at point P can be expressed by:

$$\phi(r,y) \equiv \frac{4\pi}{\lambda}\left\{\frac{(B_p+\Delta B_p)z}{r\cdot\sin\theta}+\Delta B_h\right\} \tag{7.8}$$

$$B_h = B\cdot\sin\alpha + h\cdot\cos\alpha \tag{7.9}$$
$$B_p = B\cdot\cos\alpha - h\cdot\sin\alpha$$

$$\Delta B_h \equiv \Delta B\cdot\sin\alpha + \Delta h\cdot\cos\alpha \tag{7.10}$$
$$\Delta B_p \equiv \Delta B\cdot\cos\alpha - \Delta h\cdot\sin\alpha$$

where parameters without Δ are the true values; B_p is the perpendicular baseline distance; B_h is the horizontal baseline distance; B is the horizontal distance; h is the vertical distance; λ is the wavelength; α is the off-nadir angle; r is the slant range between SAR and the point P; z is the height of the point P from the Earth ellipsoid; and θ is the incidence angle at the Earth ellipsoid (Fig. 7-3). The values with Δ are deviations from the true values. Because the orbital information contains errors (i.e., several tens of meters for JERS-1 SAR), and the orbit cannot be sufficiently corrected even by intensively canceling the external phase patterns, the above phase difference still contains some errors. We assume that the surface does not move during the two data acquisitions. ϕ is a two-dimensional function of slant range (r) and azimuth ground range (y). We consider the partial differentiation of ϕ in range. From (7.8), we have

$$\frac{\partial\phi}{\partial r} \equiv \frac{4\pi}{\lambda r\cdot\sin\theta}\left\{(B_p+\Delta B_p)\cdot\frac{\partial z}{\partial r}+\Delta B_p\right\}, \tag{7.11}$$

and

$$\frac{\partial z}{\partial r} \equiv \frac{1}{B_p+\Delta B_p}\left(\frac{\lambda r\cdot\sin\theta}{4\pi}\frac{\partial\phi}{\partial r}-\Delta B_p\right). \tag{7.12}$$

Combining the azimuth components, the two dimensional height gradients are given by

$$\left(\frac{\partial z}{\partial r}\quad\frac{\partial z}{\partial y}\right)' \equiv \frac{r\sin\theta}{B_p+\Delta B_p}\frac{\lambda}{4\pi}\left(\frac{\partial\phi}{\partial r}\quad\frac{\partial\phi}{\partial y}\right)' - \frac{\Delta B_p}{B_p+\Delta B_p}(1\quad 0)'. \tag{7.13}$$

We note from (7.13) that the flat-earth corrected phase difference gives the height gradient information without unwrapping, the orbital error causes an offset error in the gradient vector, and the offset depends on the ratio of the error to the true value ($\Delta B_p/B_p$).

Coordinate conversion

We convert the height gradient from the slant range coordinate system to the ground range coordinate system. Fig. 7-3 gives:

$$r^2 = (R_0+H)^2 + R_0^2 - 2(R_0+H)R_0\cos\varphi \tag{7.14a}$$
$$x = R_0\cdot\varphi \tag{7.14b}$$

where R_0 is the Earth radius at the satellite subpoint, and H is the height of the master orbit. Differentiating (7.14a), and manipulating it with (7.14b) gives

$$\frac{dx}{dr} = \frac{r-\{(R_0+z)-(R_0+h)\cos\varphi\}\cdot\partial z/\partial r}{(R_0+h)\sin\varphi}, \tag{7.15}$$

and

$$\frac{\partial z}{\partial x} = \frac{\partial z/\partial r}{\dfrac{\partial z/\partial r}{\tan\theta_1}+\dfrac{1}{\sin\theta_1}}, \tag{7.16}$$

where θ_1 is the local incidence at P depending on the height "z." Further analysis allows the following approximation:

$$\theta_1 \equiv \frac{R_0 z}{(R_0+H)r\sin\theta}+\theta, \tag{7.17}$$

where θ is the incidence angle on the ellipsoid. The approximation is valid within a maximum error of 0.017 degrees in the worst case for z = 8 km, r of 720 km, α of 36 degree, R_0 of 6378 km, and H of 568 km. Therefore, the local incidence angle (θ_1) can be approximated by the

global incidence angle (θ), and the gradient component in ground range can be well approximated by

$$\frac{\partial z}{\partial x} \cong \frac{\partial z/\partial r}{\frac{\partial z/\partial r}{\tan\theta} + \frac{1}{\sin\theta}}. \tag{7.18}$$

Here, we should note that this factor has lower and upper bounds as given by

$$-\frac{1}{\tan\theta} \le \frac{\partial z}{\partial x} \le \tan\theta. \tag{7.19}$$

7.2.3. Error analysis

We investigate the error caused by the phase measurement, variance of the slope correction factor, and the allowance of the orbit error for a slope corrected σ^0.

Variance of the instantaneous phase gradients (dϕ/dr and dϕ/dy)

We assume that the same amplitude complex function (f(r, y)) governs the two-dimensional phase behavior for several adjacent pixels. We then measure the phase gradient in range (for example) by the following operation:

$$\frac{\partial \phi}{\partial r} = \frac{1}{\Delta r}\tan^{-1}\left[\frac{\Im\{\mathbf{f}(r+\Delta r, y)\mathbf{f}^*(r,y)\}}{\Re\{\mathbf{f}(r+\Delta r, y)\mathbf{f}^*(r,y)\}}\right], \tag{7.20}$$

where Δr is the slant range difference between two pixels; $\Im$ stands for the imaginary part of the complex data; and $\Re$ stands for the real part. The maximum error in estimating dϕdr in MLE is bounded by Cramer-Rao as given by [14], [15]:

$$Var\left(\frac{\partial \phi}{\partial r}\cdot\Delta r\right) = \frac{6}{SNR\cdot N\left(N^2-1\right)}, \tag{7.21}$$

where SNR is the power ratio of the coherent components (fringe) and the noise component, given by Ulander [2] and Spagnolini [16]. Note that the above operation is done only for the two non-singular adjacent pixels which are selected by the residue operations [24]. In this case, we select N = 2. SNR is defined as the power ratio of the coherent signals to the non-coherent signals, and it is expressed by using the thermal decorrelation (μ_n), and the decorrelation (μ_c) for the temporal and spatial decorrelation [2] as follows:

$$SNR = \frac{N_1 2\mu_n^2\mu_c^2}{1-\mu_n^2}, \tag{7.22}$$

$$\gamma = \mu_n\mu_c, \tag{7.23}$$

where γ is the correlation coefficient defined by Zebker et. al. [12] as the absolute value of the normalized complex covariance between master and slave complex data, and N_1 is the number of looks. In (7.13), the second term on the right side is a constant, not a distribution parameter for each small image. The standard deviation of dzdr can be expressed by

$$\left(\sigma_{\partial z/\partial r} \quad \sigma_{\partial z/\partial y}\right)^t \equiv \frac{r\sin\theta}{B_p+\Delta B_p}\frac{\lambda}{4\pi}\frac{\sqrt{\left(1-\mu_n^2\right)6}}{\mu_c\mu_n\sqrt{2N_1N\left(N^2-1\right)}}\left(\frac{1}{\Delta r} \quad \frac{1}{\Delta y}\right)^t. \tag{7.24}$$

In the normal case in which N_1 is 400 and N is 2, the above standard deviations are much smaller than 1.0. The standard deviation of dzdx is calculated through a Taylor expansion of (7.17) by replacing dzdr by dzdr + a small perturbation as

$$\begin{pmatrix}\sigma_{\partial z/\partial x}\\ \sigma_{\partial z/\partial y}\end{pmatrix} \equiv \begin{pmatrix} \dfrac{\dfrac{1}{\sin\theta}}{\left(\dfrac{\partial z/\partial r}{\tan\theta}+\dfrac{1}{\sin\theta}\right)^2}\dfrac{1}{\Delta r} & 0 \\ 0 & \dfrac{1}{\Delta y}\end{pmatrix}\begin{pmatrix}\sigma_{\partial z/\partial r}\\ \sigma_{\partial z/\partial y}\end{pmatrix}. \tag{7.25}$$

Variance of cos ψ

For simplicity, we rewrite the height derivatives dzdx and dzdy by z_x and z_y, respectively. Because the standard deviations given in (7.25) are so small, we can assume that z_x and z_y distributes in Gaussian with the averages of $\overline{z_x}$ and $\overline{z_y}$ respectively. Replacing z_x by $\overline{z_x}+\Delta z_x$ and z_y by $\overline{z_y}+\Delta z_y$ in (7.3) and keeping the first order terms, we have

$$\cos\psi \equiv \overline{\cos\psi} + \left(\frac{\overline{z_x}\cdot\overline{\cos\psi}}{1+\overline{z_x}^2+\overline{z_y}^2} - \frac{\cos\theta}{\sqrt{1+\overline{z_x}^2+\overline{z_y}^2}}\right)\Delta z_x + \frac{\overline{z_y}\cdot\overline{\cos\psi}}{1+\overline{z_x}^2+\overline{z_y}^2}\Delta z_y. \tag{7.26}$$

Thus, the variance of cos ψ is calculated by

$$\sigma^2_{\overline{\cos\psi}} = \left(\frac{\overline{z_x}\cdot\overline{\cos\psi}-\sqrt{1+\overline{z_x}^2+\overline{z_y}^2}\cos\theta}{1+\overline{z_x}^2+\overline{z_y}^2}\right)^2\sigma^2_{\partial z/\partial x} + \left(\frac{\overline{z_y}\cdot\overline{\cos\psi}}{1+\overline{z_x}^2+\overline{z_y}^2}\right)^2\sigma^2_{\partial z/\partial y}. \tag{7.27}$$

Here, we used $\sigma_{\partial z/\partial x}$ and $\sigma_{\partial z/\partial y}$ for the variance of dzdx and dzdy, respectively.

7.2.4 Phase gradient calculation

The phase gradient estimation is a study to estimate the instantaneous spatial frequency in two-dimensional images. Several methods have been proposed both for the SAR era and for the signal and information theory era, and the advantages and disadvantages of each are compared [20], [21], [22]. The forward, central and backward finite difference methods are the most basic and less computer intensive. However, they may be easily affected by noise. In contrast, the least square method, Cross Wigner-Ville Distribution (XWVD), Maximum Likelihood Estimation (MLE), and Digital Fourier Transform are robust methods though impose a heavy computation load.

If the SNR of flat-surface-corrected fringes is extremely high, simple differentiation can provide the answer in a robust sense. If the SNR is smaller, we should select the time-consuming, computer-intensive method. As given by Rodriguez [13], the standard deviation of the phase difference (σ_ϕ) also depends on the coherence (i.e., sqrt($(1-\gamma^2)/(2N_1\gamma^2)$)). For the cases with $\gamma = 0.4$ (low coherence) and $\gamma = 0.6$ (high coherence), standard deviation becomes 0.08 radian and 0.047 radian respectively. We can start with this type of image. Finally, we pick the four hundred look (five times five pixels, each of which is composed of sixteen look fringes) for this processing.

One difficulty in dealing with the SAR phase difference is the residue which is a singular point in two-dimensional unwrapping. Because the phase difference is the wrapped within $-\pi$ and π, phase differentiation should consider the existence of the residue. The proposed method uses two adjacent phase differences which do not cross the branch cut proposed by Goldstein et al. [24]. The gradient over these pixels is interpolated using the gradient vectors calculated from the non-singular pixel pairs.

Table 7-1. Summary of the SAR images used for this evaluation (Mt. Fuji)

Date 1	Date 2	B_h	dh	B_p(m)	γ	γ_{max}	Contour
Sept. 7, 1995	Oct. 21, 1995	645.6	292.9	360.31	0.47	0.61	148.1

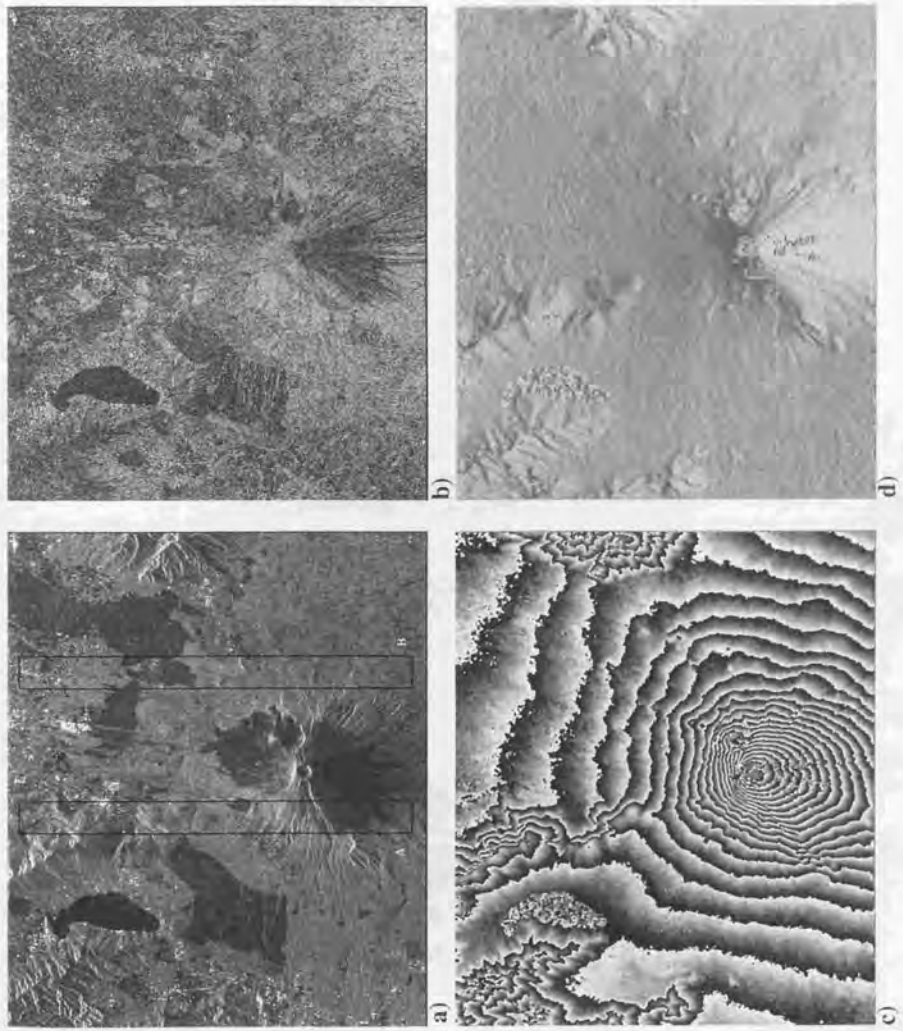

Fig. 7-4 The Mt. Fuji test area, a) amplitude image. The rectangular boxes are used for the accuracy evaluation; b), coherence map; c), flat earth corrected phase difference; d), Slope correction factor map; e), slope corrected σ^0 map using the proposed method; f), slope corrected σ^0 map using the GSI DEM

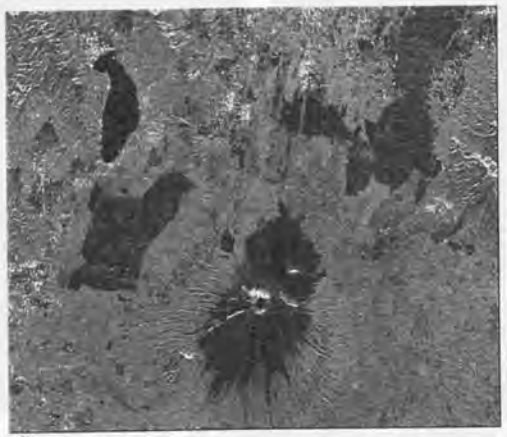

e)

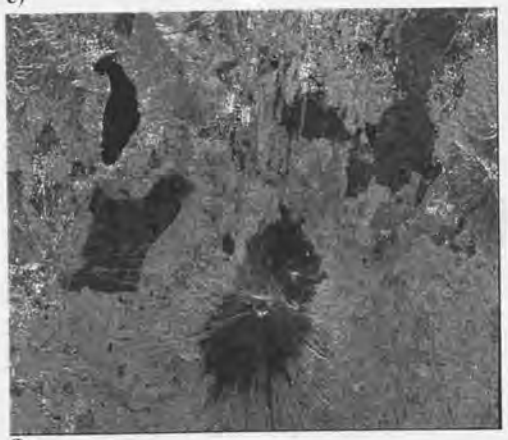

f)

7.3 Experiments

The proposed method has been examined using the JERS-1 SAR data. We have calculated the slope corrected σ^0 for the Mt. Fuji area and compared it with the one using the GSI DEM.

7.3.1 Test area

The Mt. Fuji area is appropriate for evaluating the DEM-related quantity because it contains various geological features such as mountains, lakes, flat land, grape plantations, fields, army training regions, and urban cities. The heights range from the lowest, 800 m at Yamanaka lake, to the highest, 3776 m at the top of the Mt. Fuji. The height difference is around 2900 m. Mt. Fuji is a monopole-like mountain with higher altitude, and the highest part is normally overlaid. The foothill area is quite wide and its gentle gradients simplify retrieving DEM except for the vegetated area.

Among the many available data pairs collected during the JERS-1 mission life (May 1992 to present, and the data acquired every 44 days), we picked the best data pair. They are 44 days apart in the autumn season (Sept. 7 1995 and Oct. 21 1995) and almost 360m apart as the perpendicular baseline distance. JERS-1 SAR interferometry requires a baseline distance (B_p) of less than 1 km for good interferograms (higher correlation), although the critical (theoretical) baseline is 6.5 km [4]. We selected the images satisfying this condition (Table 7-1). Branch cut trails were set using the residue method in order to find the differentiation path [8].

We selected a small rectangular area in the range direction for quantitative evaluation of the local incidence angle and the slope correction factor in comparison with the SGI DEM information. The area selected contains low, moderate, and high relief areas. The area size is 50 pixels in azimuth and 630 lines in range as shown in the rectangular box in Fig. 7-4a.

7.3.2 SAR processing and the Interferometry processing

We used the SAR processor developed by the author in adopting the range Doppler type [4]. Rectangular windows were applied in the range and azimuth correlation to achieve the best resolution. Range and azimuth reference functions were first generated in the time domain then converted to the frequency domain. This allows accurate generation of the reference function. The master and slave data were processed using the common Doppler frequency centroid, which was generated using the averaged satellite velocity vectors. The start address for the slave image processing was selected using the satellite telemetry to make the slave image overlaid onto the master data as large as possible.

Co-registration of the master and save image was conducted so that a wide area (200 pixel x 200 line) in the master image is referenced and the corresponding area was searched on the

slave image. This is called the first order co-registration process. The reference tie points were piled on the master image every several hundred pixels, and their corresponding coarse tie points were also found on the slave images. Fine co-registration points were searched in the slave image by using the covariance of the two amplitude images. A tie point found within the specified pixel/line allowances and with the covariance factor exceeding 0.2 was selected as a good tie point. The successfully selected tie points in the above procedure were used to form the continuos co-registration function which governs the master and slave images. The standard deviation of the difference between the co-registration function and the successfully selected tie points is normally less than 0.5 pixel. Here, the size of the pixel is 4.4 m in azimuth and 9 m in range.

After co-registration, the phase difference (ϕ) has been measured by the following operation:

$$\phi = \tan^{-1} \frac{\Im\left(\sum_{i=1}^{N} \mathbf{C}_i^m \cdot \mathbf{C}_i^{s*}\right)}{\Re\left(\sum_{i=1}^{N} \mathbf{C}_i^m \cdot \mathbf{C}_i^{s*}\right)}, \tag{7.28}$$

where $\mathbf{C}_i^m$ is the i^{th} complex full resolution data; the suffix "m" stands for master; and "s" for slave. ϕ has been wrapped and normally contains the high-frequency parallel component caused by the horizontal baseline distance. This component should be eliminated using the orbital data. However, the orbital determination error (60 m vertical, 40 m across track, and 180m along track; all those values are in three sigma's [5]) leaves the undesired low frequency component.

It can be removed by tuning either/both Δh or ΔB by using ground control points, analyzing the frequency gradients. However, it is very difficult to perfectly eliminate these frequency components. The output at this point gives the averaged flat earth corrected fringes (interferogram). This corresponds to the ϕ discussed in the earlier section.

7.3.3 Data examples and evaluation

A 16-look (eight looks in azimuth and two looks in range) slant range SAR amplitude image (square root of the correlation power) for the Mt. Fuji area is shown in Fig. 7-4a. This area contains various types of land features. In the mountainous area, we see many wrinkles and high relief areas. Most of the satellite side of the mountains looks brighter, and the opposite side looks dark. As shown in Fig. 7-4b, the flat foothills and low relief areas have a coherence of 0.4 or more, and the top of Mt. Fuji and its back side have lower coherence. The coherence of Lake Yamanaka is the lowest at around 0.3. The interferogram (ϕ map) is shown in Fig. 7-

4c. A four-hundred-look image reduces the additional noise and generates the phase uncertainty of around 2.7 degrees for $\gamma = 0.6$.

As shown in Fig. 7-4d, the slope correction factor produces gradient-dependent brightness for most of the area except for the overlaid and low coherence areas. The overlaid area is not visible and is not discussed here. The foreshortening area with high gradients is under sampled, and the range gradient does not show the exact value. The slope-corrected SAR data (amplitude data times square root of the slope-correction factor) is shown in Fig. 7-4f. Most of the high-relief areas in the mountain are corrected. Low-coherence areas and high-relief area, however, still have uncorrected brightness. For reference, the slope-corrected SAR data using the GSI DEM is shown in Fig. 7-4e. By comparing them, we see that the high-relief area still has uncorrected slope components.

We compare the slope correction factors calculated from this proposed method and from the conventional method using GSI DEM. The slope-correction factor is averaged along the azimuth direction for each range line within the rectangle areas (A and B) in Fig. 7-4a. The results are shown in Fig. 7-5, where the thick solid line is for the proposed method and the thin solid line with square is for GSI DEM. The theoretical and measured differences in Fig. 7-6 shows a good agreement. Standard deviation of difference in region A is 0.24 dB and that for B is 0.14 dB. The lines (solid and dashed lines) exhibit the better coincidence for regions B than for region A at the address of more than 500. This may be because that the water vapor distribution in A is less uniform than B.

From (7.13), ΔB_p should ideally be zero. However the reality is that the orbit determination error sometimes reaches several tens of meters especially for lower altitude satellites, such as JERS-1 [5]. We have evaluated the behavior of the slope correction factor due to the baseline estimation error. We have used the following parameter "ratio" for the evaluation:

$$ratio = 10 \log_{10}\left(\frac{\cos\psi'}{\cos\psi}\right), \tag{7.29}$$

where ψ' is the angle calculated from the erroneous satellite positions (from the $\Delta B_p + B_p$ instead of B_p). Fig. 7-7 shows that an evaluation parameter ($\Delta B_p / B_p$) should be less than +- 2% in order to make the error in slope correction factor less than 0.1 dB, and that the smaller incidence SAR has the smaller allowance for the existing B_p error ratio.

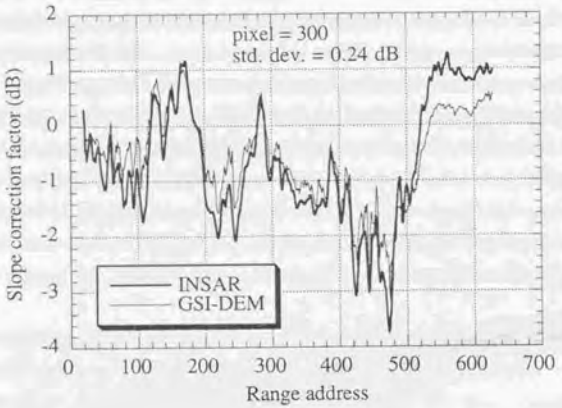

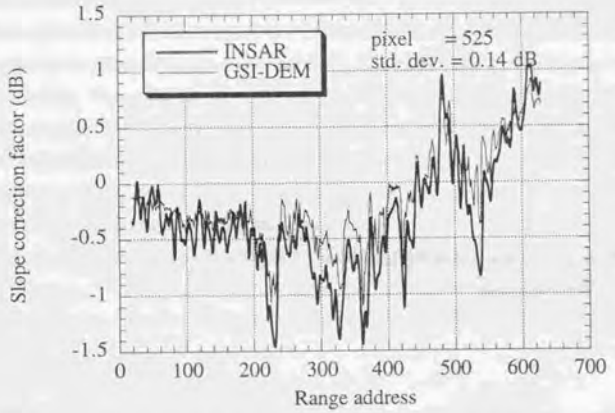

Fig. 7-5 Comparison of the slope correction factor between InSAR and GSI DEM. a) for A; b), for B

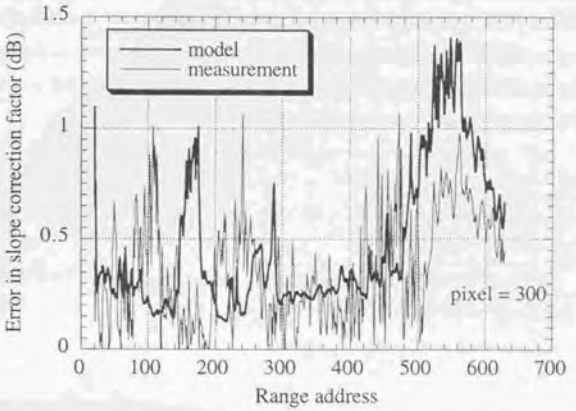

Fig. 7-6 σ^0 difference between this method and GSI-DEM and comparison with the theory.

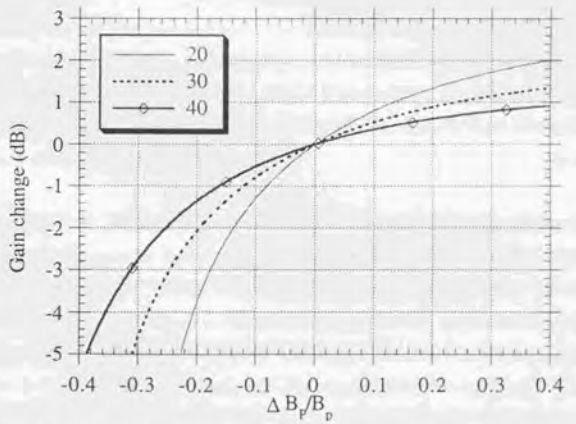

Fig. 7-7 Gain change due to the baseline estimation error.

7.3.4 Applicability of the proposed method

We evaluated the applicability of the proposed method to calculating the slope corrected σ^0 in comparison with the method using the ground measured DEM. The question is "how much pixel spacing is achieved by this method for a certain accuracy requirement?" Because the high or moderate leaf areas are only meaningful for the slope correction, we focus on those areas and calculate the number of looks which satisfy the given radiometric correction allowance. From (7.25) and (7.27), the minimal number of looks is given by

$$N_l \geq \frac{1}{\sigma^2_{\overline{\cos\psi}}} \frac{r^2 \sin^2\theta\left(1-\mu_n^2\right)}{B_p^2 \gamma^2 \left(1+\overline{z_x}^2+\overline{z_y}^2\right)^2} \left(\frac{\lambda}{4\pi}\right)^2 \cdot \left\{ \left(\overline{z_x \cos\psi} - \sqrt{1+\overline{z_x}^2+\overline{z_y}^2}\cos\theta \right)^2 \frac{\left(\frac{1}{\sin\theta}\right)^2}{\left(\frac{\overline{z_r}}{\tan\theta}+\frac{1}{\sin\theta}\right)^4} \frac{1}{(\Delta r)^2} + \left(\frac{\overline{z_y \cdot \cos\psi}}{\Delta y} \right)^2 \right\}. \quad (7.30)$$

Here, the correlation coefficient γ depends on the target's temporal change, baseline distance, and thermal noise of the SAR receiver, and the γ of JERS-1 SAR for the mountainous area can be empirically expressed by [4]

$$\gamma = 0.4 \cdot 10^{-B_p} + 0.2. \quad (7.31)$$

We calculated the minimal number of looks and the corresponding pixel spacings for two error requirements of 0.1 dB and 0.2 dB when z_x and z_y are 1.0, μ_n is 0.75, θ is 38 degrees, ψ is 50 degrees, Δr is 18 m, Δy is 36 m, r is 700 km, and λ is 23.5 cm. The results are shown in Fig. 7-8. It shows that:

i) The minimal number of looks increases as the perpendicular baseline decreases;
ii) Better accuracy requires a larger number of looks;
iii) The 50 m spacing is achieved for B_p exceeding 0.35 km and an error requirement of 0.2 dB;
iv) The 50 m spacing is not achieved for the error requirement of 0.1 dB.

Because the error in proposed method is random, a slightly larger value degrades the quality of the slope-corrected image. Thus, the maximum error must be 0.2 dB or less. For an error allowance of 0.2 dB, this method can perform as well as the ground DEM. If we require 0.1 dB, the ground DEM is superior to this method. The medium leaf or hilly area generally has a higher γ than the high leaf area, and the condition on the pixel spacing and the number of looks is relaxed.

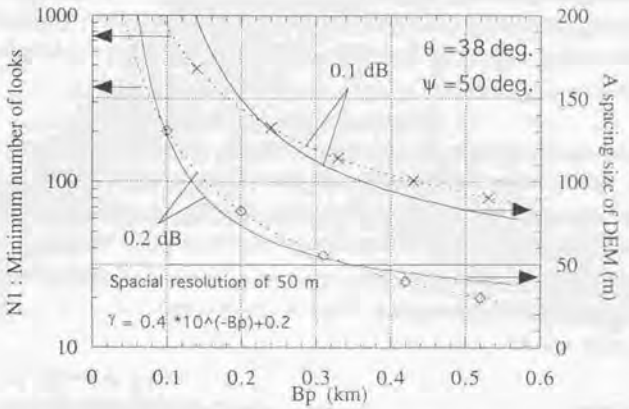

Fig. 7-8 Minimal number of looks (and corresponding resolution) vs. B_p.

7.3.5 Discussions

The flat-earth-corrected σ^0 generates large errors in a high-relief area. The correction of such errors using the surface gradient vector is crucial for terrain analyses based on σ^0. Most of the land area is not flat, but undulating or sometimes steepened due to the topography. Classification based on the normalized radar cross section requires a slope-corrected σ^0. Most of the global land is not well covered by high-resolution DEMs. NASA's global topography mission is the only existing plan for this.

After the DEM is prepared in a different way (not from the same SAR image), the SAR data and the slope-correction factor map generated from such an inconsistently generated DEM should be co-registered. Differences in the coordinate system require greater computing power for co-registration and requires linearization within the segmented areas. In contrast, the method proposed in this chapter has the advantages that the coordinate system has no difference between the SAR amplitude image and the slope correction map and co-registration does not become a problem. This method can also be applied to areas for which maps have not been prepared, i.e., Brazil, Central Africa, and Central Siberia. The disadvantages of the proposed method are that overlaid and low-coherence areas cannot be corrected and that surface wrinkles cannot be corrected in detail if the baseline is too small. Further analysis has revealed that the baseline distance error ratio $\Delta B_p/B_p$ should be less than 2% in order to achieve a slope correction error of less than 0.1 dB

The proposed method uses less processing time to perform corrections because the finite difference procedure is adopted to estimate the surface slope. This advantage is obtained if we deal with the averaged phase difference which minimizes a phase error. However, the residue point generates an inaccurate correction factor. The correction of those points should be further investigated.

The accuracy of the proposed method has been measured. One example shows that the error model was fully verified using the GSI DEM truth data. The estimated difference in σ^0 is around 0.3 dB. The accuracy thus becomes almost equal to the calibration accuracy requirement for σ^0 [9]. If the baseline distance is appropriately selected, this method can be used to correct SAR images. This method does not require the use of the ground-measured DEM, nor does it require phase unwrapping to obtain the height distribution.

7.4 Conclusions

In this chapter, we have presented a method to calculate the slope corrected normalized radar cross section. This method calculates the two-dimensional gradient using a SAR interferometry technique which does not require phase unwrapping. We have verified that such a slope-corrected σ^0 can be obtained with an accuracy of 0.2 to 0.3 dB when the interferometric condition is satisfied. It has been shown that the perpendicular baseline distance should be determined with an accuracy of the 2% for $\Delta B_p/B_p$ to generate a slope-corrected σ^0 of less than 0.1 dB accuracy. It has also been shown that the correction accuracy of this method does not exceed the ground DEM. If the spacing requirement or the radiometric requirement is relaxed to 100 m or 0.2 dB, the InSAR-based slope correction can be used.

References

[1] J. J. V. Zyl, B. D. Chapman, P. Dubois, and J. Shi, "The Effect of Topography on SAR Calibration," IEEE Trans. Geosci. Remote Sensing, vol. 31, no. 5, pp. 1036-1043, Sept. 1993.

[2] L. M. H. Ulander, "Radiometric Slope Correction of Synthetic -Aperture Radar Images," IEEE Trans. Geosci. Remote Sensing, vol. 34, no. 5, pp. 1115-1122, Sept. 1996.

[3] D. Massonnet and T. Rabaute, "Radar Interferometry: Limits and Potential," IEEE Trans. Geosci. Remote Sensing, vol. 31, no. 2, pp. 455-464, March 1993.

[4] M. Shimada, "JERS-1 SAR interferometry," submitted to IEEE Trans. Geosci Remote Sensing in June 1997.

[5] Communication with the Tracking Network Technology Department of NASDA's Tsukuba Space Center.

[8] J. Way, and E. A. Smith, "The Evolution of Synthetic Aperture Radar Systems and their Progression to the EOS SAR," IEEE Trans. Geosci. Remote Sensing, vol. 29, no. 6, pp. 962-985, Nov. 1991.

[9] A. Freeman, "SAR calibration: An overview," IEEE Trans. Geosci. Remote Sensing, vol. 30, no. 6, pp. 1107-1121, Nov. 1992.

[11] F. Li, and R. M. Goldstein, "Studies of Multibaseline Spaceborne Interferometric Synthetic Aperture Radars," IEEE Trans. Geosci. Remote Sensing, vol. 28, no. 1, pp. 88-97, Jan. 1990.

[12] H. Zebker and R. M. Goldstein, "Topographic Mapping From Interferometric Synthetic Aperture Radar Observation," JGR, vol. 91, no. B5, pp. 4993-4999, April 10 1986.

[13] E. Rodriguez, and J. M. Martin, "Theory and design of Interferometric synthetic aperture radars," IEEE proceedings-F, vol. 139, no. 2, pp. 147-159, April 1992.

[14] B. Boashash, "Estimating and Interpreting the Instantaneous Frequency of a Signal - Part 2: Algorithms and Applications," Proceedings of the IEEE, vol. 80, no. 4, pp. 540-568, April 1992.

[15] L. C. Palmer, "Coarse Frequency Estimation Using the Discrete Fourier Transform, " IEEE Trans. on Information Theory, vol. IT-20, pp. 104-109, Jan. 1974.

[16] U. Spagnolini, "2-D Phase Unwrapping and Instantaneous Frequency Estimation," IEEE Trans. Geosci. Remote Sensing, vol. 33, no. 3, pp. 579-589, May 1995.

[20] P. O'Shea, and B. Boashash, "Some Robust Instantaneous Frequency Estimation Techniques With Application To Non-stationary Transient Detection," Signal processing V: Theories and applications, pp. 165-168, Elsevier Science Publishers B.V., 1990

[21] David C. Rife, and R. R. Boorstyn, "Single-Tone Parameter Estimation from Discrete-Time Observations, " IEEE Trans. on Information Theory, vol. IT-20, no. 5, pp. 591-598, Sept. 1974.

[22] B. Boashash, P O'shea, and M. J. Arnold, "Algorithms for Instantaneous frequency estimation : A comparative study," SPIE vol. 1348, Advanced Signal Processing Algorithms, Architectures, and Implementations, pp. 126-148, 1990.

[24] R. M. Goldstein, H. A. Zebker, and C. L. Werner, "Satellite radar interferometry: Two-dimensional phase unwrapping," Radio Science, vol. 23, no. 4, pp. 713-720, July-Aug. 1988.

CHAPTER 8 CONCLUSIONS

This thesis has presented the results of investigations on the accuracy improvement of measuring the normalized radar cross section (NRCS) of earth surfaces using synthetic aperture radar data.

In Chapter 1, the background and the outline of this thesis have been introduced. We 1) have reviewed the need for earth monitoring by the synthetic aperture radar (SAR), 2) have described the SAR instrument and processing algorithms, 3) have introduced the definition and the properties of normalized radar cross section, 4) have shown SAR data interpretation examples and summarized the accuracy requirements for different observation targets, 5) have shown the SAR artifacts due to the incorrect SAR calibration, 6) have summarized the new SAR calibration procedure investigated in this thesis, 7) and finally have shown the outline of the thesis.

In Chapter 2, the preparative reviews have been given for the subsequent chapters. We 1) have shown the principle of SAR imaging, 2) have discussed the details of the SAR calibration, 3) have described the SAR system, SAR processor, and calibration instrument, and 4) have shown the current calibration accuracy.

In Chapter 3, a new radar equation has been theoretically derived for the correlated SAR power, which consists of backscattered signals from the terrain, receiver noise, redundancy noise at the analogue-to-digital converter (ADC), and the saturation noise at ADC. The correlated power is expressed by the signal-to-clutter ratio (SCR), signal-to-noise ratio (SNR), and the saturation rate (S_a). When the saturation rate becomes larger, the power loss increases proportional to S_a^2. For example, 20% of the saturation rate underestimates the power in -1.5 dB. A simulation has shown that the power loss can be successfully recovered regardless of the SAR gain mode, automatic gain control (AGC) or manual gain control (MGC). The method has been applied to the JERS-1 SAR data and has confirmed that the saturated image is corrected well.

In Chapter 4, a method to estimate the antenna elevation pattern of the inflight SAR has been investigated. The SAR data observed for the Amazon rainforest show the constant backscattering coefficient ($\sigma^0/\cos\theta$) over an image swath. Screening processing using χ^2 test has successfully extracted the similarly distributed area by excluding the different brightness area, rivers and mountain ridges. The least square method has determined the antenna elevation pattern. The method has been applied to the SIR-B antenna and determined the antenna elevation pattern with an accuracy of 0.1 dB. In the annex of the chapter, the JERS-1 SAR

antenna elevation pattern has been examined. More consideration on automatic gain controller (AGC) and sensitivity time control (STC) has been taken in the analysis. Eighteen Amazon SAR data sets have been analyzed, and the antenna elevation pattern has been derived. Worse SNR and the STC's steep gain change have made the standard deviation of the measurement as large as 0.1 dB.

In Chapter 5, the impulse response function (IRF) of the frequency-tunable active radar calibrator has been investigated. The IRF of the frequency-shifted ARC has been theoretically derived. The expression prescribes the location shift in azimuth and the decrease of the IRF's peak. The computer simulation has estimated the frequency dependency of the location shift, the decrease in the peak value of IRF, and the resolution decrease. Some of them have been compared with experimental results on the JERS-1 SAR. The following is the main conclusions: First, the location shift and the peak gain loss can be theoretically estimated with an accuracy of 4.2 m and 1.6 dB (a standard deviation), respectively. Second, the peak calibration method is affected by the broadened resolution and the decreased peak. Third, the integral method that is not sensitive to the defocusing should be used for the SAR calibration using a frequency-tunable ARC. Fourth, the frequency shift should be less than 40 Hz for the image evaluation in the case of L-band SARs.

In Chapter 6, a calibration of JERS-1 SAR has been described. we have applied the calibration method developed in the previous chapters to low-dynamic range SAR data, which is saturated in the near range region, and whose receiver is composed of a sensitivity time control (STC), an automatic gain control (AGC) and a low-bit-number analog-to-digital converter (ADC). We 1) have shown a method to determine the STC and AGC gains, 2) have performed the mosaicing to evaluate the cross track variation of the calibrated data, 3) have calculated the calibration factors in two ways, peak and integral methods, and verified that the measured σ^0 is obtained with an accuracy of 1.1 dB, 5) have obtained the error budgets for σ^0 measurement at several saturation conditions, 6) have calculated the image quality of the processed data, and finally 7) have shown a method to eliminate the interfered signals.

In Chapter 7, the radiometric slope correction of σ^0 using SAR interferometry has been investigated. The method calculates the two-dimensional gradient using the SAR interferometry technique which does not require phase unwrapping. We have verified that such a slope-corrected σ^0 can be obtained with an accuracy of around 0.3 dB when the interferometric condition is satisfied. It has been shown that the perpendicular baseline distance should be determined with an accuracy of the 2% to generate a slope-corrected σ^0 of less than 0.1 dB accuracy.

In this thesis, we have proposed the three new algorithms to improve the SAR calibration accuracy. They are 1) the new radar equation to describe the saturated and non-saturated SAR image data, 2) a method to estimate the antenna elevation pattern using the flat amazon rainforest data, and 3) a method to correct the slope effect on σ^0 using SAR interferometry. We have shown the effectiveness and limitation of the frequency tunable active radar calibrator by the theoretical and experimental approaches. We have verified that the proposed methods are very effective for calibrating the SAR data, and have confirmed that JERS-1 SAR data, which is saturated slightly and has lower SNR of around 5 dB, can be calibrated with an accuracy of 1.1 dB using the active radar calibrator and 2.4 m trihedral corner reflectors. It should be however noted that the proposed method is effective to decrease the bias error more than the current method but not for the random error. We have also confirmed that the slope error on σ^0 can be corrected with an accuracy of 0.3 dB.

Needs for the calibrated SAR data (σ^0) has been increasing recently. This is because 1) SAR can measure the earth surface reflectance of high resolution accurately and effectively, not depending on the weather condition neither solar irradiance condition; 2) the calibrated data can retrieve the geophysical information of the earth surfaces (e.g., biomass of the forest, types of the land utilization, sea-ice distribution, etc.), and 3) retrieval of the geophysical information is mandatory for the global understanding. Measurement accuracy for this application is required as less than between 1.0 dB and 3.0 dB, depending on the targets. As the future approaches to these goals, we require two more investigations on accuracy improvement. First, a method to effectively subtract the noise from the SAR data should be developed. Currently, the total power of signal and noise is calibrated and there is a problem to separate the signal power from it. If we find a method which subtracts the noise power component from the total power effectively, we can generate stripe-free SAR mosaic images. Second, a robust method to calculate the two-dimensional surface slope should be developed. As discussed in Chapter 7, the slope correction is mandatory for the SAR calibration. However, the singular points in the SAR image (e.g., layover, foreshortening, low coherence) loose the calculation accuracy. We expect that the phase unwrapping approach can solve the problem. We will also require investigation on the phase delay due to the local distribution of the water vapor and the determination of orbit vectors using the ground control points as to improve the calibration accuracy.

Acknowledgment

The author wishes to express his deepest gratitude to Prof. Haruto Hirosawa of the Institute of Space and Astronautical Science (ISAS), Prof. Sadao Fujimura of the University of Tokyo, Prof. Masao Sakauchi of Institute of Industrial Science (IIS), Prof. Kazuo Hotate of the University of Tokyo, Associate Prof. Akira Hotate of the University of Tokyo, and Associate Prof. Hiroyuki Morikawa of the University of Tokyo, for their guidance and encouragement in writing this thesis. A major part of this study was performed at Earth Observation Center (EOC) and Earth Observation Research Center (EORC) of National Space Development Agency of Japan (NASDA) between 1988 and 1997. The author is grateful for the support received from Dr. Tutomu Takashima, Mr. Takashi Moriyama, and Mr. Tasuku Tanaka of NASDA.

The author' SAR remote sensing studies started at Earth Observation Center of NASDA. The author would like to thank Mr. Noritaka Tanioka, and Mr. Seiichi Kawase for their encouraging this study. The author would like to thank Dr. Anthony Freeman, Dr. John Curlander, and Dr. Bruce Chapman for their technical support and valuable discussions on antenna pattern determination while he is conducting this study at Jet Propulsion laboratory (JPL) in 1990. The author also thanks to Dr. Yves Louis Desnos of ESTEC on the valuable discussion on the SAR calibration.

The author would like to express his special thanks to his colleagues, Ms. Hiromi Oaku, Dr. Ake Rosenqvist, Mr. Kazuo Isono and Mr. Yuuki Kawata for their valuable discussion, comments, and the numeric calculation. He also express his special thanks to Dr. Hiroshi Kimura of Gifu University for his valuable comments on SAR calibration and interferometry. He also thanks to Mr. Hitoshi Noumi, Mr. Minoru Murata, Ms. Ikuko Horie, and Mr. Masanori Miyawaki for their valuable comments on the SAR data analysis and the investigation of the SAR interferometry.

LIST OF PUBLICATIONS RELEVANT TO THIS STUDY

SAR calibration

1 M. Shimada, and A. Freeman, "A technique for Measurement of Spaceborne SAR Antenna Patterns Using Distributed Targets," IEEE Trans. Geosci. Remote Sensing., vol. 33, no. 1, January 1995, pp. 100-114.

2 M. Shimada, "Radiometric Correction of Saturated SAR Image," IEEE Trans. Geosci Remote Sensing, 1998, in Press.

3 M. Shimada, H. Oaku, and M. Nakai, "Calibration Using Frequency-Tunable Active Radar Calibrators," IEEE Trans. Geosci Remote Sensing, 1998, in press.

4 M. Shimada, M. Nakai, and S. Kawase, "Inflight Evaluation of L band SAR of JERS-1," Canadian Journal of Remote Sensing, vol. 19, no. 3, ISSN 0703-8992, Aug. 1993, pp. 247-258

5 M. Shimada and M. Nakai "Inflight Evaluation of L band SAR of Japanese Earth Resources Satellite-1," Adv. Space Res. vol. 14, no. 3, pp. 231-240, (1994), COSPAR, 1992.

6 M. Shimada, "Radiometric and Geometric Calibration of JERS-1 SAR," Advanced in Space Research, vol. 17, no. 1, pp. 79-88, 1996, COSPAR

7 M. Shimada, "Radiometric correction of the saturated SAR image," Proceedings of the CEOS SAR calibration workshop, 28-30, September, 1994, The University of Michigan, pp. 123-142.

8 M. Shimada, M. Nakai, "First result of the SAR characterization (in Japanese)," Technical Report of IECE SANE92-58 (1992-11)

9 M. Shimada, "An estimation of JERS-1's SAR antenna pattern using Amazon rain forest images," Proc. 1993 SAR Calibration Workshop, Noordwijk, The Netherlands, Sept. 1993, pp. 185-208.

10 M. Shimada, "Radiometric calibration accuracy on the AD conversion noise - estimation of the radiometric correction error due tot he ADC saturation noise based on th Monte Carlo simulation," Technical Report of IECE SANE92-58 (1992-11)

11 M. Shimada, "SAR's AD conversion noise and radiometric calibration accuracy - Monte Carlo simulation on the correlation of the saturated SAR data and its related error (Japanese)," Technical report of IEICE, SANE 93-57 (1993-11), pp. 15-22.

12 M. Shimada, "Absolute Calibration of JERS-1 SAR and Image Quality (Japanese)," Japan Remote Sensing Society, vol. 14, no. 2, (1994), pp. 143-154.

13 M. Shimada, "Determination of the JERS-1 SAR antenna elevation pattern using the Amazon rainforest images (Japanese)," Japan Remote Sensing Society, vol. 13, no. 4, (1994), pp. 327-338.

14 M. Shimada, Y. Nakatani, T. Kawada, "Removal of the interferences appeared within the SAR images, " submitted to COSPAR'98

15 M. Shimada, "A multi-platform verification processor for the SAR calibration and the interferometry," submitted to COSPAR'98.

SAR interferometry

1 M. Shimada, "JERS-1 SAR interferometry," submitted to IEEE Trans. Geosci Remote Sensing, Jun. 1997. (Comments were received in Feb. 1998).

2 M. Shimada, "SAR Interferometry," IEICE, Japan, Dec. 1995

3 M. Shimada, and Haruto Hirosawa, "Normalized radar cross section corrected for the topographic slope using SAR interferometry," submitted to IEEE Trans. Geosci Remote Sensing, June 1998.

The others

1 M. Shimada, M. Sasanuma, "Simulation of Wind-Vector Estimation - design evaluation of microwave scatterometer -," pp. 379-387, The Ocean Surface, 1985, Reidel Publishing Company

2 M.Shimada, T. Yamazaki, M. Tsuji and K. Ayabe, "DATA COLLECTION SYSTEM ON JAPAN'S FIRST MARINE OBSERVATION SATELLITE; INFLIGHT EVALUATION OF THE SYSTEM PERFORMANCES," Proceedings of IGARSS'88 Symposium, Edinburgh, Scotland, 13-16 Sept. 1988, pp. 283-286

3 M. Shimada, H. Oaku, M. Yamanashi, "Development of the NASDA Airborne Synthetic Aperture Radar (NASAR-1)," IGARSS '96, Nebraska.

衛星搭載用合成開口レーダを用いた地表の規格化後方散乱断面積の計測に関する研究